# DESIGNING NOVEL CERMET MATERIALS IN THE TITANIUM-BORON-IRON-MOLYBDENUM SYSTEM

by

Alexander Raymond Lark

A thesis submitted to the faculty of
The University of Utah
in partial fulfillment of the requirements for the degree of

Master of Science

Department of Metallurgical Engineering

The University of Utah

May 2018

**The University of Utah Graduate School**

# STATEMENT OF THESIS APPROVAL

The thesis of **Alexander Raymond Lark**

has been approved by the following supervisory committee members:

| | | |
|---|---|---|
| **K.S. Ravi Chandran** | , Chair | **2/22/18** Date Approved |
| **Darryl Butt** | , Member | **2/22/18** Date Approved |
| **Krista Carlson** | , Member | **2/22/18** Date Approved |

and by **Manoranjan Misra** , Chair/Dean of

the Department/College/School of **Metallurgical Engineering**

and by David B. Kieda, Dean of The Graduate School.

## ABSTRACT

This study focuses on synthesizing cermet materials consisting of a two-phase structure of ductile beta-Ti solid solution phase and a hard titanium boride TiB phase, which appears as a nanostructured TiB whisker network surrounded by a beta-Ti matrix. Iron and molybdenum are used in this Ti-B-Fe-Mo alloy system as stabilizers of the beta-Ti phase to control the proportions of alpha (hcp) or beta (bcc) solid solution phases, and also have some solubility in the TiB phase, forming ternary (Ti,X)B borides.

The calculation of phase diagrams (CALPHAD) approach using Thermo-Calc software was used to predict and design sample compositions and processing temperatures. Samples were synthesized by mixing Ti, Fe, Mo, and $TiB_2$ powders at varying concentrations to achieve desired compositions. Electric-field-activated-sintering was used to synthesize samples with a reaction sintering process. This study focused on analysis of samples in the cermet range, between 50 and 70 volume percent TiB phase. Density measurements indicated that fully dense cermet materials were created. Generic two-phase microstructure was confirmed using X-ray diffraction and scanning electron microscope (SEM) techniques.

Mechanical properties including flexural strength and fracture toughness were evaluated. Four-point flexural strength varied between 826 MPa and 941 MPa for 50, 60, and 70 volume percent TiB samples. Inclusion particles were responsible for initiation of fracture in flexural testing and led to variations in strength. Precracked beam fracture

toughness varied between 10 and 17.8 MPa√m for 50, 60, and 70 volume percent TiB samples, with fracture toughness improving with the addition of more ductile beta-Ti phase and after heat treatment.

The mechanical and physical properties of Ti-TiB cermets were compared against commercially available cermets such as WC-Co. The present samples have potential for some practical applications as cutting, shaping, or forming tools.

## TABLE OF CONTENTS

## LIST OF TABLES

## LIST OF FIGURES

# CHAPTER 1

# INTRODUCTION

## 1.1 History

A cermet is derived from a combination of the words “ceramic” and “metal.” According to a definition given in the ASM Metals Handbook [1], a cermet is “a powder metallurgy product consisting of ceramic particles bonded with a metal.” The aim behind development of these materials was to produce a material that has designed properties superior to those attained with ceramics or metals independently [2]. In the realm of composite materials containing both ceramic and metal components, cermets fall in the nominal range of 30 to 90 volume percent ceramic particle content.

The original drive for the development of cermet materials came in the early twentieth century. High-speed steels were being used in machining, but could only cut in the range of 20 to 40 m/min. There continued to be industrial need for higher cutting speeds than high-speed steel could offer. Cemented carbide, which consists of a hard WC phase bound by Co matrix phase, was developed in 1923 by Osram Lamp Works in response to this need. WC-Co offered cutting speeds from 100 to 150 m/min [3]. The development of WC-Co composite materials was the start of the field of cermet research.

For several decades, cermet development was dominated by the creation of TiC-based materials with combinations of Ni, Mo, Cr, Al, and other metals serving as metal

matrices. These TiC cermets were widely used as machine tools for high-speed finishing of steel. Further need for refinement of cermet properties, particularly for machine tooling needs, led to the development of Ti(C,N) cermets as well as coated WC-Co [4].

Several factors have led to the expansion of research into cermet materials with noncarbide ceramic phase. One factor driving this expansion was the desire to have cermets with low density which could be used as low-weight structural materials in aerospace and automotive applications. Another driving factor was ease of processing. For some time, WC-Co cermets required multiple processing stages, including high-temperature sintering of WC followed by infiltration of liquid Co as a matrix material. There has been a drive for less expensive processing methods than those of traditional WC-Co, such as one stage sintering processes and relatively low-temperature synthesis of cermets.

One result of this expanding cermet research was the development of titanium and boron-based cermets. Due to the low density of boron, these cermets also have very low density and can be used in lightweight applications. The majority of the work on boride cermets in industry has been centered around cermets in which titanium diboride ($TiB_2$) is the primary ceramic phase. However, the synthesis of cermets with TiB remains of special interest because of the thermodynamic driving force for the creation of TiB from $TiB_2$ during sintering. TiB ceramic material can achieve hardness as high as 1600 $kgf/mm^2$ [5]; having ceramic material of such high hardness coupled with ductile Ti material offers good potential for machine tooling applications. Recent developments in electric-field-activated sintering technology have made it possible to sinter Ti-TiB cermets in one step at a relatively low processing temperature [6].

## 1.2 Problem Statement

The author is part of a research group at the University of Utah that undertook the task of furthering research into the creation of Ti-TiB cermets. The most noticeable need in this field was the improvement of mechanical properties of Ti-TiB cermets. Previous work showed bending strength around 450 MPa for the range of 50 to 70 volume percent TiB, and toughness around 6 MPa√m for the same composition range [7]. These mechanical properties were evaluated for Ti-TiB cermets in which the titanium phase consisted of alpha (hcp) Ti. It is widely accepted that beta (bcc) Ti is more ductile than alpha Ti, and there was room for research into developing a beta Ti-based Ti-TiB cermet, which would improve bulk strength and toughness properties.

To create a cermet with a beta-Ti matrix phase, the beta-Ti phase must be stabilized to a lower temperature. This is done by alloying additions of beta-stabilizing elements such as Fe, Mo, Nb, and V, among others. But the scope of this research presents a unique challenge by trying to stabilize the beta-Ti phase within a composite system in which reaction sintering takes place to create the ceramic phase. The presence of metastable ternary boride (Ti,X)B phases is expected and will require further evaluation [8].

In recent years, the author's research group has successfully synthesized various Ti-TiB composites by reaction sintering Ti and $TiB_2$ particles. Ti-TiB composites of ceramic content varying up to 90 volume percent were synthesized. This work began investigation into the use of beta-stabilizing alloy additions in the creation of Ti-TiB composites in ternary and quaternary alloy systems [9]. This work highlighted a need for focus on specific ranges of composition, such as a cermet range of composition. Thus,

successful synthesis of cermets in the Ti-TiB system with alloying additions creates a novel material in need of evaluation. Very little work has been done on evaluation of quaternary Ti-TiB composite alloy systems in the cermet range.

The general focus of this work was to synthesize fully dense Ti-TiB cermet materials in the Ti-B-Fe-Mo alloy system by reaction sintering Ti, $TiB_2$, Fe, and Mo powders. The expected result was a cermet composite with a nanostructured network of TiB whiskers embedded in a beta-Ti matrix. Following successful synthesis, mechanical property evaluations were in order to determine potential industrial uses for these cermet materials.

### 1.3 Scope of the Present Research

The present research is focused on the synthesis of 50, 60, and 70 volume percent TiB cermet materials with a beta-Ti matrix phase, as well as understanding the mechanical behavior including hardness, bending strength, and fracture toughness. The principal objectives of the research are the following:

- To use thermodynamic data and the CALPHAD approach to design cermet materials in the Ti-B-Fe-Mo system. The CALPHAD approach is implemented using the Thermo-Calc software package. This approach was chosen because the intended cermet materials are novel. Thus, standard methods of alloy investigation would require time-consuming, expensive, and repetitive empirical sample preparation. The CALPHAD method allows predictive modeling of compositions and processing parameters, which fulfill the requirements of the traditional empirical side of investigation.

- Synthesize fully dense cermet materials in the Ti-B-Fe-Mo system by electric-field-activated sintering, varying beta-stabilizing element content as well as TiB final content by volume percent.
- Optimize the Fe:Mo ratio (by weight) and evaluate the behavior of alloying elements Fe and Mo during sintering. The amount of these beta-stabilizing elements that go into the TiB phase to create ternary (Ti,X)B borides may alter the effectiveness of the stabilization of the beta-Ti matrix phase.
- Evaluate the microstructure of the sintered materials, comparing among the different compositions. This will be done using X-ray diffraction and scanning electron microscopy methods. Microstructure of as-sintered samples is analyzed as well as post-fracture samples.
- Evaluate mechanical properties of the 50, 60, and 70 volume percent TiB samples by performing Vickers hardness, four-point bend testing to evaluate flexural strength, and four-point bend precracked beam fracture toughness testing to evaluate material toughness.
- Implement a heat-treatment on the 50, 60, and 70 volume percent TiB samples and repeat hardness, flexural strength, and fracture toughness testing to characterize changes in mechanical properties.

# CHAPTER 2

# LITERATURE REVIEW

## 2.1 Introduction to Cermets

There is debate in industry about the differentiation among hardmetals, cermets, and cemented carbides [2,3]. For the sake of simplicity, this thesis will categorize all materials with a ceramic phase between 30 and 90 volume percent bound by a metal matrix phase of the remaining volume percent as cermets.

The ceramic phase in this definition consists of a metallic element bonded with C, B, N, or O in varying stoichiometry. Engineering ceramics are classified generally into oxide ceramics and nonoxide ceramics. Boron carbide ($B_4C$), silicon carbide (SiC), silicon nitride ($Si_3N_4$), titanium carbide (TiC), titanium carbo-nitride (Ti(C,N)), and tungsten carbide (WC) are among the nonoxide ceramics. Aluminum oxide ($Al_2O_3$), zirconia ($ZrO_2$), and magnesium oxide (MgO) are among the oxide ceramics [10]. With the exception of very niche applications, the ceramic phase in cermets is generally limited to nonoxide ceramics. The metallic binder phase is historically limited to Ni, Cr, Co, Ti, Mo, Al, and Fe [3]. However, small quantity alloying additions to these binder elements or combinations thereof are often used, as will be demonstrated in this research.

As demonstrated above, the first cermets to find industrial use were carbide-based cermets. Although WC-Co cermets were able to achieve high cutting speeds, limited tool

life was a concern. WC-Co cutting tools demonstrated high crater wear, which deteriorated the life of the tool. To counter this, TiC was added to the WC-Co materials to make WC-TiC-Co cermets. This dramatically reduced crater wear [11]. TiN and Ti(C,N) were also investigated as alloying and coating materials for cemented carbide cutting tools to further improve tool life by providing a hardened shell, which would have to be worn through before crater wear began deteriorating the substrate cemented carbide [12]. In this pattern, the development of new cermets grew out of the need for property improvements of previous cermets.

### 2.1.1 WC Cermets

WC-based cermets are usually produced with powder metallurgy methods in which WC and metal powders are mixed and pressed into compacted green parts, followed by sintering to form consolidated bulk materials [13]. Another common method is to preform porous WC structures and infiltrate molten metal material into the structure [14]. Production of bulk WC-based cermets is usually performed using furnace melting, but alternatively, exothermic thermite reactions have been utilized to melt metal matrix materials and facilitate fast infiltration of the WC preform structure [15].

WC cermets generally contain a metallic binder phase of Co. Depending on the intended application, the grain size of WC in WC-Co ranges from about 0.3 μm to 40 μm. Coarse WC grains of 3 μm and larger are used in mining applications. WC-Co metal cutting tools contain WC grains between 1 and 2 μm. Cermets with submicron WC particles have many niche applications in machining, punches, and nozzles, to name a few [16]. WC has a simple hexagonal unit cell, but the asymmetrical positioning of C

atoms in relation to W atoms generates different types of planes at the interface with Co. The result is rough asymmetrical angular grains of WC embedded in the Co matrix [17].

In industrial applications, the Co content of these cermets ranges from 3 to 30 weight percent. Strength and toughness of WC-Co cermets depend on optimization of the ratio of ceramic to matrix material as well as optimization of the WC grain size. Materials with larger WC grains on the order of 20 to 30 μm exhibit ductility, whereas materials with small WC grains of 3-6 μm behave in a brittle fashion [18]. Increased WC content will lead to increased hardness but decreased toughness.

WC-Co materials with varying ratios of WC and Co have an average density of around 15 $g/cm^3$. Jia et al. estimate that a WC-Co sample with about 75 volume percent WC phase demonstrates a hardness around 1950 $kgf/mm^2$ and a fracture toughness around 8 MPa√m [19]. Naturally, many variations on fracture toughness are possible by changing WC grain size, binder material, or phase of the binder material. Fracture toughness of WC-Co cermets with high WC ceramic content has been measured up to 20 MPa√m [20]. The bending strength of WC-Co composites in the cermet WC volume percent range have been calculated in the range of 2200 to 4000 MPa [21].

### 2.1.2 Ti(C,N) Cermets

TiC-based cermets were produced in part because of the shortcomings of WC-Co cermets during use. At high machining speeds, and therefore high friction-caused machining temperature, WC-Co cermets demonstrated debonding phenomenon and low oxidation resistance that quickly deteriorated tool life. TiC cermets were able to function at higher cutting speeds and showed higher oxidation resistance than WC-Co, but had

shortcomings of their own, namely that TiC showed poor wettability that hindered bonding with the matrix phase. The matrix phase at that time was typically a combination of Ni, Mo, and Cr.

The need for easier processing led to the sintering additive of $Mo_2C$ [4]. $Mo_2C$ powders were mixed with the binder metal powders of Ni and Mo and upon sintering, formed a rim of (Ti,Mo)C around the TiC particles, which increased the wettability of the TiC particles. Taken one step further, additives like $Mo_2C$ mixed with pure parent materials like unalloyed Ti birthed the method of reaction sintering of cermets. The reaction sintering of Ti and metal carbides such as $Mo_2C$ provides the carbides for formation of TiC ceramic particles, as well as introducing particles like Mo into the Ti matrix to assist in stabilization of desired phases [22]. It was later found that TiC cutting performance and wear resistance could be further improved by the addition of N to create Ti(C,N) cermets. Once again, the key ingredient in the processing of these cermets was the addition of $Mo_2C$ to enhance wettability and assist in creation of desired phases [23].

Attempts have been made to combine the advantages of WC, TiC, and TiN by creating composite materials with all three carbides bound in a matrix phase. Li et al. created cermet composites with 20 weight percent Co binder phase and varying amounts of WC, TiC, and TiN. Their study found that strength varies between 800 and 1000 MPa and fracture toughness varies between 16 and 20 MPa$\sqrt{m}$ [24]. Cermets of this combination of ceramic phases have been measured at hardness values between 1500 and 1900 kgf/mm$^2$.

TiC has a similar crystal structure to that of tungsten, as explained in Section 2.1.1. When combined with WC and other carbides and allowed to sinter at high

temperature or for long periods of time, TiC forms carbide solid solutions with the other carbides in the mixture. These carbide solid solutions remain as distinct ceramic particles surrounded by a matrix such as a Ni-Co solid solution to form a cermet material [25].

One drawback of TiC and Ti(C,N)-based cermets is low fracture toughness. A cermet of this type with metallic binder phase of about 20 weight percent exhibits a fracture toughness around 5 to 6 MPa√m. Properties like flexural strength and hardness can be improved within the range of 1000 to 1400 MPa and 1900-2000 kgf/mm$^2$, respectively, by different alloying additions [26]. Fracture toughness of Ti(C,N)-based cermets is more difficult to improve. By using higher binder metal content or increasing grain size of the ceramic phase, fracture toughness can be improved up to 12 MPa√m, but hardness is reduced, which in turn reduces the effectiveness of the alloy for cutting [27]. There have been TiC-based cermet materials developed for noncutting applications like impact-resistant armor, which have demonstrated toughness as high as 20 MPa√m by increase in metal binder phase, but this seems to be the upper limit of toughness in TiC-based cermets [28].

### 2.1.3 $B_4C$ Cermets

$B_4C$, as an engineering ceramic, is best known for its high hardness and wear resistance. It has a hardness value in excess of 3000 kgf/mm$^2$. It also has a low density of around 2.5 g/cm$^3$. Both of these qualities have made it an ideal material for use as a lightweight armor material for both vehicle and personnel [29]. Its high hardness also makes $B_4C$ a useful ceramic material for use in cermets. $B_4C$ itself has a low fracture toughness of 3 to 4 MPa√m, but this can be improved the addition of a metal binder

phase as in cermets [30].

The most common binder metal in $B_4C$ cermets is Al. It has been found that the addition of Al and $Al_2O_3$ overcomes sintering barriers and greatly increases the densification of $B_4C$ as well as acting as a binder [31]. Al is often melt infiltrated into the $B_4C$ structure, which can increase the hardness of the $B_4C$ slightly due to the prevention of pore collapsing [32]. $B_4C$-Al cermets are designed for use outside of cutting tools, unlike previously discussed cermets. As such, their mechanical properties are difficult to compare.

Another common binding method of porous $B_4C$ structures is the infiltration of molten Si, sometimes with a small addition of a carbon source. The Si reacts with the $B_4C$ to form a composite structure in which the $B_4C$ is strongly bonded to the Si matrix phase due to reaction [33].

The use of Ti as a matrix material with $B_4C$ ceramics has received interest recently. This is a purposefully designed reaction sintering process in which $B_4C$ reacts with Ti to make final products of TiC and TiB according to the reaction $5Ti + B_4C \rightarrow 4\ TiB + TiC$. Thus, a cermet is created that contains ceramic materials of TiC and TiB surrounded by a Ti matrix [34]. This method, however, has drawbacks because the starting $B_4C$ powder is expensive and difficult to make. Thus, efforts to create boride-based ceramics have followed other processing routes.

### 2.1.4 $TiB_2$ Cermets

There is research interest in boride-based cermets because of their high temperature durability and high hardness. These cermets have high wear-resistant

properties. Good electrical conductivity of borides has also played a key role in the drive for development of these cermets.

$TiB_2$ has a hardness of up to 2500 kgf/mm$^2$ and has been used effectively as an armor plating material. $TiB_2$ cermets have been used as coating materials on stainless steels and Ni-based superalloys to protect base materials in abrasive applications [35].

Initial work in the fabrication of solid structure boride cermets had limitations because of the poor sinterability and high brittleness of borides. A liquid phase sintering process was developed to counter these issues. Initially, the base materials used were Fe, Co, and Ni. These base materials reacted with borides to form ternary boride cermets such as $Mo_2FeB_2$-Fe, $Mo_2NiB_2$-Ni, and WCoB-Co [36,37].

To avoid forming these borides, it was then natural for researchers to attempt to use the base metals of Fe, Co, and Ni to make cermets with $TiB_2$ as the ceramic phase. However, during sintering of $TiB_2$ with these transition metals, undesired metallic borides of MB, $M_2B$, and $M_{23}B_6$ were created, which reduced the strength and toughness of the bulk materials. It was found that additions of alloying elements Al and Ti to an Fe-Ni matrix prevents the formation of these unwanted boride compounds. Depending on control of the phases in the metallic matrix, hardness and toughness of these cermets can reach about 1900 kgf/mm$^2$ and 15 MPa$\sqrt{m}$, respectively [38].

$TiB_2$ cermets with other metallic binder phases have since been attempted. For example, a $TiB_2$-W cermet has been developed that demonstrated a high hardness of 2500 kgf/mm$^2$, as well as bending strength of about 700 MPa and fracture toughness of 8 MPa$\sqrt{m}$. However, this alloy system also saw the development of undesirable ternary borides that altered mechanical properties [39].

A simpler alloying approach has been to mix $TiB_2$ powders with Ti binder powders and sinter. During sintering of these powders, some TiB forms according to the equation $Ti + TiB_2 \rightarrow 2TiB$ [40]. By controlling the ratio of starting powders, the final ratio of $TiB_2$ and TiB can be controlled. B has a limited diffusion rate into Ti, so controlling the processing time and temperature can also be used as a tool for controlling final structure. Through these methods, it is possible to make cermets with the high hardness of $TiB_2$ and the toughening properties of TiB [41]. It will be shown hereafter that the author's research group utilized this method.

## 2.2 Ti-TiB Cermets

Ti-TiB cermets strike a desirable balance among the mechanical properties of other cermets discussed above, with relatively high hardness, strength, and toughness. They have become incorporated into design of reaction-sintered cermet products because of the favorable thermodynamic properties of borides reacting with the correct alloying metals, as well as good electrical conductivity. Reinforcement of cermets with TiB maintains the high hardness typical of boride materials and offers higher toughness and strength than other boride reinforcements, such as $TiB_2$.

### 2.2.1 Physical Metallurgy of the Ti-B System

As mentioned in Section 2.1.4, industry cermets have often used $TiB_2$ as the ceramic phase. This is understandable given that $TiB_2$ has a higher melting point, elastic modulus, and hardness than TiB. However, formation of TiB and $Ti_3B_4$ at the Ti-$TiB_2$ interface during sintering of $TiB_2$-based cermets has been problematic for development of

these cermets. TiB cermets, as an alternative, do not have the problem of unwanted borides because there is no intermediate phase between Ti and TiB. Additionally, synthesizing TiB cermets requires lower B content and lower sintering temperatures, making processing easier [42]. TiB forms as long, single-crystal whiskers. According to theories of strengthening based on whisker reinforcement, large increases in modulus and strength can be achieved with relatively low whisker reinforcement. Mechanical properties are helped as well by a crystallographic constituency between TiB and Ti, which has a nearly perfect interface [43]. The ease of processing of Ti-TiB cermets is helped at least in part by TiB and Ti having similar densities of 4.56 g/cm$^3$ and 4.5 g/cm$^3$, respectively, as well as similar coefficients of thermal expansion at 7.15x10$^{-6}$/˚C and 8.2x10$^{-6}$/˚C, respectively [9,42].

In the Ti-B system, three boron compounds exist: TiB, $Ti_3B_4$, and $TiB_2$ at boron concentrations of about 18%, 22% and 30% by weight, as shown in Figure 2.1 [44]. Each of these borides have different crystal structures. The main distinction is between $TiB_2$ and TiB (Figure 2.2). Each of these crystal structures have the same basic building block: a trigonal prism with a B atom at the center of the unit cell surrounded by six Ti atoms at the corner positions [45,46]. However, the packing arrangement of these trigonal prisms is different for $TiB_2$ and TiB. In $TiB_2$, the prisms stack vertically with triangular faces on top of each other in a close-packed array, creating a hexagonal structure. TiB, conversely, stacks vertically with rectangular faces in contact with neighboring prisms, forming an orthorhombic structure. B atoms preferentially diffuse along B-B chains in the $[010]_{TiB}$ direction. This stacking behavior is how TiB grows into long, needle-like structures. The high electron density of B-B bonds in these orthorhombic needles is what gives TiB high

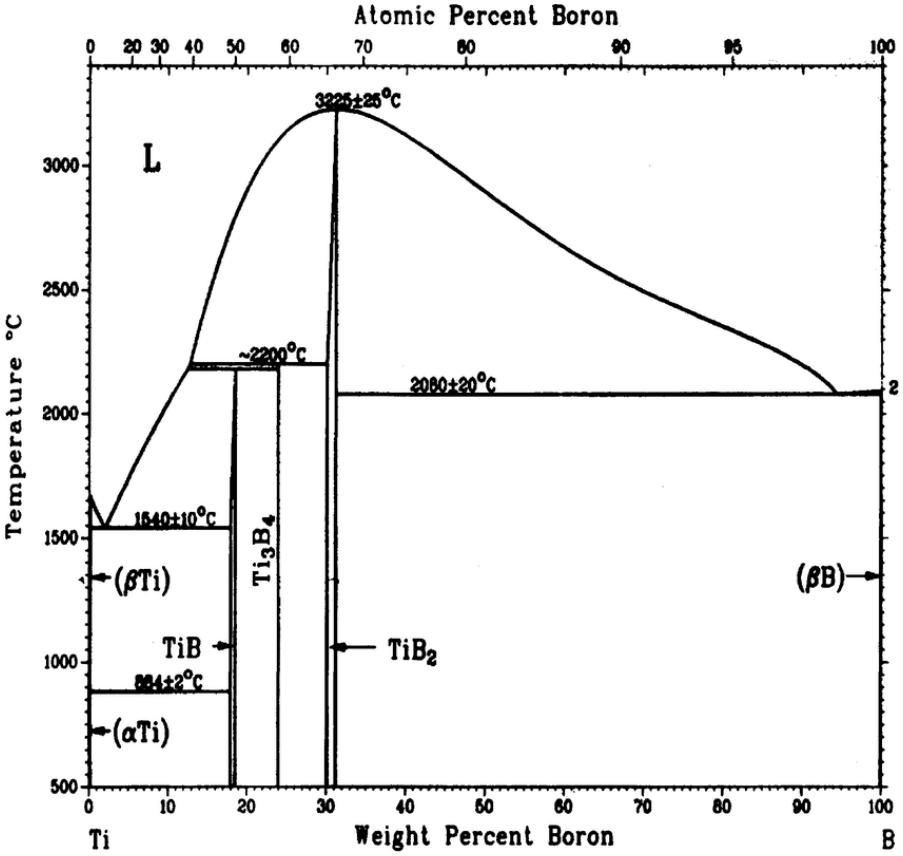


Fig. 2.1 Ti-B binary phase diagram. Adapted from [44].

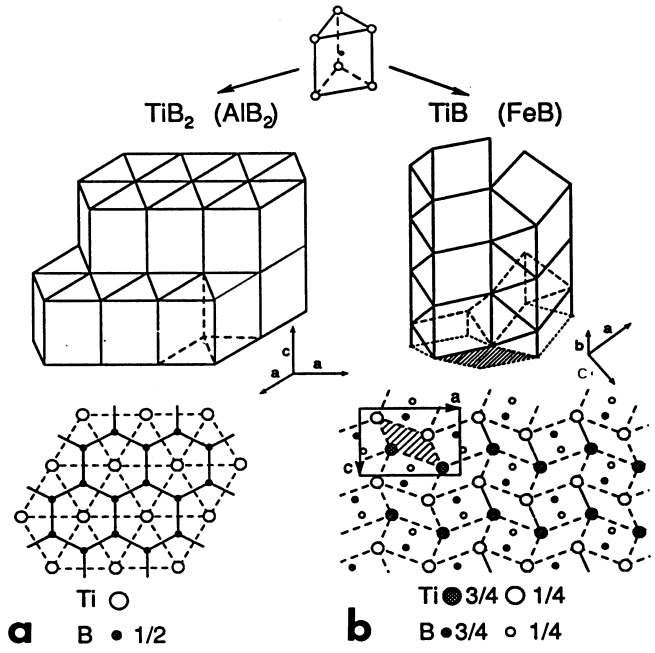


Fig. 2.2 Crystal structures of $TiB_2$ and TiB. Adapted from [46].

stiffness properties, which in turn increases strength and toughness [47]. Figure 2.1 shows $Ti_3B_4$ as an intermediate phase between TiB and $TiB_2$, but prior work by the author's research group has not found evidence of this phase appearing in composite materials made from the sintering of $TiB_2$ and Ti starting powders [48].

### 2.2.2 Reaction Sintering and Thermodynamic Design

In previous work, Ti-TiB cermets have been produced using a variety of methods including pseudo hot isostatic pressing, combustion synthesis, rapid solidification, and laser cladding. Some of these methods develop TiB reinforcement through in situ methods, while some start with ceramic TiB particles [49]. It was found that methods of melt solidification to form Ti-TiB cermets produced a coarse product, which contained internal holes due to shrinkage [50].

The author's research group has shown that reaction sintering using electric-field-activated sintering, also known as spark plasma sintering, is an effective method for synthesis of in situ Ti-TiB composites [5,45,48]. According to Figure 2.1, when the B content is less than about 18 weight percent, alpha-Ti and beta-Ti phases can coexist in a stable manner with TiB up to 1540˚C.

It is possible to form Ti-TiB composites by mixing Ti and B powders and reacting according to the reaction $(1+x)Ti + B \rightarrow TiB + xTi$. However, this reaction is highly exothermic and can create control problems during processing [7,10]. Alternatively, by utilizing the reaction $(1+x)Ti + TiB_2 \rightarrow 2TiB + xTi$, TiB reinforcements of chosen volume fraction can be formed in situ with the Ti matrix. This reaction is made possible by a negative free energy of formation value of TiB forming from Ti and $TiB_2$ powders

(Figure 2.3) [42]. Despite having a small negative free energy of formation value, the reaction free energy is nonetheless negative, which means the formation of TiB from Ti and $TiB_2$ powders is favorable if the ratios of starting powders are carefully controlled.

The morphology of TiB in bulk Ti-TiB composites can be altered by optimizing powder-packing parameters. Generally, $TiB_2$ powders are smaller than Ti powders. This is because Ti and B form strong covalent bonds, which make $TiB_2$ resistant to oxidation. Consequently, $TiB_2$ powders can be milled to sizes around 5 μm. Pure Ti powders are generally in a size range around 30 μm. The larger size of Ti powders in comparison is due to the high oxygenation susceptibility of Ti powders. Ti powders must have low oxygen content to react properly in the Ti-TiB system. Keeping oxygen content low enough in Ti powders milled smaller than 30 μm becomes exponentially expensive due to required atmospheric controls and chemical removal of oxygen. Because most materials

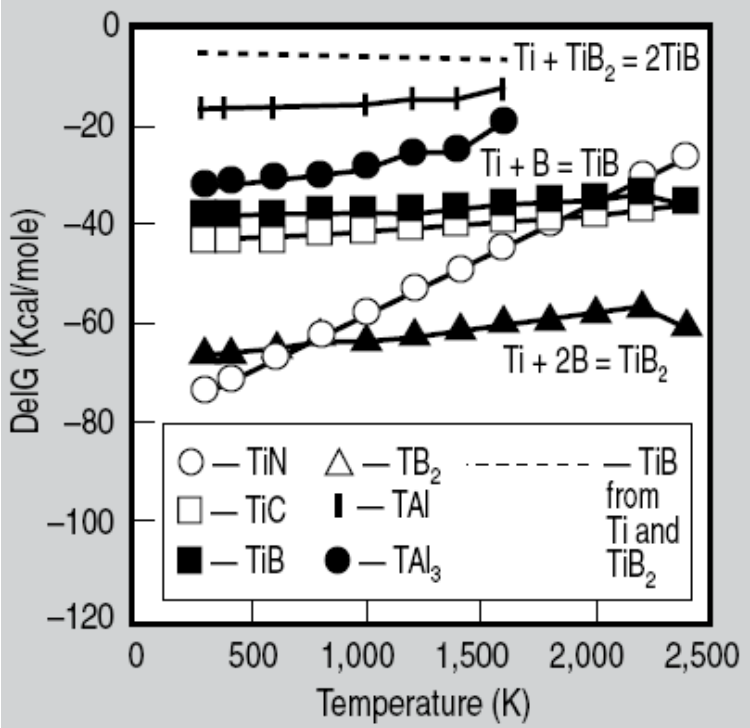


Fig. 2.3 Free energy of formation of cermet reinforcement materials. Adapted from [42].

research is targeted toward producing bulk materials in as inexpensive a fashion as possible, powder-packing parameters and sintering reactions have been designed for powders of these sizes.

The first parameter that can be manipulated to affect final morphology is the amount of $TiB_2$ in the starting powders. Naturally, the amount of $TiB_2$ starting material will be dictated by the desired final composition. But in a bimodal system of Ti and $TiB_2$ powders, 29 volume percent $TiB_2$ powders is a critical point for developing differences in final morphologies [48]. Figure 2.4 illustrates the differences in morphologies above and below the critical point of 29 volume percent $TiB_2$. It should be noted that the morphology generated from higher $TiB_2$ content includes clusters of nanowhiskers that form on a nanoscale as they impede each other's growth. It has been found that these nanoscale whiskers are an important aspect of impeding crack growth and strengthening the matrix phase, which greatly improves strength and toughness properties of the bulk material [51].

A second method of changing final morphology is by increasing the packing density of the starting powders by adding powder size differences, such as changing from a bimodal to a trimodal powder mix. Often this role is fulfilled by the addition of phase-stabilizing elements, such as beta-stabilizers in Ti systems. As is discussed more in Section 2.2.3, some common stabilizing alloys of the beta-Ti phase are Fe and Mo. These elements have been shown to increase the packing density of base powders up to about 85% [52,53]. The resulting bulk material morphology is shown in Figure 2.5 [53]. This strategy results in nearly 100% dense cermet materials while also strategically stabilizing the beta-Ti phase.

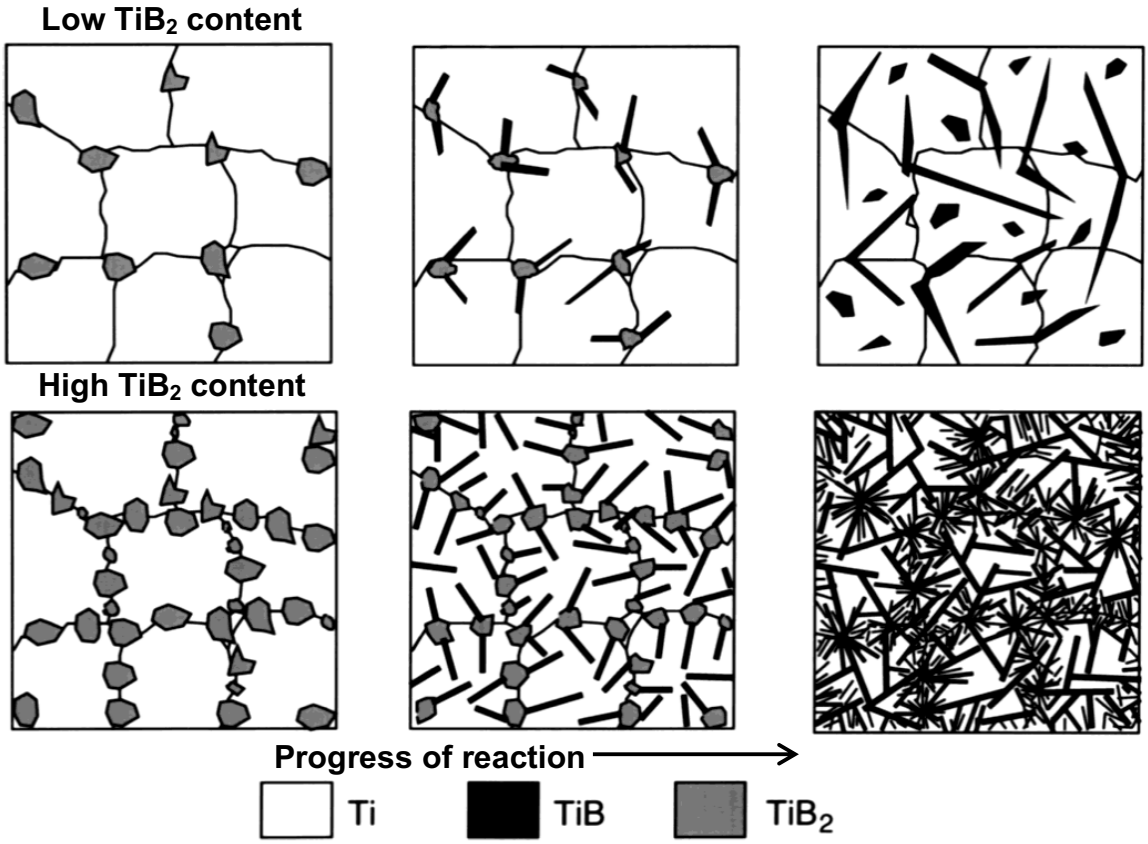


Fig. 2.4 Illustration of final Ti-TiB composite morphology due to high and low $TiB_2$ starting powder content. Adapted from [51].

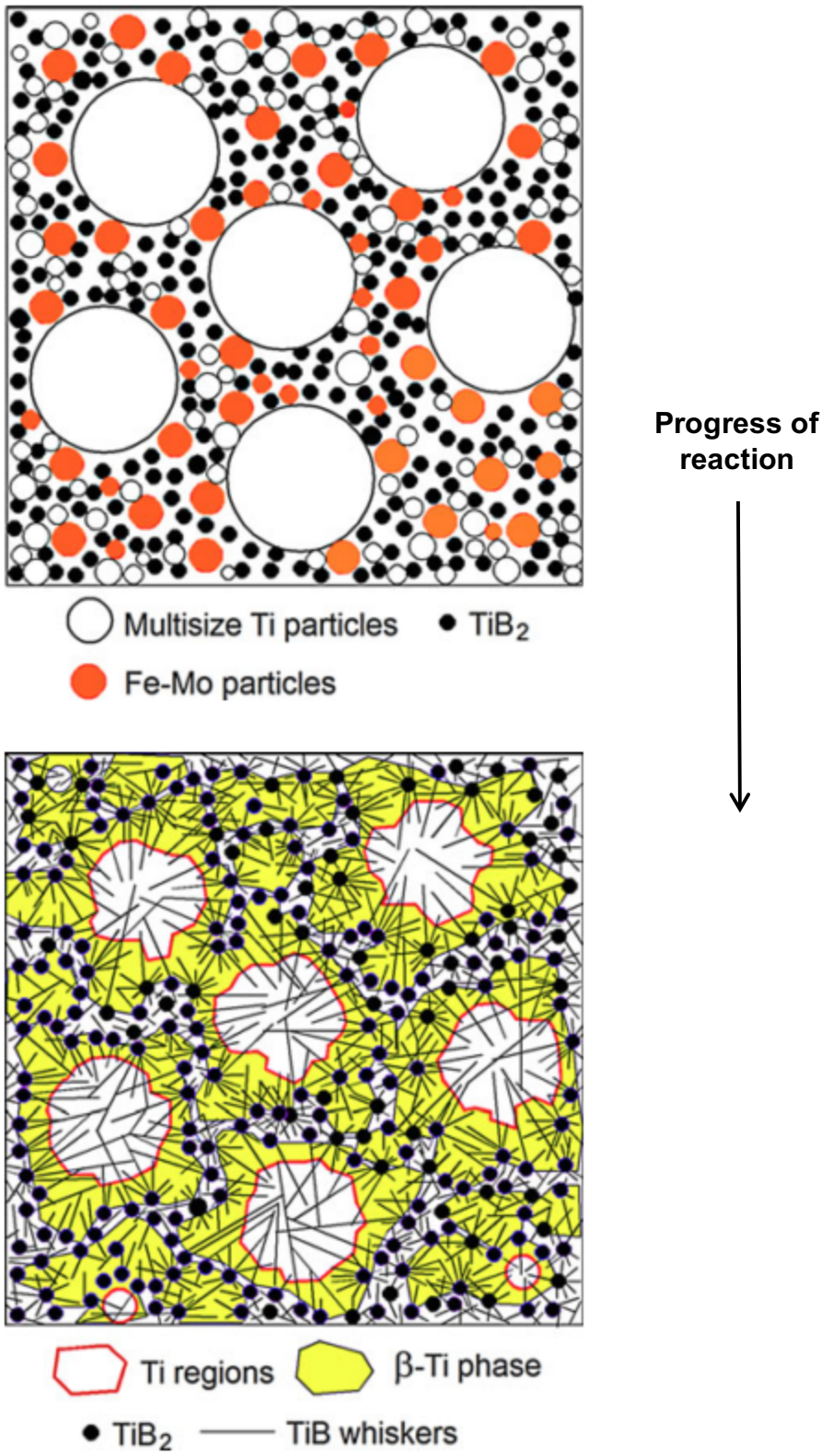


Fig. 2.5 Illustration of Ti-TiB morphology achieved using trimodal powder mix. Adapted from [53].

### 2.2.3 Stabilizing the Beta-Ti Phase

As discussed above, one primary objective of the research on Ti-TiB cermets is to improve mechanical properties of the bulk material by improving the properties of the Ti metal matrix phase. A common method for altering the properties of the Ti phase is to stabilize the alpha or beta phases of Ti using common alloying additions. Mo, V, Nb, Ta, Fe, Cr, Ni, Cu, W, Mn, and Co are common beta-Ti stabilizing alloying elements. These additions would push Ti alloys to the right of the graph in Figure 2.6. Some common alpha-stabilizing alloy additions are O, N, B, C, and Al. These elements push Ti alloys to the left of the graph in Figure 2.6 [54]. According to desired applications, the optimal Ti alloy may contain both alpha and beta phases, as in the commonly used industrial Ti alloy of Ti-6Al-4V. In Ti-6Al-4V, both alpha and beta stabilizers are used to strike an ideal balance, mechanically speaking, between alpha and beta phases [55]. It should be

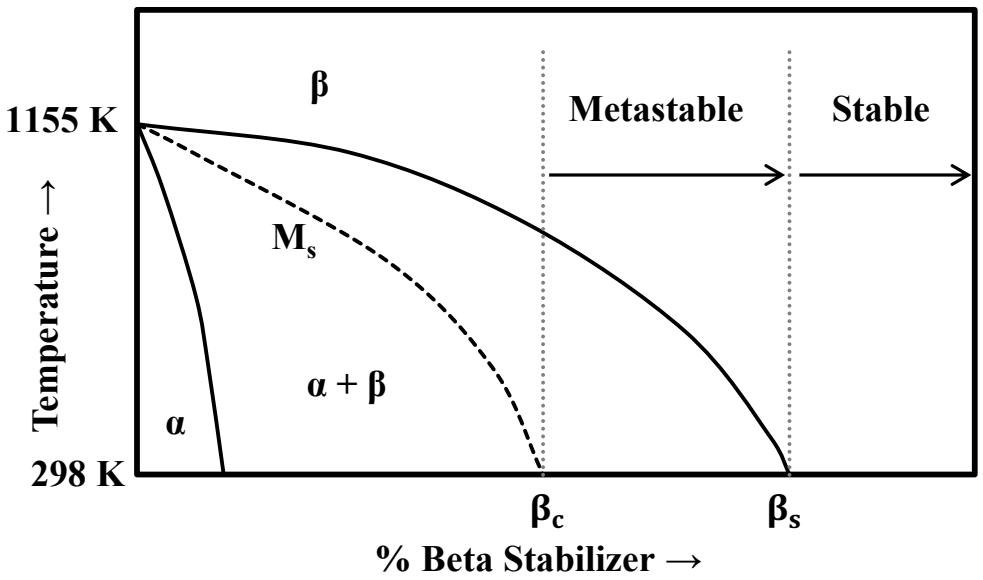


Fig. 2.6 The effect of beta-stabilizing elements on titanium alloys. α and β represent alpha and beta phases of Ti, respectively. $M_s$ represents the martensite start temperature. $\beta_c$ is the critical minimum amount of beta-stabilizing elements required for metastable beta-Ti alloys to remain fully beta upon quenching. $\beta_s$ is the minimum amount of beta stabilizer required for stable beta-Ti alloys. Adapted from [54–56].

reemphasized with the use of Figure 2.6 that there is a vital need for keeping the O content of the source Ti powder low. O is a very strong alpha stabilizer and will detrimentally affect the stabilization of the beta phase.

A previous study by Panda et al. [9] determined there was a significant increase in ductility of Ti-TiB composites due to stabilization of the beta phase because beta-Ti (bcc) is more ductile than alpha-Ti (hcp). Their work showed that in a Ti-TiB composite with 34 volume percent TiB, elastic modulus, ultimate tensile strength, and percent elongation were all increased by the addition of Fe, Mo, and Nb beta stabilizers. The Nb alloy showed a higher increase in ductility than the Fe and Mo alloys, but a lower ultimate tensile strength.

Many Ti alloys have been used as a binder phase in TiB-reinforced composites. Alloys with varying combinations of Al, V, Nb, Fe, and Mo have been tested with varying results. Comparing the effect of phase stabilization on mechanical properties based on surveying literature is complicated because amounts of alpha and beta phases will vary among studies due to different amounts of interstitials (C, O, N), variation in size of reinforcing TiB whiskers due to processing, and varying amounts of alpha and beta stabilizing elements [42]. However, the principle remains that ductility of Ti binder phase increases, and therefore bulk material strength and toughness increase, by stabilizing the binder phase as beta-Ti by the proper alloying additions.

### 2.2.4 Heat Treatment of Ti-TiB Composites

Electric-field-activated sintering, also known as spark plasma sintering, has been established as an efficient process for synthesis of Ti-TiB cermets [49,57]. It is a powder

metallurgy process whereby starting powders are placed inside a graphite die and pressure is applied by hydraulic rams. A direct current pulse voltage is then passed directly through the powders through which the powders are resistance-heated and sintered. Du et al. [5] synthesized Ti-TiB composite materials with Fe and Mo additives by this method. The power output resulting from electric-field-activated sintering during this work is shown in Figure 2.7. The heating and cooling steps of this process can be observed in this graph because the temperature of the sample during sintering is directly correlated with the power output. The initial positively-sloped curve shows the heating of

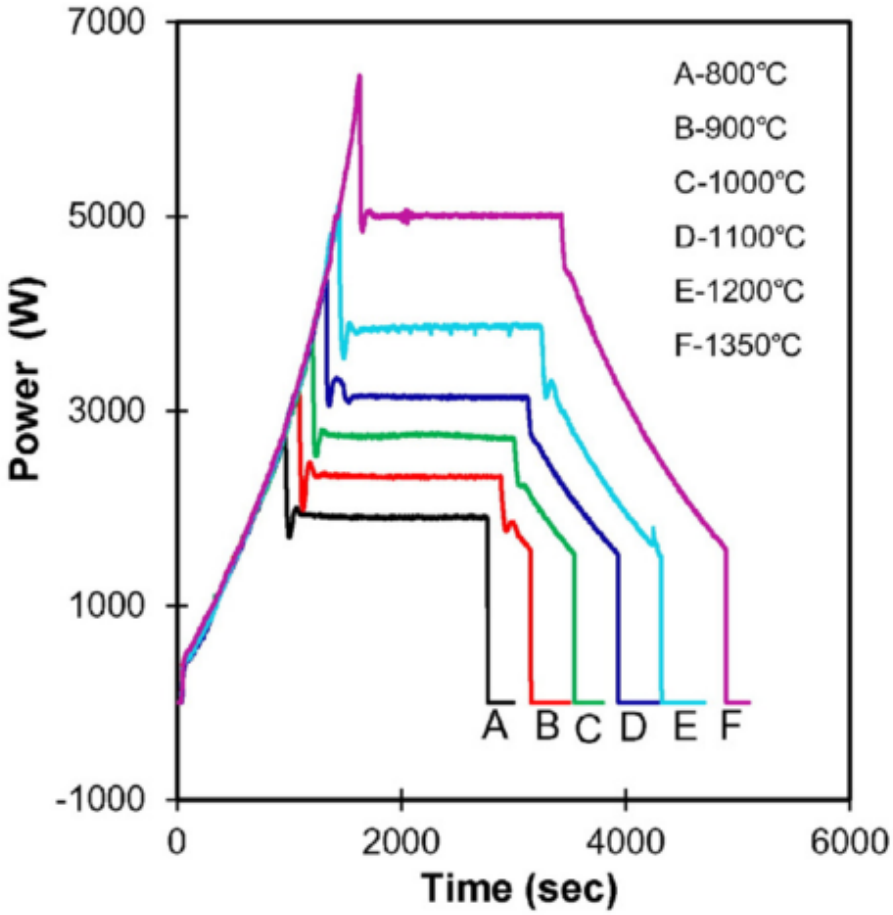


Fig. 2.7 Power vs. time output from electric-field-activated sintering of Ti-TiB composites. Adapted from [5].

the sample, and the flat line represents a prescribed hold time at a desired temperature. Of most interest is the negatively-sloped line that signals the start of the cooling period of the sample. In this example, power is still being applied during cooling, although at a diminishing rate. The purpose of this is to have a controlled cooling rate of 22˚C/min to avoid thermal shock to the graphite die and sample due to rapid cooling.

This method of slowed cooling poses no problems in a sample that has been alloyed with enough beta stabilizers to maintain the beta phase during the entire cooling process, as indicated on the right side of Figure 2.6. But in samples with beta stabilizing content in the metastable range between $\beta_c$ and $\beta_s$ in Figure 2.6, slow cooling would allow formation phases other than beta.

In the author's work, the synthesized Ti-TiB samples with alloying additions were calculated to fall within the metastable beta alloy range, according to Equation 2.1, which calculates the beta stabilizer content in terms of equivalent Mo content [58]. The author

$$[Mo]_{eq} = [Mo] + \frac{[Ta]}{3} + \frac{[Nb]}{3.6} + \frac{[W]}{2.5} + \frac{[V]}{1.5} + 1.25[Cr] + 1.25[Ni] + 1.7[Mn] + 1.7[Co] + 2.5[Fe] \quad (2.1)$$

used the same equipment and the same heating and cooling regime as in Figure 2.7. Because the samples were metastable beta-Ti samples, the slow cooling was problematic for achieving full beta stabilization and avoiding the formation of alpha-Ti. Additionally, because Mo was used as a beta-stabilizer, the Mo-Ti binary system indicates the potential for formation of a metastable omega phase during slow cooling, which could further alter the mechanical properties of the bulk material [59–62].

In order to avoid unwanted phases and obtain a fully-beta microstructure at room temperature for Ti-TiB cermets with metastable range beta-stabilizing content, a simple

heat treatment is proposed: heat the samples into the beta range (above 1155 K, as shown in Figure 2.6) under inert atmosphere and immediately quench them. A quench with water at room temperature has been shown to be sufficient for achieving quenching rapid enough to avoid the formation of both alpha and isothermal omega phases [55,59–62].

# CHAPTER 3

# CALPHAD DESIGN IN THE Ti-B-Fe-Mo SYSTEM

## 3.1 Thermo-Calc Calculations

One facet of this cermet design is to incorporate CALPHAD-based calculations into alloy design in order to avoid time-consuming empirical trial and error synthesis experiments, where possible. This was done using Thermo-Calc software and a Ti-B-Fe-Mo thermodynamic database, which was constructed and maintained by Dr. Vikas Jindal during his post-doctorate work at the University of Utah. Previous to the author's work, the research group had synthesized and analyzed samples of varying compositions in the ternary systems of Ti-B-Fe and Ti-B-Mo and binary Ti-B system. The samples were analyzed to determine presence of phases and volume fraction of phases in order to verify or alter existing thermodynamic information for these systems. This, combined with other data from first principles calculations and literature surveys, allowed Dr. Jindal to modify the parametric free energy equations contained in his Ti-B-Fe-Mo database to more accurately reflect ternary behavior and assist in the construction of a free energy equation for the quaternary system.

Following established CALPHAD practice [63,64], the aforementioned Ti-B-Fe-Mo database contains free energy information for each unary system Ti, B, Fe, and Mo, each binary system Ti-B, Ti-Fe, Ti-Mo, Fe-B, Mo-B, and Fe-Mo, each ternary system Ti-

B-Fe, Ti-B-Mo, and Ti-Fe-Mo, and B-Fe-Mo, and the quaternary system of Ti-B-Fe-Mo. This free energy information is combined and utilized by Thermo-Calc software in order to generate the phase diagrams contained in this section. These diagrams were used as a basis for choosing processing parameters and compositions used throughout the course of this research project.

### 3.1.1 Binary Systems

The binary system of greatest use in this research is the Ti-B binary system. Even after the addition of beta stabilizers, the general behavior of the alloys included in this research are dictated by the line compounds and pseudo-line compounds contained in the Ti-B binary. Figure 3.1 shows little deviation from the Ti-B binary shown in Figure 2.1. The binary shows that by adding up to 50 mole percent B to Ti will result in a Ti-TiB composite. Since Ti and B are in a 1:1 stoichiometric ratio in TiB, it is conceivable that a sample of nearly 100% TiB could be synthesized, which was the aim of previous work in this group [5,10]. Of principle concern on this diagram are the beta-Ti + TiB and alpha-Ti + TiB phase fields. The goal of adding beta stabilizers to this system is to lower the phase stability line between these two fields from its current position at around 1157 K to a temperature close to room temperature.

The additions of Fe and Mo both have unique effects on the movement of this phase stability line. This is demonstrated in the binary Ti-Mo and Ti-Fe diagrams. The Ti-Mo binary diagram is shown in Figure 3.2. It can be seen that the addition of Mo to Ti has a strong broadening effect on the beta phase field, meaning the addition of Mo stabilizes the beta phase in both the direction of room temperature and the direction of

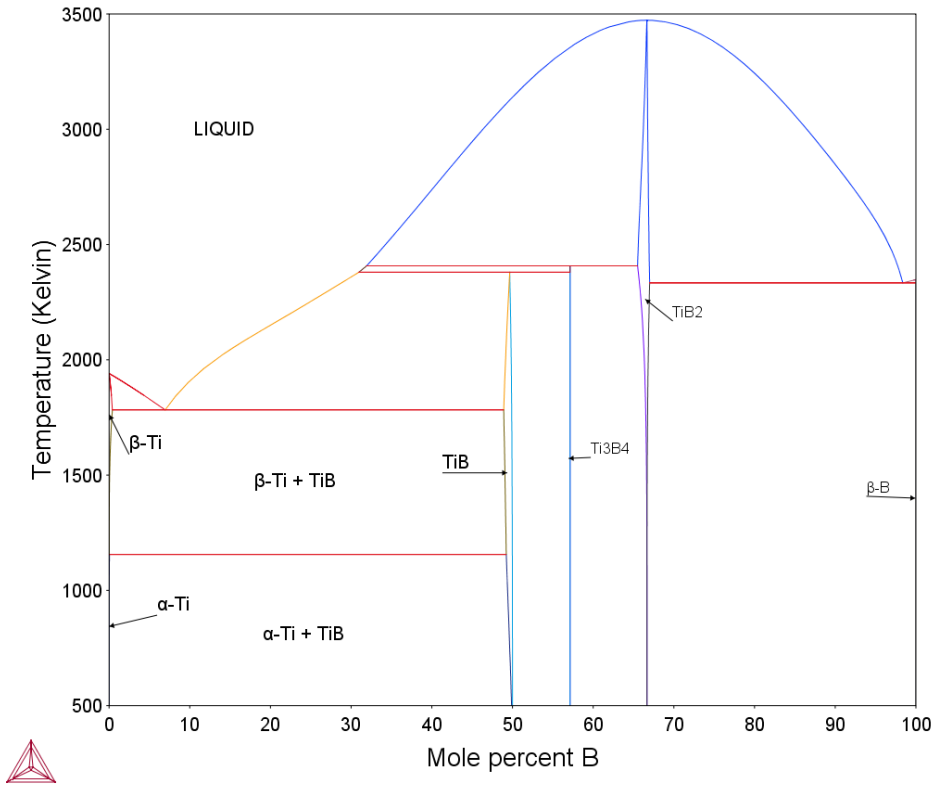


Fig. 3.1 Binary Ti-B phase diagram.

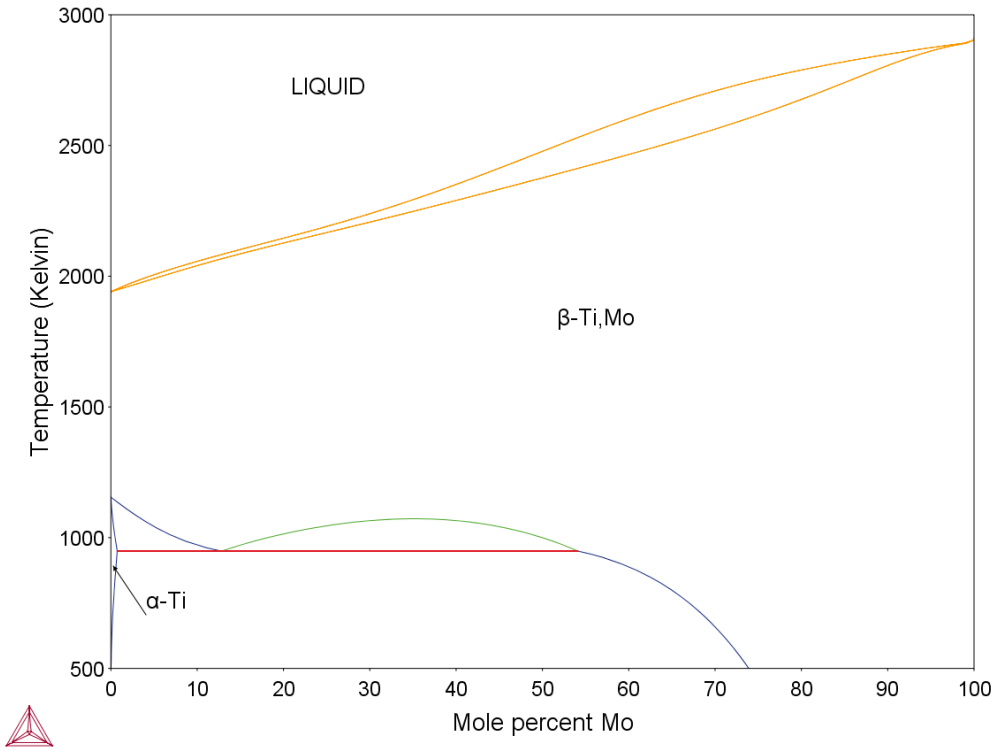


Fig. 3.2 Binary Ti-Mo phase diagram.

high temperature. Mo has better high-temperature stability than Ti, and this property is adopted by Ti in the binary system.

The Ti-Fe binary diagram is shown in Figure 3.3. From this it can be observed that an important impact of the addition of Fe to the Ti phases is that Fe has a drastic ability to reduce the temperature stability of the beta phase to a lower temperature. Additionally, it lowers the liquidus line in contact with the beta phase to a lower temperature, in contrast to the effect of Mo. The addition of Fe, therefore, is important for ease of processing of Ti-TiB cermets. By these implications, Fe acts as a sintering aid that lowers the required sintering temperature and aids the desired reaction during reaction sintering by acting as a wetting agent among the metal powders.

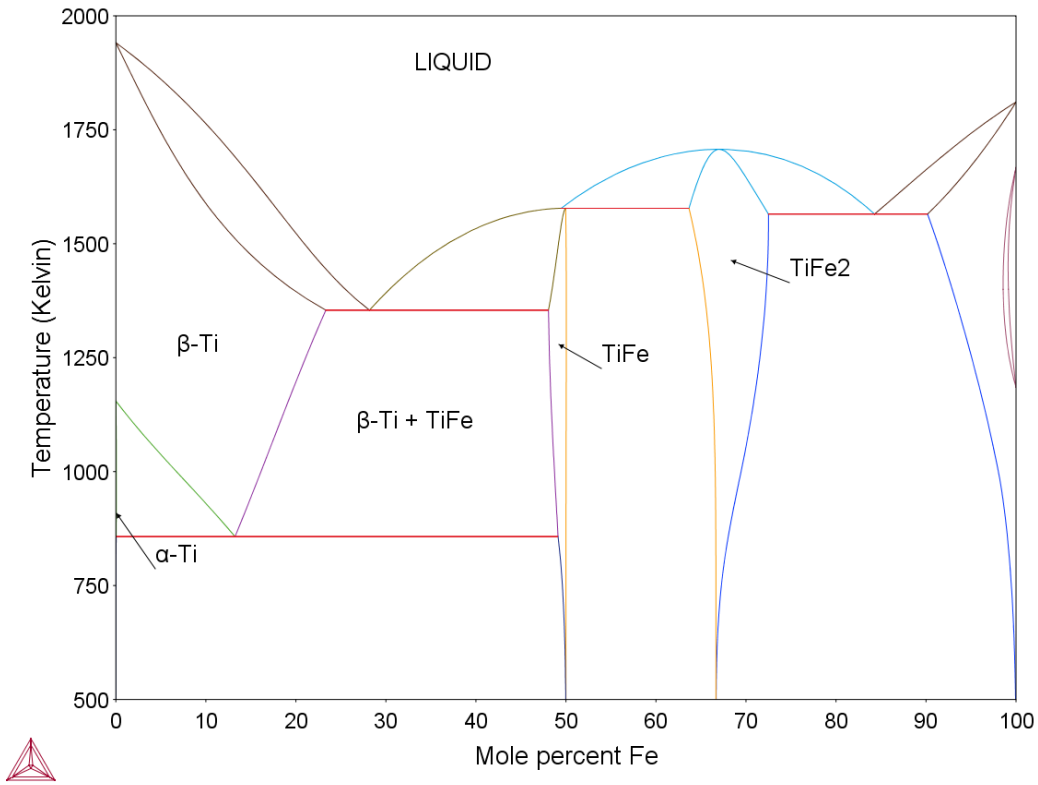


Fig. 3.3 Binary Ti-Fe phase diagram.

### 3.1.2 Ternary Systems

The behavior of the beta phase based on the additions of Fe and Mo makes it possible to sinter at a relatively low temperature range of 900˚C to 1300˚C [5,42]. The trends demonstrated in the binary systems of Section 3.1.1 are reflected in the ternary systems. Figure 3.4 shows the Ti-B-Fe ternary phase diagram at 1200˚C. At this processing temperature, the beta-Ti + TiB phase is a narrow processing window before liquid phase is created (liquid phase is problematic in electric-field-activated sintering of cermets). However, the Ti-B-Mo ternary phase diagram at 1200˚C in Figure 3.5 shows how Mo stabilizes the solid beta phase at this temperature. The combination of these two effects makes for ease of processing.

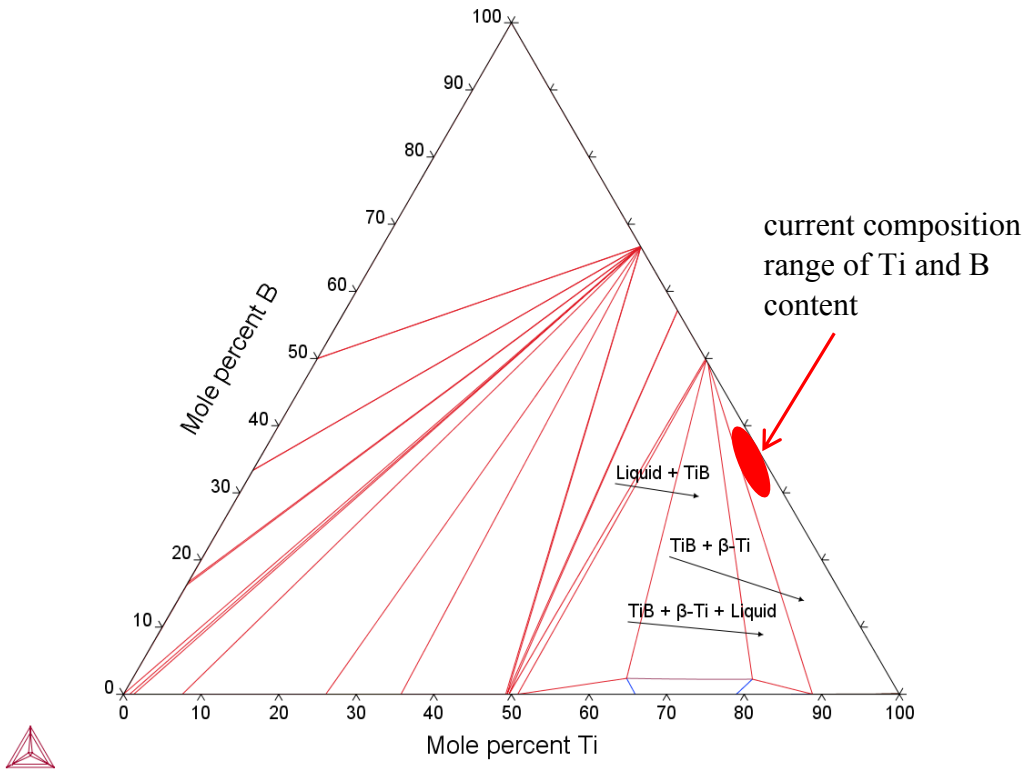


Fig. 3.4 Ternary Ti-B-Fe phase diagram at 1200˚C.

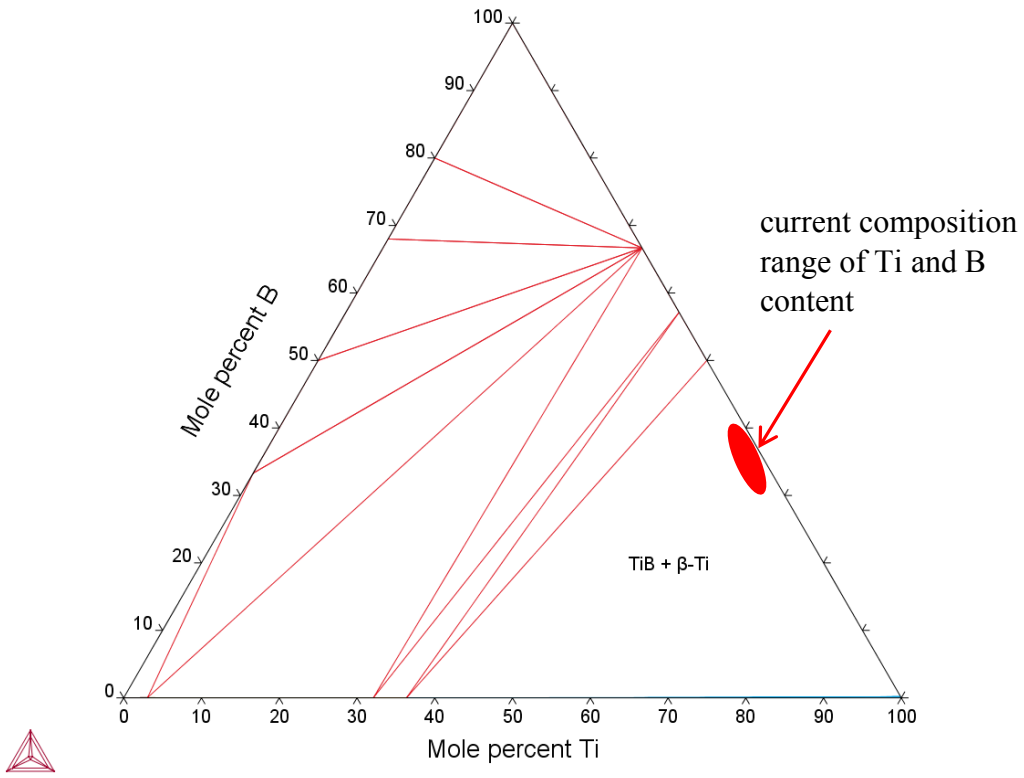


Fig. 3.5 Ternary Ti-B-Mo phase diagram at 1200˚C.

### 3.1.3 Quaternary Systems

3.1.3.1 Optimization of the Fe:Mo Ratio

The emphasis of initial experimentation during this research was placed on this point: to optimize the ratio of Fe:Mo within a cermet Ti-B-Fe-Mo composition. As a starting point, a high end of the cermet range of volume percent reinforcing materials was chosen at 70 volume percent TiB. It was determined using the beta-stabilizing principles discussed in Section 2.2.3 that at 70 volume percent TiB, if at least 6.4 weight percent of the starting powders were beta-stabilizers, they would be sufficient for creating at least a metastable beta alloy. The natural question arising from this decision is, “Why not add more beta-stabilizers to make the samples fully stable instead of metastable?” Previous synthesis of samples in the research group had shown that there is a high risk of forming

undesirable intermetallic compounds with the addition of some beta-stabilizers, especially Fe. The Ti-Fe binary phase diagram in Figure 3.3 shows the ubiquitous presence of the TiFe phase. Avoiding the formation of this phase was vital to the goals of the research.

Additionally, it was intended that the dual properties of Fe and Mo additions be preserved. It is possible that using only Mo as a beta stabilizer would eliminate the potential for some intermetallics, but the processing conditions aided by the presence of Fe would be lost. It was not in the interest of this research to use only one beta-stabilizer and lose this duality. This, then, brought about issues of processing practicality. A temperature high enough to achieve full densification of samples was desired, but with the presence of Fe, raising the processing temperature increases the risk of liquid phase. When sample powders are raised to temperature under the pressure of hydraulic rams during electric-field-activated sintering, liquid metal has potential to be pushed out of the graphite die, ruining the sample. Thus, the solution was to have a combination of Fe and Mo starting powders of high enough weight percent to allow for beta stabilization at least in a metastable fashion, but low enough weight percent to avoid intermetallics and difficulties in processing.

After weighing these considerations, the first samples were designed at an intended final volume percent of 70 TiB. The Fe:Mo ratio was varied in three variations of 40:60, 50:50 and 60:40, by weight. Thermo-Calc was used to design these three compositions. This ratio variation was chosen because it varied the beta-stabilizer content near the eutectoid point involving the beta-Ti + TiB phase field (see Figure 3.6). This point was strategic because this would allow the beta phase to be stable until the lowest

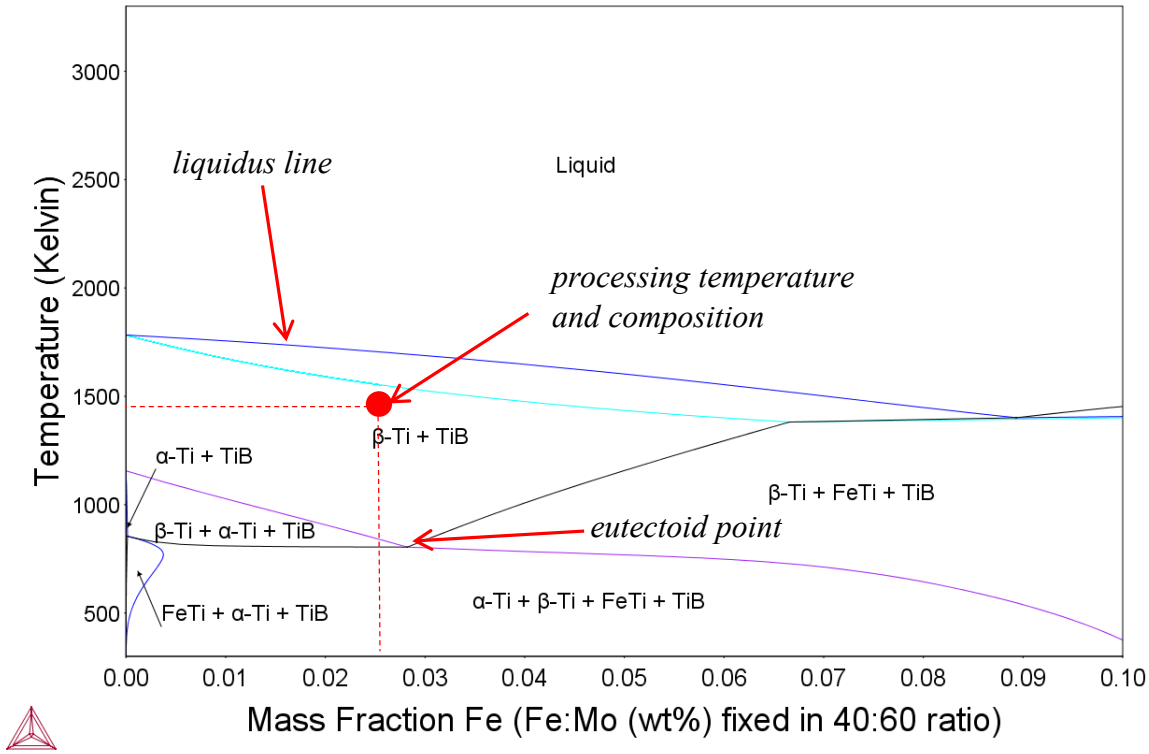


Fig. 3.6 Quaternary Ti-B-Fe-Mo phase diagram. TiB is fixed at 70 vol.% and Fe:Mo is fixed in a 40:60 wt.% ratio (for every 1 wt.% Fe, there is 1.5 wt.% Mo).

possible temperature during the cooling process after sintering, to the end of diminishing the occurrence of formation of phases other than beta. Figure 3.6 shows the processing parameters of a 70 volume percent TiB, 40:60 Fe:Mo sample. A sintering temperature of 1473 K was chosen because this was well within the beta phase and near but not above the liquidus line. Getting close to the liquidus line during processing was designed to increase densification of samples by having near-liquid phase reaction sintering.

Figure 3.7 shows the processing parameters of a 70 volume percent TiB, 50:50 (by weight) Fe:Mo sample. Little of the overall phase diagram appearance changed from Figure 3.6, with the exception of a small expansion of the beta-Ti + TiB phase to the right around 0.07 mass fraction Fe and an increase in area of the FeTi + alpha-Ti + TiB phase.

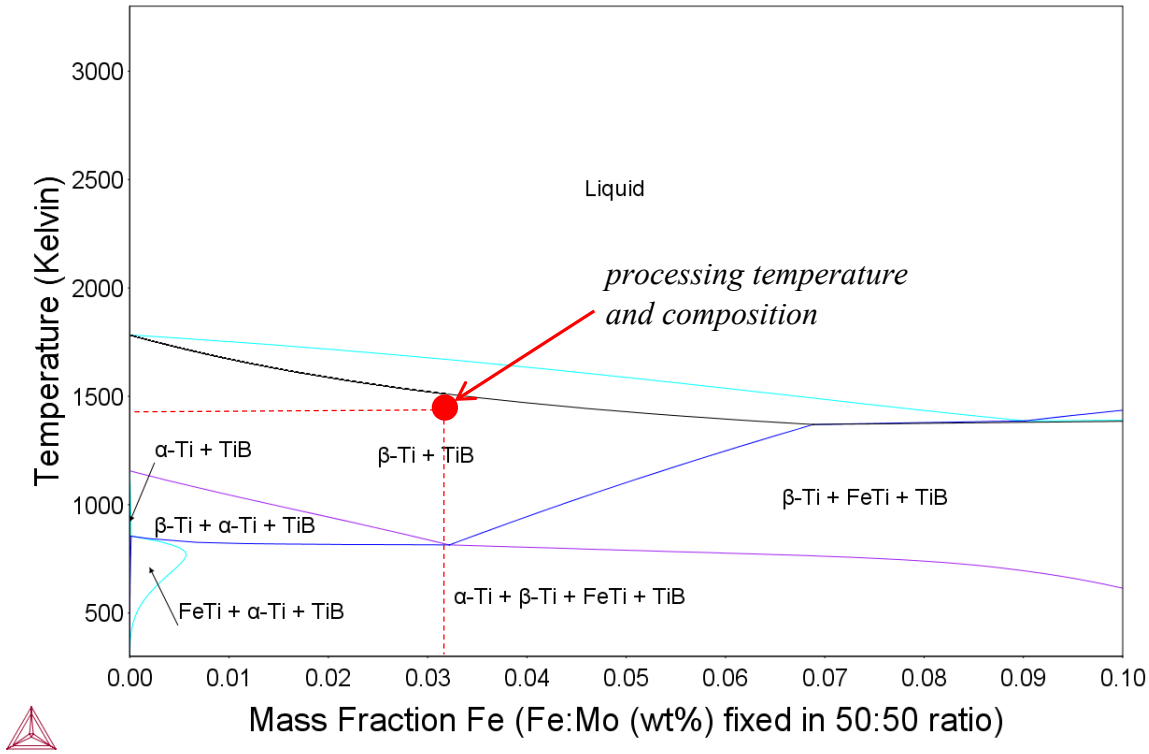


Fig. 3.7 Quaternary Ti-B-Fe-Mo phase diagram. TiB is fixed at 70 vol.% and Fe:Mo is fixed in a 50:50 wt% ratio (for every 1 wt.% Fe, there is 1 wt.% Mo).

This sample composition is closer to the eutectoid point than the sample in Figure 3.6.

Figure 3.8 shows the processing parameters of a 70 volume percent TiB, 60:40 (by weight) Fe:Mo sample. The same changes occurred in this sample due to an increase in Fe content, namely the small expansion of the beta-Ti + TiB phase to the right, around 0.07 mass fraction Fe, and an increase in area of the FeTi + alpha-Ti + TiB phase. Keeping at the same operating temperature of 1473 K to be consistent among samples pushed the processing of this composition very near the liquidus line. There was some minute evidence of liquid phase metal being forced out of the die during sample processing. The differentiation among products from these three sample designs is discussed in Chapter 5.

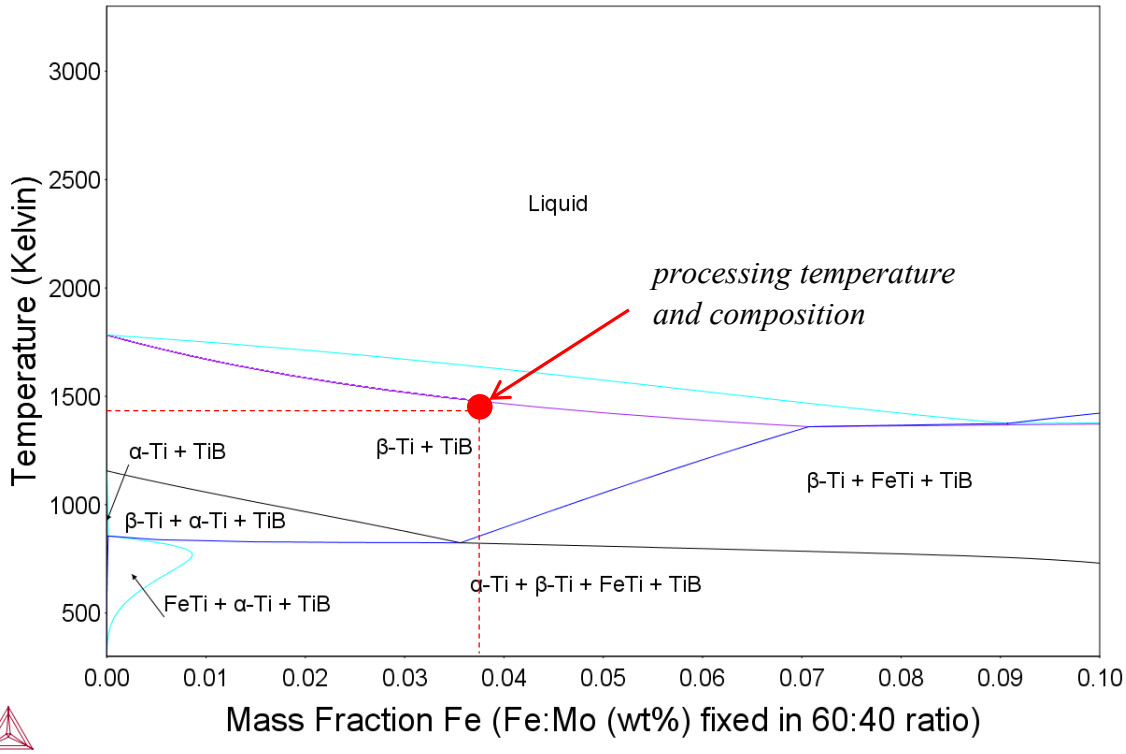


Fig. 3.8 Quaternary Ti-B-Fe-Mo phase diagram. TiB is fixed at 70 vol.% and Fe:Mo is fixed in a 60:40 wt% ratio (for every 1.5 wt.% Fe, there is 1 wt.% Mo).

3.1.3.2 Variation of TiB Volume Percent

The second stage of design and analysis of a Ti-TiB cermet, predicated upon finding an optimal Fe:Mo ratio (by weight), was to vary the TiB volume percent in order to achieve a desired morphology and eventually compare trends in mechanical properties. A range of 50 to 70 volume percent TiB was targeted. A fixed Fe:Mo ratio of 40:60 by weight was chosen based on analysis of morphology in micrographs, as discussed in chapter 5. Samples of 50 and 60 volume percent TiB, in addition to the 70 volume percent TiB sample of Figure 3.6, were synthesized. Just as in Section 3.1.3.1, these CALPHAD designs in Thermo-Calc were used to determine processing parameters for

sintering of these particular compositions.

Figure 3.9 shows the processing parameters of a 60 volume percent TiB, 40:60 Fe:Mo (by weight) sample. The amount of TiB is lower than the 70 volume percent TiB samples and the amount of residual titanium postreaction is higher. Thus, there is a wider processing range for the beta-Ti phase. This sample is a little further away from the eutectoid point compared to the sample in Figure 3.6, and thus has more chance of forming additional phases during processing, such as alpha-Ti. The same sintering temperature of 1200˚C was used, as it falls comfortably within the beta-Ti + TiB phase field.

Figure 3.10 shows the processing parameters of a 50 volume percent TiB, 40:60 (by weight) Fe:Mo sample. Once again, the range at which beta-Ti phase is stable has been widened to beyond 10 weight percent Fe. This sample, falling further away from the eutectoid point than the sample in Figure 3.9, also runs a slightly higher risk of developing unwanted phases. The temperature 1200˚C falls within the beta-Ti phase field but still near enough to the liquidus line for good sintering kinetics.

The remaining scope of this work was based on CALPHAD analysis performed in this chapter. Samples were prepared for synthesis and subsequent analysis using the Thermo-Calc plots described in Section 3.1.3.

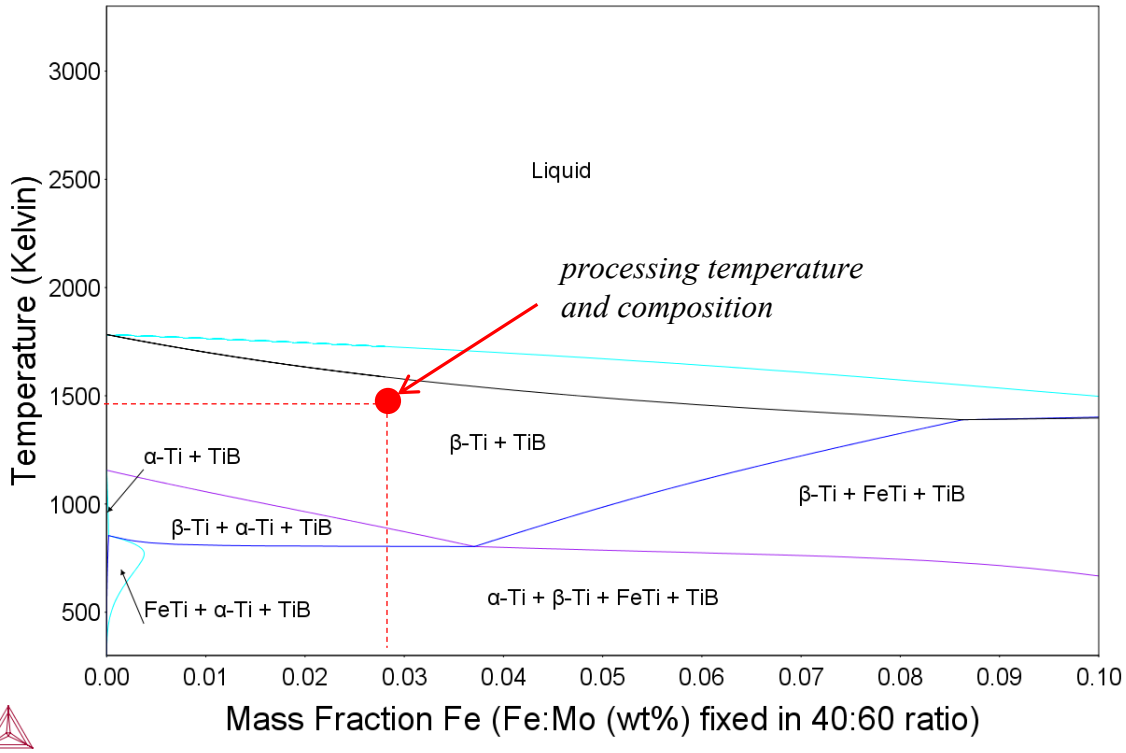


Fig. 3.9 Quaternary Ti-B-Fe-Mo phase diagram. TiB is fixed at 60 vol.% and Fe:Mo is fixed in a 40:60 wt.% ratio (for every 1 wt.% Fe, there is 1.5 wt.% Mo).

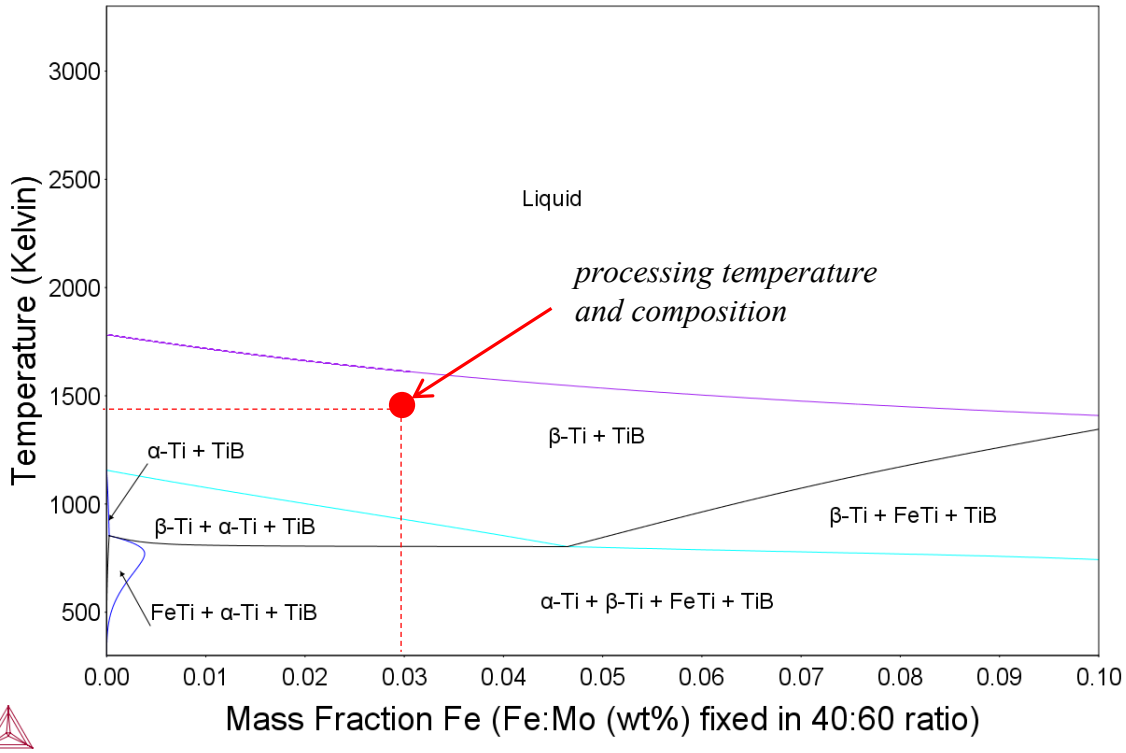


Fig. 3.10 Quaternary Ti-B-Fe-Mo phase diagram. TiB is fixed at 50 vol.% and Fe:Mo is fixed in a 40:60 wt.% ratio (for every 1 wt.% Fe, there is 1.5 wt.% Mo).

# CHAPTER 4

# EXPERIMENTAL PROCEDURE

## 4.1 Powder Preparation

High purity Ti powders in the size range of 30 to 40 μm used in this study were supplied by Puris, LLC (recently acquired by Carpenter Technology Corporation). $TiB_2$ powders in the size range of 3 to 5 μm were supplied by Momentive Performance Materials. Ti and Fe powders in the size range of 10 to 15 μm were supplied by Alfa Aesar. These powders were used as the starting materials for mixing compositions according to the CALPHAD designs in Chapter 3.

The trimodal size ratio of 3:10:40 ($TiB_2$:Fe/Mo:Ti), as discussed in Section 2.2.2 was important to optimizing packing density. It is estimated that these size ratios bring the maximum packing density to 85% or higher [52,53]. The powders were weighed according to design and placed in a stainless steel tumbling canister with side wall lifters to assist in tumbling. Ti mixing balls of ¼" diameter were added to assist in homogenization of mixing. The canister was placed on a tumbling rack to mix. The canister was allowed to fill with atmospheric air as opposed to an inert atmosphere. Measurement by the research group using a LECO electrode furnace showed that the difference in final oxygen content of post-sintered samples was negligible between sample powders mixed in inert atmosphere versus air. This is most likely due to the

natural formation of a passivating layer of oxygen on the Ti powders that shields the powders so oxygen content changes negligibly during mixing. The sample mixtures of the first batch of samples in which optimization of Fe:Mo ratio was being analyzed are shown in Table 4.1.

The second batch of samples in which the effect of changing TiB volume percent was analyzed are also contained in Table 4.1. These samples were mixed according to the same methods as the previous samples. Included in this study of varying TiB content is the first sample entry from the table with the same Fe:Mo ratio of 40:60 by weight. The mixtures from this portion of the study were repeated several times during the course of the research as more samples were made for mechanical testing. This proved that sample synthesis had good repeatability in sintering and mechanical properties.

Table 4.1 Powder proportions and mixture identities for studying the effect of varying Fe:Mo wt.% ratio and TiB vol.%.

| Name | Composition by wt.% Starting Powders | | | |
|---|---|---|---|---|
| Powder Mix Name | Ti | $TiB_2$ | Fe | Mo |
| TiBFeMo, 70 vol.% TiB, 40:60 (wt.%) Fe:Mo | 52.6 | 41.0 | 2.5 | 3.8 |
| TiBFeMo, 70 vol.% TiB, 50:50 (wt.%) Fe:Mo | 52.6 | 41.0 | 3.2 | 3.2 |
| TiBFeMo, 70 vol.% TiB, 60:40 (wt.%) Fe:Mo | 52.6 | 41.0 | 3.8 | 2.6 |
| TiBFeMo, 50 vol.% TiB, 40:60 (wt.%) Fe:Mo | 62.8 | 29.6 | 3.1 | 4.6 |
| TiBFeMo, 60 vol.% TiB, 40:60 (wt.%) Fe:Mo | 57.5 | 35.5 | 2.8 | 4.2 |

## 4.2 Reaction Sintering

The reaction sintering process is a vital component of this research process. It utilizes the chemical reaction of the mixed starting powders depicted in Equation 4.1. β(Ti,X) represents the beta-Ti phase with solid solution elements of Fe and Mo. (Ti,X)B represents TiB with possible ternary elements of Fe and Mo making ternary borides.

$$TiB_2 + Ti + X(Fe, Mo) \rightarrow \beta(Ti, X) + (Ti, X)B \quad (4.1)$$

The electric-field-activated sintering equipment used on this project was designed by Thermal Technology, LLC (formerly GT Advanced Technologies). The sintering process is performed in a chamber under an inert argon atmosphere. The graphite die is prepared by lining it with graphite foil. This is to prevent direct reaction between the die and the metal powders. The mixed starting powders are poured into the lined die and lightly pressed to ensure the powders are in a uniform disk shape. Then graphite plugs are placed in the die on the top and bottom of the powder disk, and the whole apparatus (lined graphite die, powders, and plugs) is placed inside the sintering chamber between the hydraulic rams. A pressure of 5 MPa is immediately applied to the sample in preparation for beginning the sintering program.

The sintering program is a one-step process of heating, holding at temperature, and cooling. The sintering program is a temperature-controlled program. There is a thermocouple inserted into the graphite die near the sample powders that monitors the temperature at the center of the die. This temperature reading is transferred to the monitoring software, which tailors the voltage and current as needed to keep the sample at the temperature dictated by the program.

The temperature versus time profile for part synthesis is shown in Figure 4.1. The

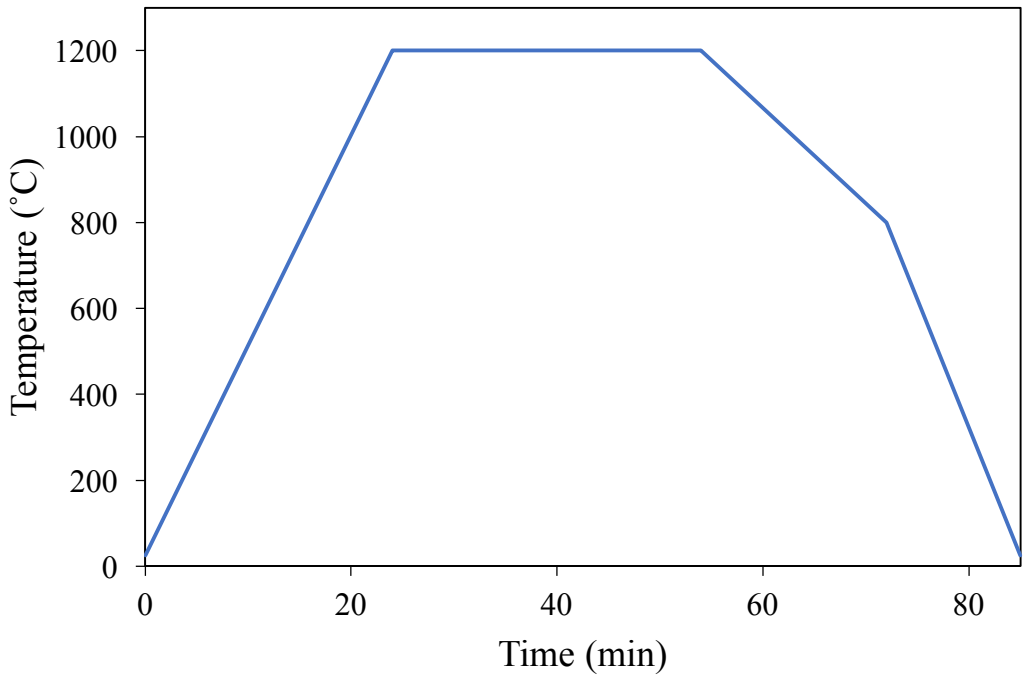


Fig. 4.1 Temperature versus time sintering profile used for synthesis of samples.

samples are heated to the desired sintering temperature of 1200˚C (1473 K), as designed from CALPHAD calculations, and at a rate of 50˚C/min. The samples were held at temperature for 30 minutes. The 30-minute hold time was designed to ensure that a full reaction had taken place as well as full densification. It is possible to sinter a sample with no hold time, but results are more variable. Following the hold time, a controlled cooling stage began that slow-cooled the samples at a rate of 22.5˚C/min to a temperature of 800˚C, after which the power was shut off and the sample allowed to air cool as fast as possible to room temperature. This slow-cooling was designed to avoid thermal shock to the graphite die and sample, which could lead to cracking but may also contribute to the formation of unwanted phases, as discussed in Section 2.2.4.

The pressure versus time profile during synthesis of parts is depicted in Figure 4.2. The starting pressure of 5 MPa is held during the heating portion of the sintering

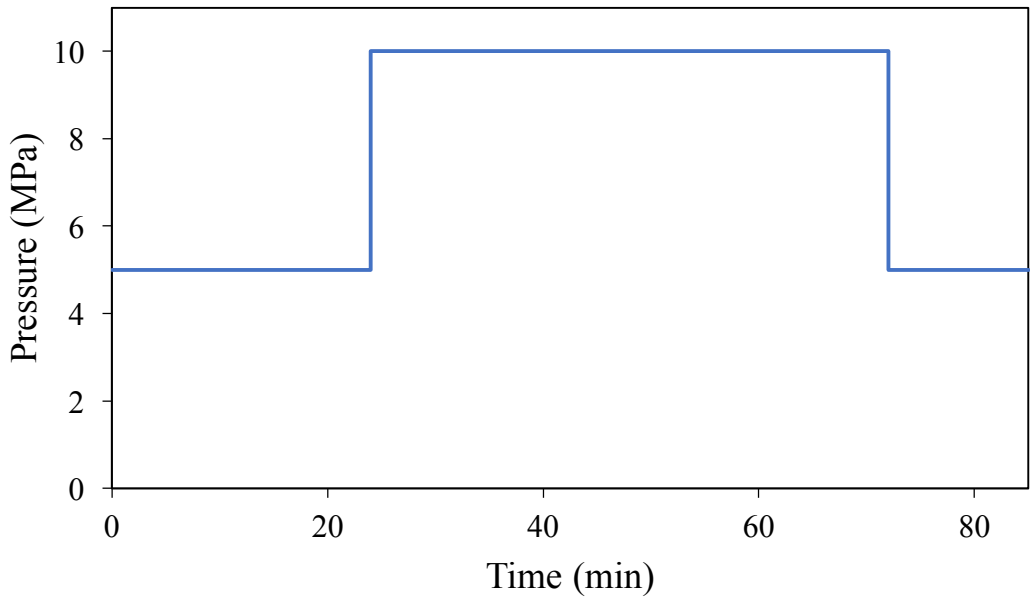


Fig. 4.2 Pressure versus time sintering profile for synthesis of samples.

program, after which a pressure of 10 MPa is applied. The applied pressure is important for densification of the samples. The 10 MPa pressure is held constant through both the 30-minute hold time and the controlled cooling to 800˚C. The air-cooling stage of the sintering process is done at the starting pressure of 5 MPa.

The effect of the application of pressure can be observed in Figure 4.3. During sintering, the hydraulic ram position is monitored. The starting position of the ram is somewhat arbitrary because it can be different depending on preparation of the sample die. This machine output offers real-time reflection of sintering behavior during the sintering process. In the ram displacement curves for all five samples, there is an initial thermal expansion followed by the first dip around 1000 seconds when the samples reach the transition temperature between the alpha-Ti and beta-Ti phases around 884˚C (see Figure 2.1 and Figure 2.6). This phase change and densification continues as the sample climbs to 1200˚C. The second and larger dip observed around 1500 seconds represents

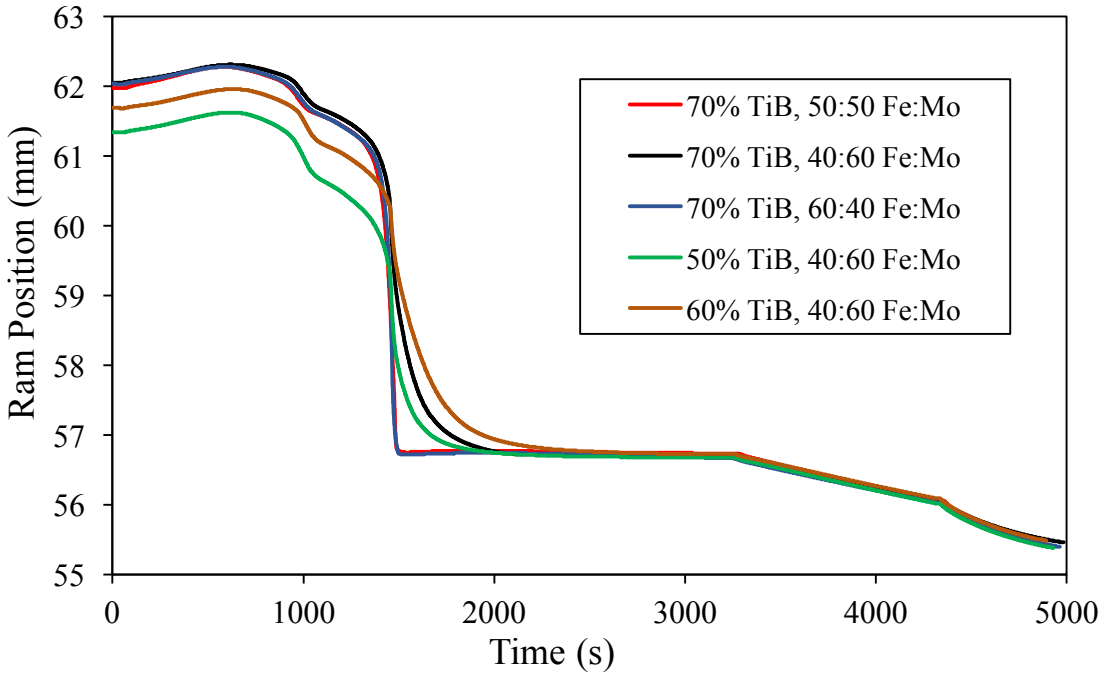


Fig. 4.3 Ram position versus time during synthesis of samples.

when the sample reaches 1200˚C and 10 MPa pressure is applied. The ram drops quickly as the samples immediately densify under pressure. Lastly, another significant observation from this graph is that the two samples with higher Fe content (50:50 Fe:Mo and 60:40 Fe:Mo) immediately densify almost to completion when the higher pressure is applied. This confirms the predictions from CALPHAD calculations that the presence of Fe aids in densification during sintering. The samples with 40:60 Fe:Mo ratio took a little more time to reach the same level of densification by comparison, which also means the hold time during processing is important. Beyond 2500 seconds, all the samples reach nearly identical densification according to this figure.

The temperature versus time curve (Figure 4.1) is reflected in the power versus time output, which is depicted in Figure 4.4. The ramp up to temperature shows an increasing need for power until 1500 seconds when the desired temperature is reached

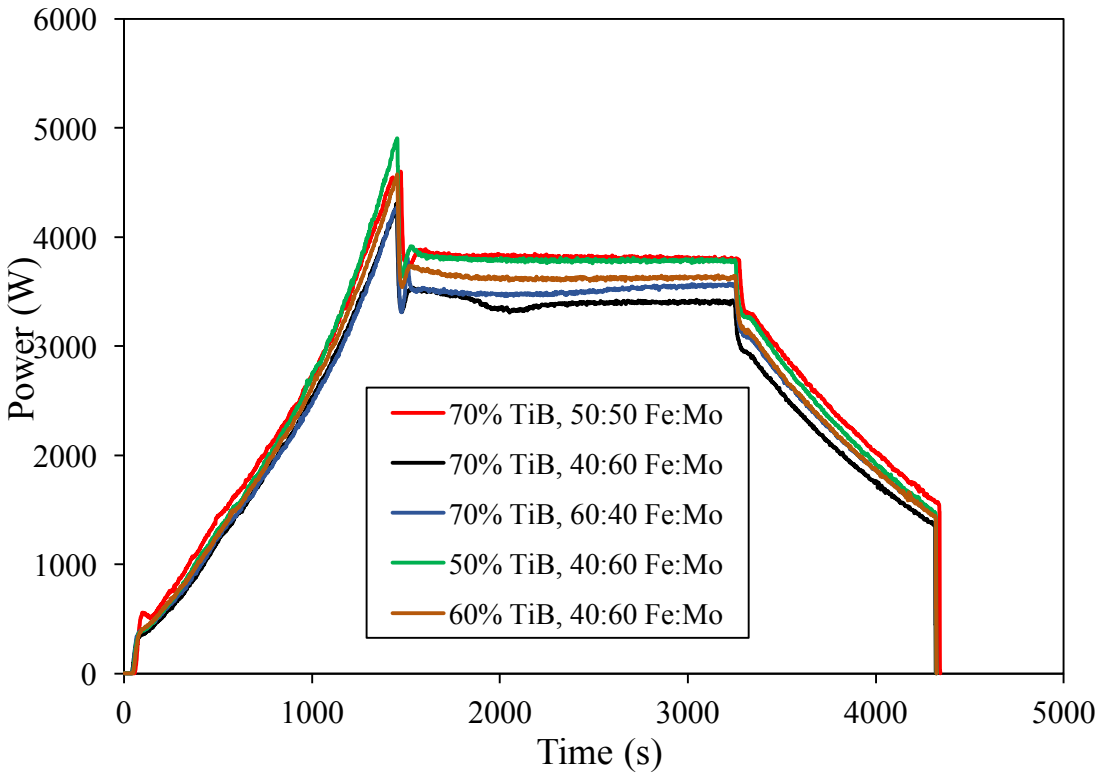


Fig. 4.4 Power versus time during synthesis of samples.

and the machine adjusts power to maintain temperature during the 30-minute hold time. The controlled cooling period is shown by decreasing power usage between about 3300 seconds and 4300 seconds, after which the power is shut off for the fast cooling stage.

Following the sintering process, samples are removed from the die and sent to be machined to size by electric discharge machining (EDM). It is thermodynamically favorable for some of the powders being used to form carbides during sintering when in the presence of carbon. Because the powders are sintered in direct contact with graphite foil, a layer of carbon compounds forms on the outside of the samples. This carbon layer is machined off before samples are cut to shape for microstructural analysis or mechanical testing because the carbon layer would alter the observable properties of the samples.

### 4.3 Microstructural Characterization

After being EDM machined, samples to be prepared for microstructural characterization first underwent a grinding process whereby successive grits of SiC grinding papers were used to achieve a fine finish of about 15 μm. The samples were then polished to a mirror finish using colloidal silica slurries, the finest of which was 0.3 μm in size. Lastly, etching was performed using a modified Krolls reagent containing deionized water, hydrofluoric acid, nitric acid, and glycerol for uniform wetting of the sample surface.

Low magnification characterization of microstructure was performed using optical microscopy. High-magnification microscopy was performed using a scanning electron microscope (SEM). Typically, the SEM was operated at parameters of 20 kV and 15 μA, except where charging of the sample surface became problematic.

Phase analysis was performed using X-ray diffraction (XRD) techniques. The samples were analyzed using XRD after polishing but before etching, so the change in surface topography due to etching would not impact the results. The XRD was programmed to assess between the 2θ extremes of 20 and 80 degrees at a step size of 0.02 degrees and a scanning rate of 2 degrees/min. The X-ray generator was operated at 40 kV and 15 mA using Cu $K_\alpha$ radiation.

Peaks were indexed according to available XRD indexing cards. Design of TiB volume percent and powder mixtures was based on the assumption that all B in $TiB_2$ reacts during sintering to form TiB. The volume percent of the 50, 60 and 70 volume percent TiB samples were verified within acceptable error from XRD diffraction peaks using a quantitative estimation method established by this research group [48]. Using this

method, the intensity peaks of each XRD result are integrated under the assumption of the peaks being Gaussian in form. The integrated areas are then used to calculate ratios of phases present by volume.

## 4.4 Mechanical Property Evaluation

### 4.4.1 Vickers Hardness

Hardness of samples was evaluated using a Vickers microhardness indenting system. The samples were hardness tested after polishing and before etching in order to avoid measurement error to differences in surface topography. Using established methods of Vickers indentation, a square-tipped diamond indenter with a load of 1000 gf was used to indent the samples. A calibrated microscope was then used to measure the length of both diagonals across the diamond indentation. These two diagonals were averaged to a value, $d$ (in mm), which was used along with $L$ (load in kg) to calculate Vickers Hardness Number according to Equation 4.2. Vickers hardness is reported in this thesis in units of kgf/mm$^2$.

$$VHN = \frac{L(2\sin 2)}{d^2} = \frac{L(1.8544)}{d^2} \tag{4.2}$$

### 4.4.2 Flexural Strength

Flexural strength testing was performed in as close accordance as possible with the ASTM standard test method for flexural strength in advanced ceramics [65]. This standard was designed for used with ceramics and whisker-reinforced ceramics. The cermet samples in this study are not considered fully ceramic because of their high metallic content of 30 to 50 volume percent. However, they are also not considered

metallic enough for flexural strength analysis of metals because of the high ceramic content. This test method, therefore, was chosen for practicality. It applies to cermets as closely as possible and has a sample size requirement that is much easier to adhere to than the metallic material size requirement using the sintering method mentioned above.

Samples from the 50, 60 and 70 volume percent TiB with 40:60 Fe:Mo (by weight) ratio compositions were synthesized for this strength testing. The samples were cut to the recommended size of 45 x 3 x 4 mm by EDM machining. The copper-containing surface melt inherent in EDM machining was ground off with SiC grinding papers. As in grinding for microstructural characterization, the samples were ground until a flat surface with a finish of 15 μm was obtained. This fine grinding was to ensure that crack propagation during testing did not originate from surface scratches but from bulk material properties.

The samples were tested using an MTS load frame and a four-point bending configuration designed according to the ASTM standard (Figure 4.5), where L is 40 mm [65]. To test samples, the load frame applied a uniaxial force through the rollers, with the

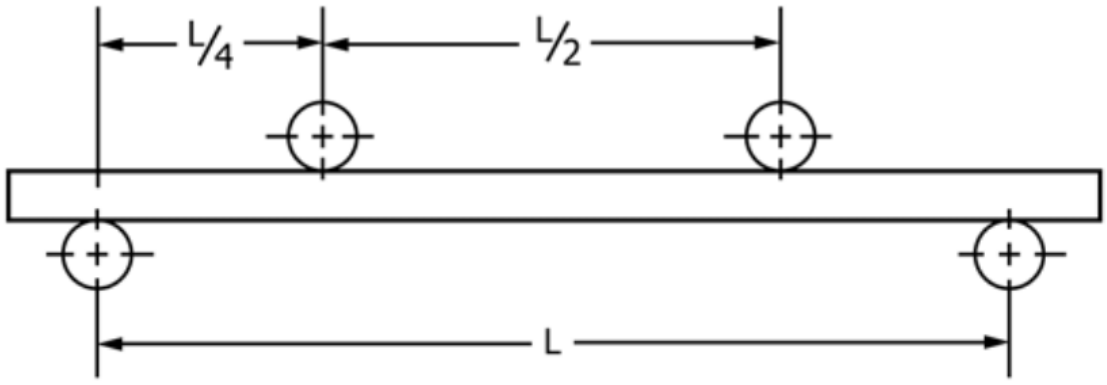


Fig. 4.5 Four-point bending configuration for material testing. Adapted from [65].

rollers in direct contact with the 4 mm-wide faces of the sample bar. The flexural testing is a displacement-controlled test in which the sample bar is forced to flex by a controlled rate of displacement and the force exerted by the bar back on the rollers is recorded up until the point of fracture. The flexural strength, in MPa, was evaluated using Equation 4.3, where $P$ is force at point of fracture (N), $L$ is outer support span (mm), $b$ is specimen width (mm), and $d$ is specimen thickness (mm).

$$S = \frac{3PL}{4\,bd^2} \tag{4.3}$$

Following flexural strength testing of samples, fracture surfaces were characterized using the same SEM techniques described in Section 4.3. Probability of fracture and Weibull modulus were calculated to characterize materials.

### 4.4.3 Fracture Toughness

In similar fashion to the testing for flexural strength, fracture toughness evaluation of materials was performed in as close a fashion as possible to the ASTM standard test method for fracture toughness of advanced ceramics [66]. Once again, the test method for ceramics applied to these cermets more practically than the metal test method. The testing system configuration was very similar to that of flexural strength testing. The same four-point bending configuration was used (Figure 4.5) and the same MTS load frame.

Preparation of samples for toughness testing is more complicated and nontrivial compared to flexural strength testing. Fracture toughness testing requires the initiation of a small precrack, which falls within a specified range of distance through the thickness of the sample. Because these cermets behave as neither ceramics nor metals, slight steps outside the bounds of the ASTM standard had to be taken to form these precracks.

As in Section 4.4.2, samples from the 50, 60, and 70 volume percent TiB with 40:60 Fe:Mo (by weight) ratio compositions were synthesized for this strength testing. Sample bars were cut to the same 45 x 3 x 4 mm size as in flexural testing. Sample preparation began by fine grinding to the level described in Section 4.4.2. Once a clean surface was obtained, a precrack needed to be initiated. There are several methods of precracking the samples allowable in the ASTM standard. This research used the precracked beam test specimen method. The initiation of a precrack by this method generally has two steps: prepare the surface for cracking by notching or indenting, then use a gapped precrack block to force a precrack with compressive force. The simplest crack-starting method in the ASTM standard is indentation of sample surface using a square Vickers indenter. The indentations must be evenly spaced and one diagonal of the indentation must be perpendicular to the side face of the sample. Through trial and error, it was found that five indentations in the 3 mm-wide face of the sample bars were sufficient for the 70 volume percent samples (Figure 4.6). These samples were then placed in a fixture with a 6 mm gapped precrack block and placed under increasing compressive force until a “pop-in” sound is heard signaling the rapid connection of a precrack linking all the indentations, as depicted in Figure 4.7. The precrack is supposed to extend through the width of the sample in the range of 35 to 60% and keep a generally straight line, as depicted in Figure 4.8.

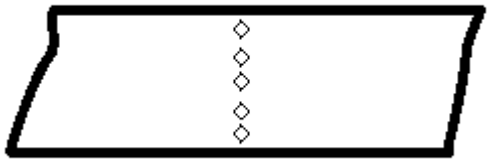

Fig. 4.6 Indentations to initiate crack in fracture toughness test specimen.

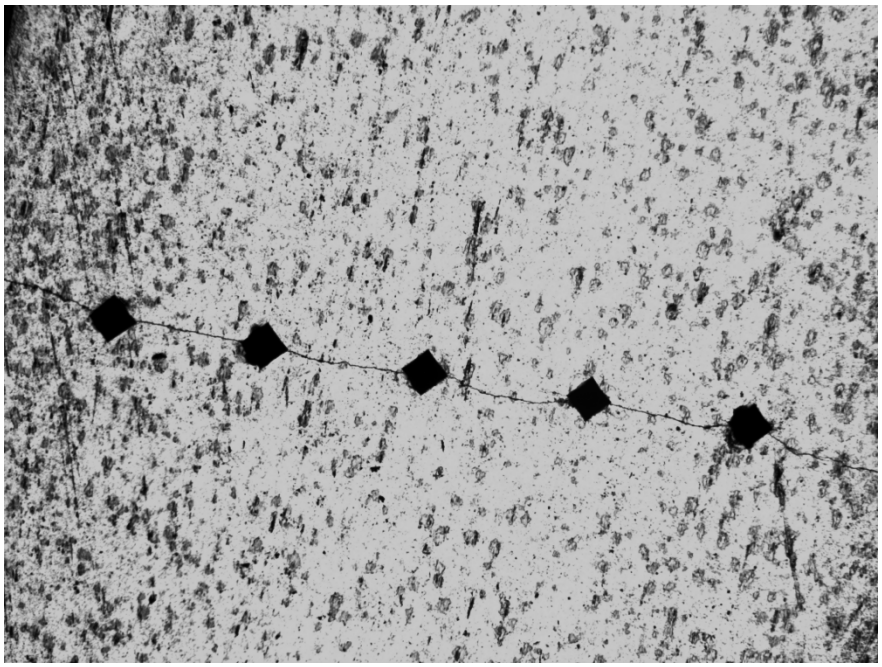

Fig. 4.7 Precrack linking indentations in fracture toughness test specimen.

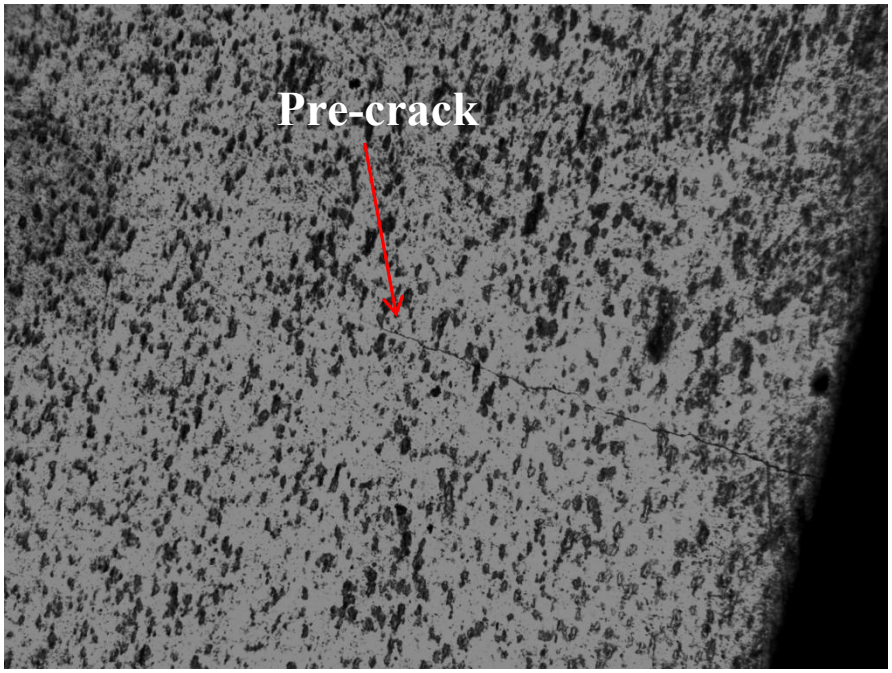


Fig. 4.8 Side view of precrack extending from indentations.

Because the samples with 50 and 60 volume percent TiB had such high metallic content increasing their resistance to precracking, the indentation method used above did not work for these samples. Slight adjustments were made to the ASTM methods in order to create the necessary precrack in these samples.

It was decided that a saw notching method would be more effective at initiating a crack in these sample bars. Because of the high hardness of TiB, standard machining tools such as high-speed steels have difficulty scoring a notch in these samples. It became necessary to use EDM machining again to notch these samples. The samples were notched with a 0.5 mm notch according to the drawing in Figure 4.9. This notch was treated as the indentations were treated in the 70 volume percent composition as a crack initiation point.

Another slight adjustment to the ASTM standard methods came from the needs arising from this EDM notch method. After notching, precracking was attempted using the 6 mm gapped precrack block without success. The ASTM standard limits the block gap to 6 mm, but it was necessary to widen the gap for these cermet samples in order to increase the bending moment at the bar notch. Therefore, a precrack block with an 8 mm gap was designed as depicted in Figure 4.10. In order to precrack, the notched section of the bar is placed downward facing the gap in the block. When uniaxial compressive force is applied, the notch is forced open, initiating a crack. The resulting cracks appeared as depicted in Figure 4.11.

Once precracks were obtained in all the compositions, the cracks were infiltrated with magnaflux dye (mixed in a ratio of 1.5 DI water: 1 magnaflux). This was for the purpose of measurement after testing.

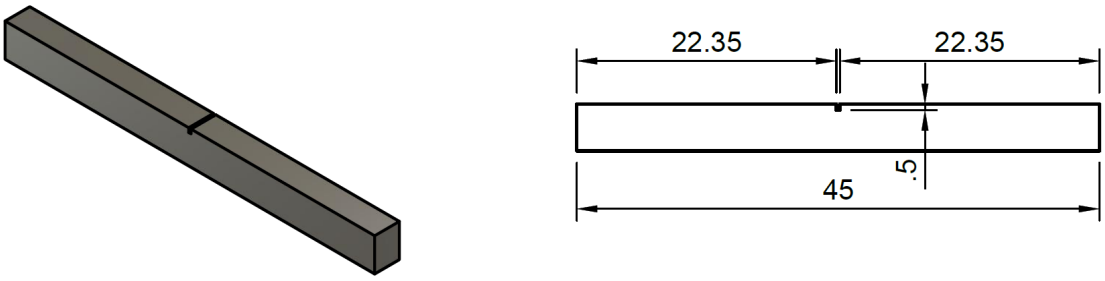


Fig. 4.9 EDM notch dimensions of fracture toughness specimen (mm).

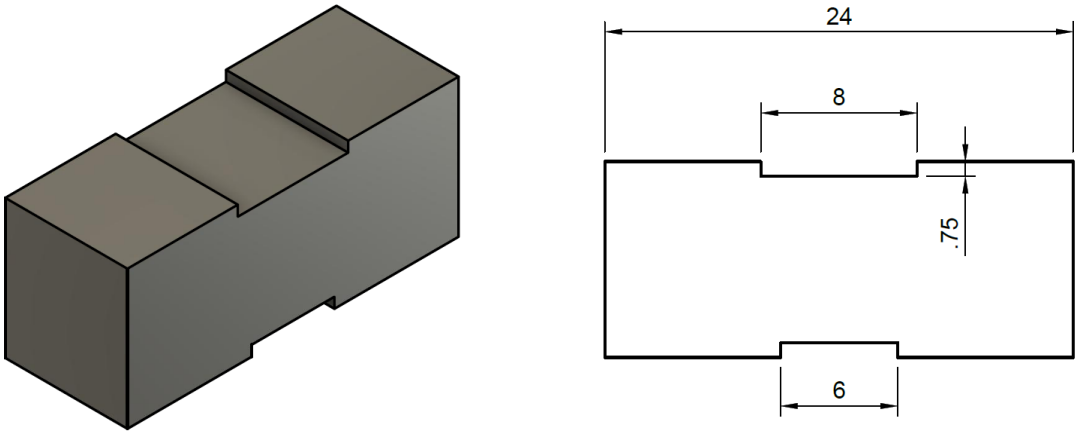


Fig. 4.10 Precrack block dimensions for cracking of fracture toughness specimen (mm).

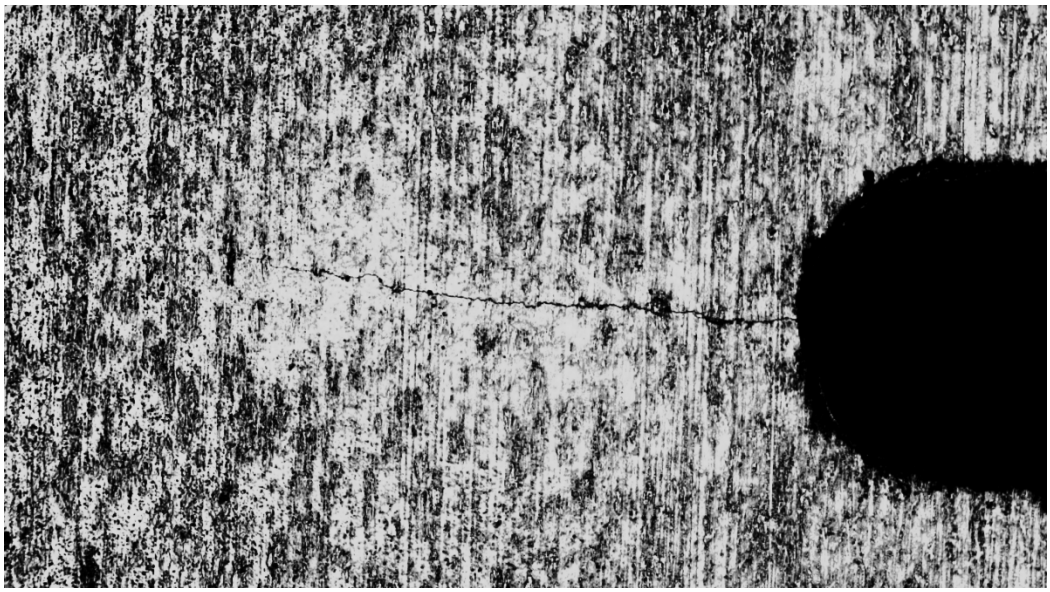

Fig. 4.11 Precrack formed in notched bar for fracture toughness testing.

The four-point testing configuration for fracture toughness has two variations from the parameters for flexural strength testing: the sample is tested with the narrower 3 mm side in direct contact with the rollers so the precrack can grow in line with the direction of force application, and the displacement-controlled testing rate is different. Samples are placed between rollers (similar to Figure 4.5) and uniaxial force is applied and the force the sample exerts in resistance is recorded until complete fracture of sample. After fracture, optical micrographs of the dyed fracture surfaces were taken and ImageJ pixel-measurement software was used to measure the distance the precrack front traveled through the sample initially. An example of the dyed fracture surface is depicted in Figure 4.12. This measurement is used for calculation of toughness.

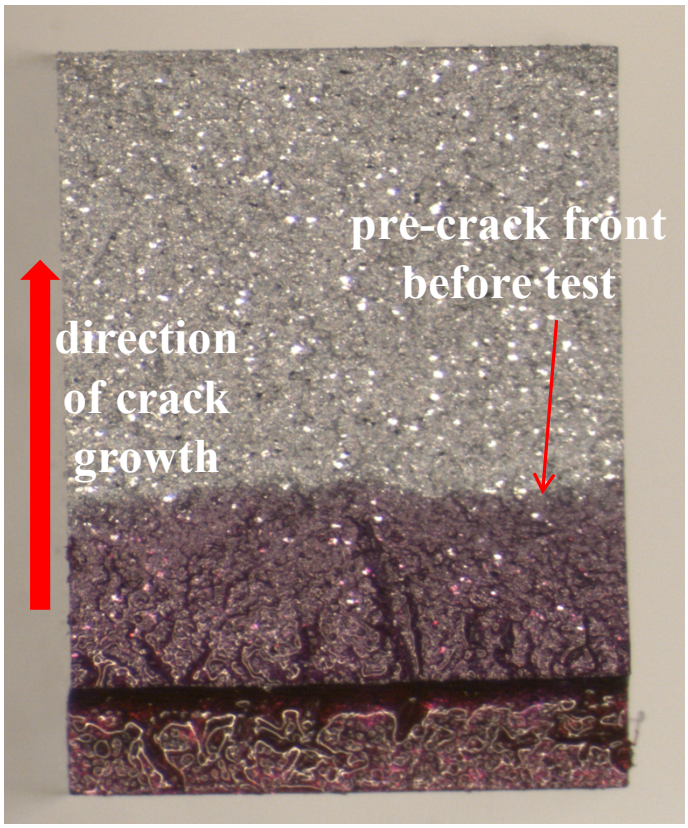


Fig. 4.12 Dyed fracture toughness specimen after fracture.

The equations used for calculation of fracture toughness in four-point bending came from the ASTM standard [66]. Equation 4.4 is the fracture toughness calculation and Equation 4.5 is a parameter calculation used in Equation 4.4, which depends on the calculated length of the precrack through the sample. $K_{Ipb}$ is fracture toughness (MPa√m), $P_{max}$ is the maximum load observed before fracture (N), $S_0$ is outer span of rollers (m), $S_1$ is inner span of rollers (m), $B$ is width of the bar perpendicular to crack depth (m), $W$ is depth of the bar parallel to crack depth (m), and $a$ is crack length measured from micrograph (m).

$$K_{Ipb} = f\left[\frac{P_{max}[S_0 - S_1]10^{-6}}{BW^{3/2}}\right]\left[\frac{3[a/W]^{1/2}}{2[1-a/W]^{1/2}}\right] \quad (4.4)$$

$$f = 1.9887 - 1.326[a/W] - \frac{[3.49 - 0.68[a/W] + 1.35[a/W]^2][a/W][1-[a/W]]}{[1+[a/W]]^2} \quad (4.5)$$

# CHAPTER 5

# RESULTS AND DISCUSSION

## 5.1 Density

After sintering, specimens were EDM-cut to remove surface carbide layers and density tests were performed on all samples. The density was measured by the Archimedes method of measuring displacement of water by the volume of the sample. The results are shown in Table 5.1. It can be seen that all five compositions of this study had a final sintered density of 97% or above. Taking into consideration that there is a possibility of small error in using the Archimedes method, it was assumed for the sake of this study that all of the samples are completely densified. The reaction design of Section 4.2 proved sufficient for densification. Additionally, mechanical testing results showed that samples fractured from causes other than porosity, indicating again that there is a full densification.

## 5.2 Microstructure

### 5.2.1 Optimization of Fe:Mo Ratio

Optimization of the Fe:Mo ratio was investigated by microstructural analysis. The aim of this facet of the project was to determine which combination of beta-stabilizing elements produced the most desirable microstructure. A desirable microstructure in this

Table 5.1 Density measurements of powder mixtures after sintering.

| Name | Composition by wt% Starting Powders | | | | Density, Post-Sintered ($g/cm^3$) | | Density |
|---|---|---|---|---|---|---|---|
| Powder Mix Name | Ti | $TiB_2$ | Fe | Mo | Measured (Archimedes) | Theoretical | % |
| TiBFeMo, 70 vol.% TiB, 50:50 (wt.%) Fe:Mo | 52.6 | 41 | 3.2 | 3.2 | 4.68 | 4.80 | 97.5 |
| TiBFeMo, 70 vol.% TiB, 40:60 (wt.%) Fe:Mo | 52.6 | 41 | 2.5 | 3.8 | 4.69 | 4.81 | 97.5 |
| TiBFeMo, 70 vol.% TiB, 60:40 (wt.%) Fe:Mo | 52.6 | 41 | 3.8 | 2.6 | 4.67 | 4.78 | 97.7 |
| TiBFeMo, 50 vol.% TiB, 40:60 (wt.%) Fe:Mo | 62.8 | 29.6 | 3.1 | 4.6 | 4.72 | 4.87 | 96.9 |
| TiBFeMo, 60 vol.% TiB, 40:60 (wt.%) Fe:Mo | 57.5 | 35.5 | 2.8 | 4.2 | 4.70 | 4.84 | 97.1 |

instance would have the most uniform distribution of phases which would make the mechanical properties of this system the most controllable.

5.2.1.1 Micrographs

The three Fe:Mo ratios (by weight) being investigated were 40:60, 50:50, and 60:40, which were discussed thoroughly in previous sections. Micrographs were taken of samples from each of the three ratios in order to better understand the formation of morphology among the different ratios. Low and high magnification optical micrographs of these samples are shown in Figure 5.1 and 5.2.

Figure 5.1 and 5.2 add second witness to Table 5.1 that the samples are fully dense and free of pores. These figures also highlight the difference in whisker growth

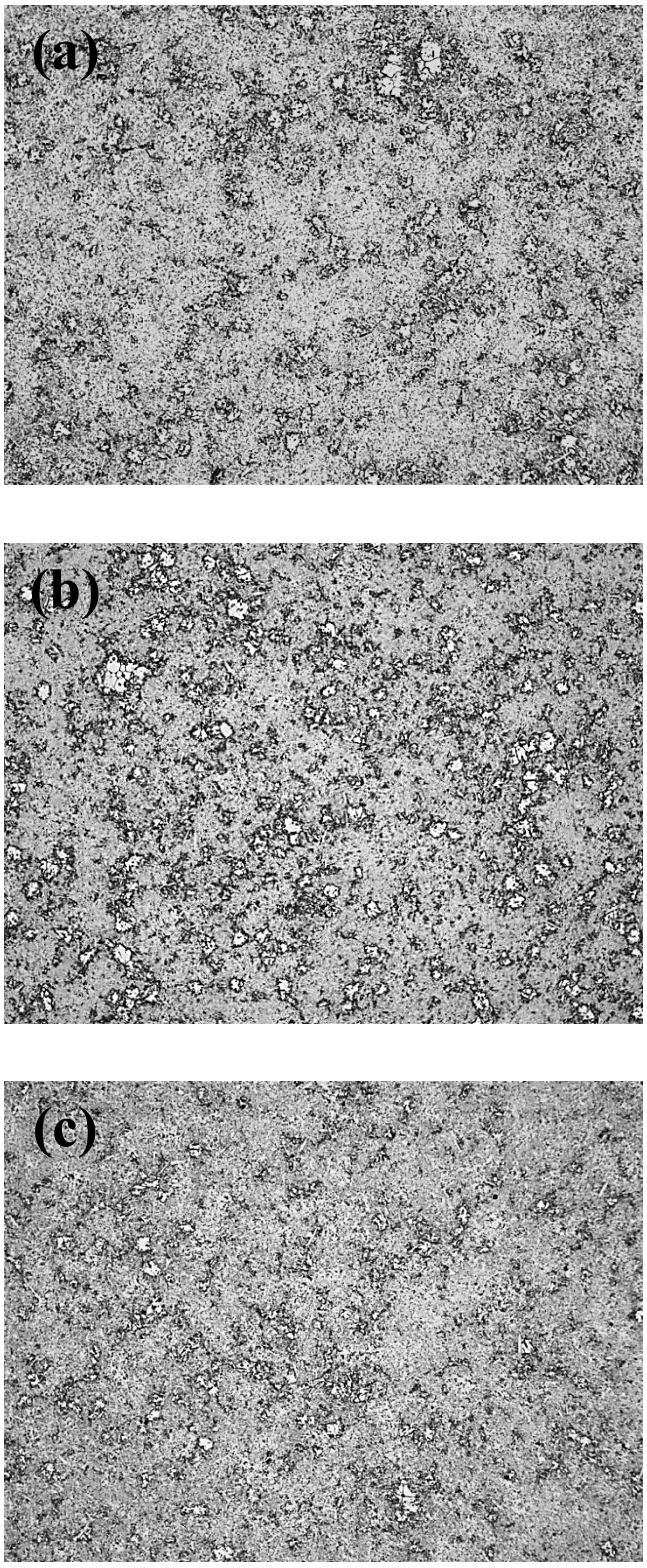


Fig. 5.1 100x optical micrographs of Ti-B-Fe-Mo sample microstructures that have roughly 70 vol% TiB phase in a beta titanium matrix with 6.4 wt.% beta-stabilizer: (a) 70 vol.% TiB, 50:50 wt.% Fe:Mo (b) 70 vol.% TiB, 40:60 wt.% Fe:Mo (c) 70 vol.% TiB, 60:40 wt.% Fe:Mo.

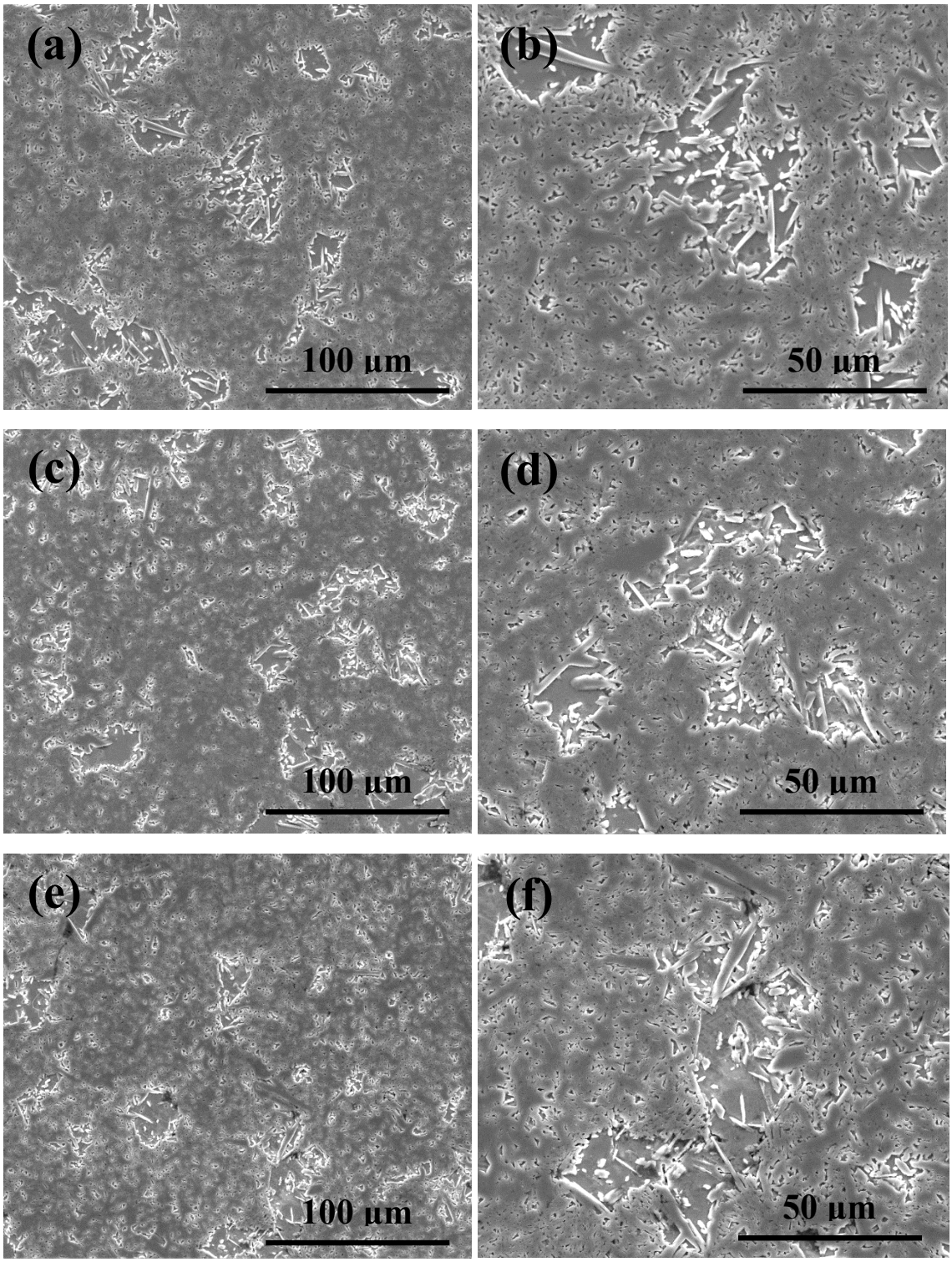


Fig. 5.2 500x and 1000x SEM micrographs of Ti-B-Fe-Mo sample microstructures that have roughly 70 vol% TiB phase in a beta titanium matrix with 6.4 wt.% beta-stabilizer: (a,b) 70 vol.% TiB, 50:50 wt.% Fe:Mo (c,d) 70 vol.% TiB, 40:60 wt.% Fe:Mo (e,f) 70 vol.% TiB, 60:40 wt.% Fe:Mo.

seen among the different Fe:Mo ratios. Sample alloys with 50:50 and 60:40 by weight Fe:Mo ratios in (a) and (c) of Figure 5.1 and (a,b) and (e,f) of Figure 5.2 show smaller whiskers clustered around larger titanium matrix grains. These clusters of small whiskers interspersed with large grains of matrix material are less ideal because the uneven distribution of matrix material would lead to a lapse in toughness. Part (b) of Figure 5.1 and part (c,d) of Figure 5.2 shows that the Fe:Mo ratio of 40:60 by weight promotes more even and optimal whisker and matrix material distribution.

5.2.1.2 XRD Results

The XRD results from this test series in Figure 5.3 show that there was a complete sintering reaction, and there are no residual $TiB_2$ peaks. There is a small percentage of alpha-Ti peaks appearing, which would indicate that the effect of slow-cooling on the metastable alloys did lead to the formation of phases other than beta-Ti. However, there is no indication that intermetallics such as FeTi developed during the sintering reaction.

It can be observed in Figure 5.4 that the β-Ti peaks are showing a consistent shift to the right as Fe content is increased. The lattice d-spacing in β-Ti is decreasing as Fe content is increased. As the beta-Ti peak shifts to overlap the alpha-Ti (101) peak, these beta-Ti peaks may be masking a higher alpha-Ti peak than can be observed at the surface.

It was determined from these micrographs and XRD scans that the 70 volume percent TiB, 40:60 Fe:Mo ratio (by weight) sample showed the best microstructure. It showed the most even distribution of Ti particles within the network clusters of TiB nanowhiskers. This even distribution is important for impeding the progress of cracks through the bulk material, which is a vital characteristic of a cermet. This sample also

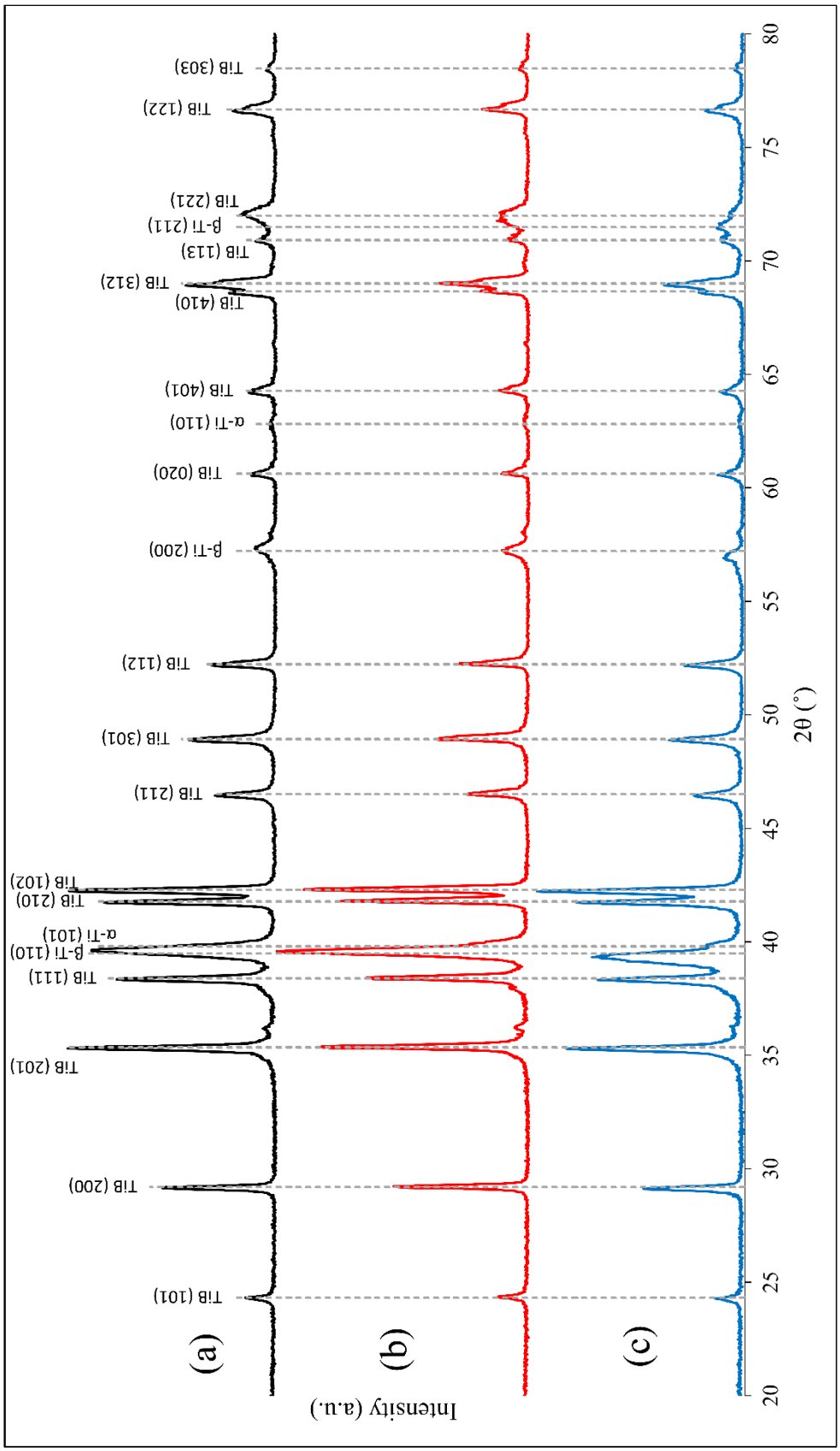


Fig. 5.3 XRD results of (a) 70 vol.% TiB, 60:40 wt.% Fe:Mo, (b) 70 vol.% TiB, 50:50 wt.% Fe:Mo, (c) 70 vol.% TiB, 40:60 wt.% Fe:Mo.

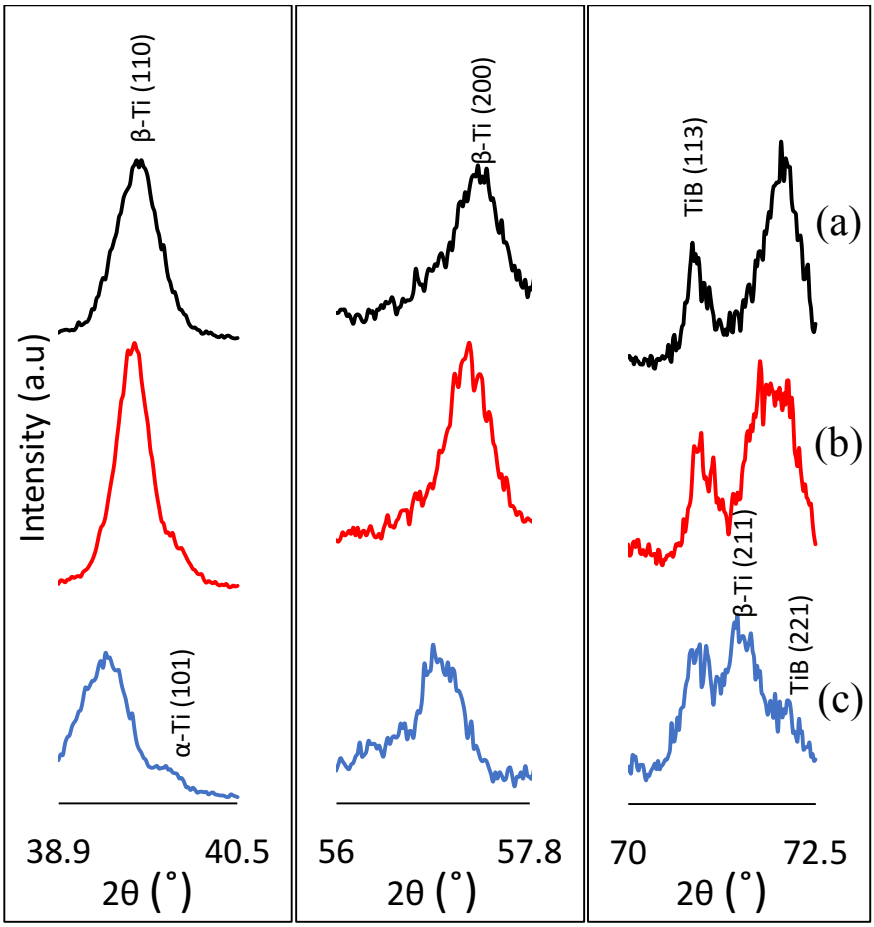


Fig. 5.4 XRD peak shifts from (a) 70 vol.% TiB, 60:40 wt.% Fe:Mo, (b) 70 vol.% TiB, 50:50 wt.% Fe:Mo, (c) 70 vol.% TiB, 40:60 wt.% Fe:Mo.

contains the desired characteristics of having beta-Ti phases heavily bridged by larger TiB whiskers. This is a designed strengthening mechanism that stems from the growth kinetics of TiB whiskers during reaction (see Figure 2.4).

### 5.2.2 Variation of TiB Volume Percent

Having decided on the best Fe:Mo ratio (40:60 by weight), TiB volume percent was varied with the end goal of comparing mechanical properties among the samples with different amounts of reinforcing TiB. Samples of 50 and 60 volume percent TiB with this ratio were synthesized for comparison with the 70 volume percent sample.

Microstructural characterization and XRD analysis were also performed on these samples to aid in comparison.

#### 5.2.2.1 Micrographs

Micrographs of the 50, 60, and 70 volume percent samples with 40:60 Fe:Mo ratio by weight were captured using optical microscopy and SEM microscopy. These samples are compared in Figure 5.5 and 5.6.

Figure 5.5 and 5.6 show, as expected, that there is a noticeable increase in the volume percent of beta-Ti phase as volume percent TiB is decreased. The pockets of beta-Ti surrounded by whiskers become noticeably larger and form visible grain boundaries in the 50 and 60 volume percent samples. Whisker size within the beta-Ti phase is generally larger as volume percent TiB is decreased. This is due to the mechanism described in Figure 2.4 that demonstrates that as Ti content is increased, there is more driving force for the reaction of $TiB_2$ growing into TiB whiskers. The lower B content also means there are fewer whiskers that impede the progress of neighboring whisker growth. Thus, it is easier for the sample to form larger TiB whiskers at the edges of the beta-Ti grains during synthesis.

As established in Section 5.2.1, the 40:60 Fe:Mo ratio (by weight) leads to an even distribution of Ti grains within the TiB clusters. This pattern can be observed in all of the samples despite the variation of TiB content.

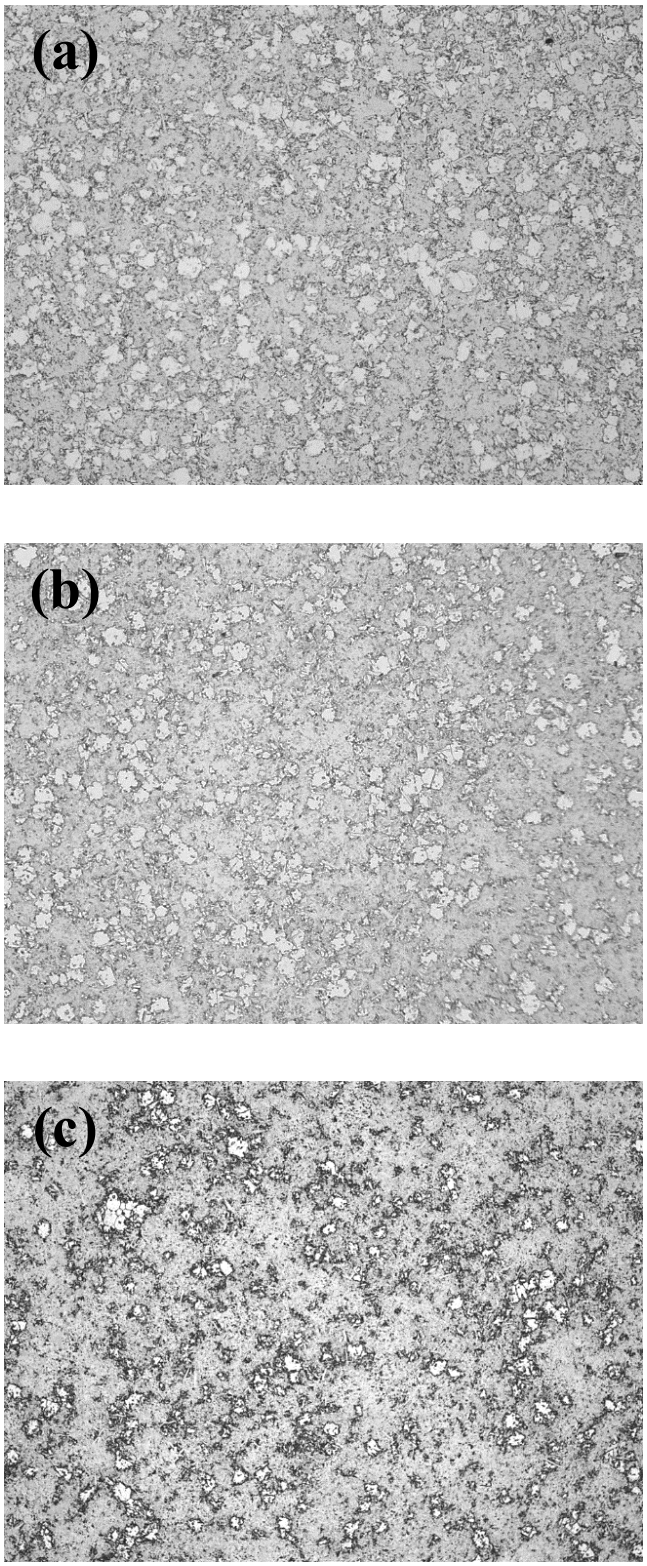


Fig. 5.5 100x Optical micrographs of Ti-B-Fe-Mo sample microstructures that have 6.4 wt.% beta-stabilizer: (a) 50 vol.% TiB, 40:60 wt.% Fe:Mo (b) 60 vol.% TiB, 40:60 wt.% Fe:Mo (c) 70 vol.% TiB, 40:60 wt.% Fe:Mo.

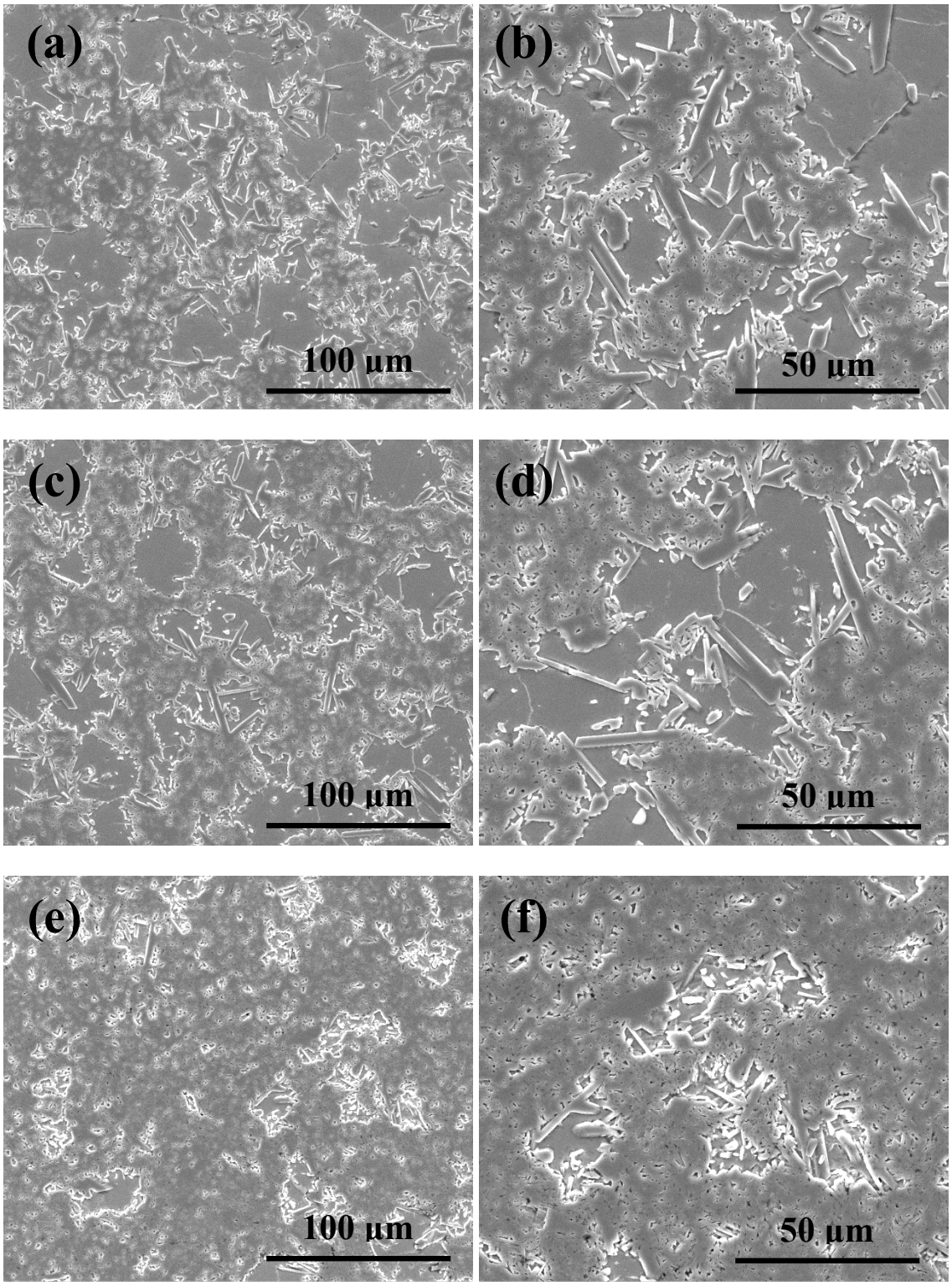


Fig. 5.6 500x and 1000x SEM micrographs of Ti-B-Fe-Mo sample microstructures that have 6.4 wt.% beta-stabilizer: (a,b) 50 vol.% TiB, 40:60 wt.% Fe:Mo (c,d) 60 vol.% TiB, 40:60 wt.% Fe:Mo (e,f) 70 vol.% TiB, 40:60 wt.% Fe:Mo.

5.2.2.2 XRD Results

Figure 5.7 shows that just as with samples from the previous section, no residual $TiB_2$ peaks remain, so the $TiB_2$ starting powders reacted completely during sintering. There is, however, a prominent alpha-Ti peak around 39º. When the sample sets are normalized among their individual data sets, it seems that the alpha-Ti peak is more prominent in the 70 volume percent sample and becomes less prominent as TiB content is reduced. Again, the formation of alpha is possibly due to a slow cooling rate. The trend of reduction in alpha-Ti peak with reducing TiB content may speak to the behavior of the beta-stabilizers during sintering. It is possible that as TiB content is highest as in the 70 volume percent sample, there is a higher driving force for Fe and Mo to be bonded with TiB to make ternary (Ti,X)B borides. As Fe and Mo go into TiB, there is less beta-stabilizer than intended remaining in the Ti grains, which reduces the stabilization of the beta-Ti phase. Figure 5.8 shows that there is a right shift in the β-Ti peaks as TiB content is increased. Thus, the lattice d-spacing of the β-Ti phase is decreasing as TiB content is increased.

## 5.3 Behavior of Fe and Mo

The XRD results of the previous section imply that there is some possibility of Fe and Mo being absorbed into the TiB phase to create (Ti,X)B ternary borides. To further analyze the behavior of these beta-stabilizers during sintering, analysis was performed using wave dispersive spectroscopy (WDS). This method was chosen because it has the ability to characterize elements of low atomic number, such as B, by utilizing the deeper penetrating x-ray radiation typical of a scanning electron

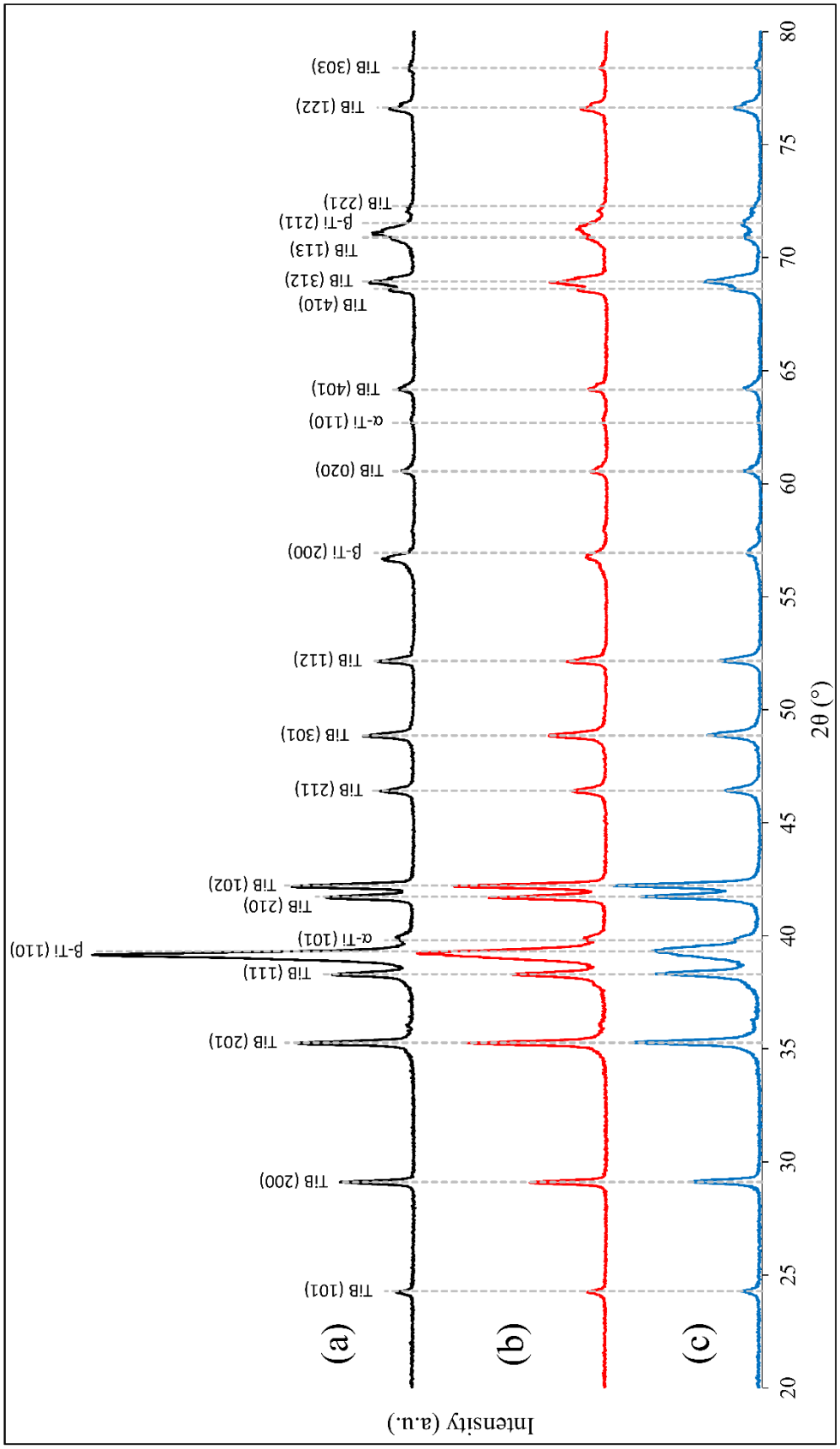


Fig. 5.7 XRD results of (a) 50 vol.% TiB, 40:60 wt.% Fe:Mo (b) 60 vol.% TiB, 40:60 wt.% Fe:Mo (c) 70 vol.% TiB, 40:60 wt.% Fe:Mo.

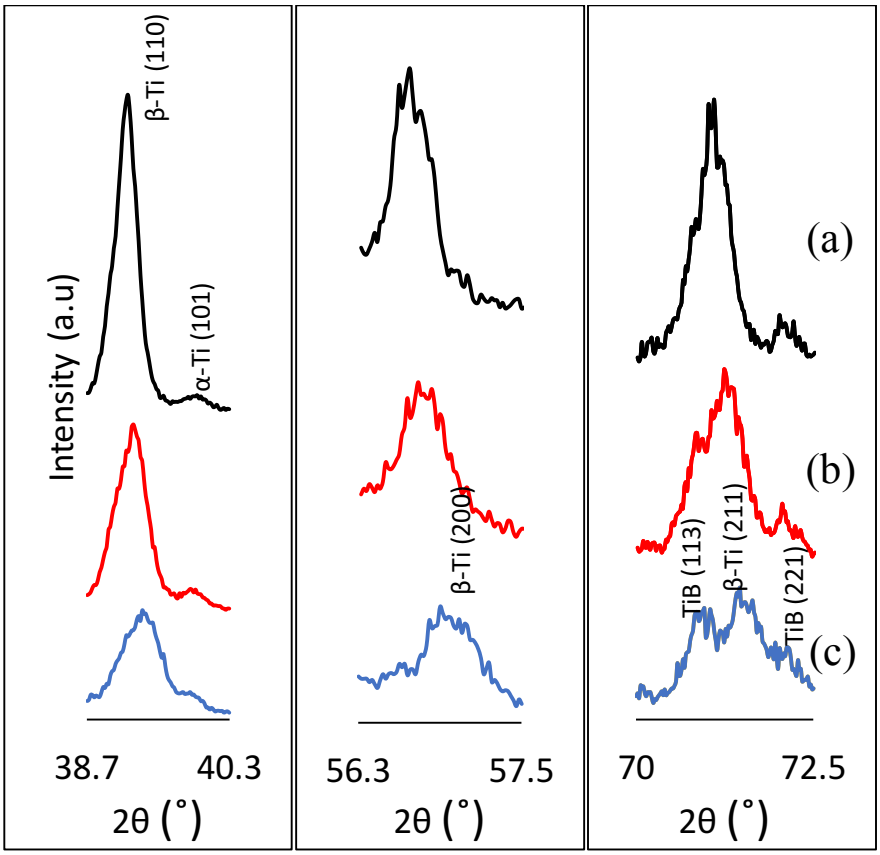


Fig. 5.8 XRD peak shifts from (a) 50 vol.% TiB, 40:60 wt.% Fe:Mo (b) 60 vol.% TiB, 40:60 wt.% Fe:Mo (c) 70 vol.% TiB, 40:60 wt.% Fe:Mo.

microscope. Energy dispersive spectroscopy (EDS) was performed on these samples, but it was unsuccessfully used to determine if Fe and Mo were being bonded in a ternary boride phase because of its limitations with B. The results of WDS analysis on the five sample combinations designed in Section 4.1 are contained in Table 5.2.

The most obvious trend shown in Table 5.2 is that Mo has almost as high of an affinity for the TiB phase as it does for the beta-Ti phase. With these results, we can safely conclude that TiBMo ternary borides or MoB borides are present in these samples. The table also shows that Fe has a very low tendency to form borides compared to Mo, and Fe is found in higher quantity in the beta-Ti phase than Mo. A note on Table 5.2: the percentage totals in each row do not add to 100% because the remaining percentage

Table 5.2 WDS results for Ti and TiB phases of each composition.

| Sample Identity | Phase | wt% element | | | |
|---|---|---|---|---|---|
| | | Ti | B | Fe | Mo |
| TiBFeMo, 70 vol.% TiB, 50:50 (wt.%) Fe:Mo | TiB Whisker | 79.1 | 17.3 | 0.7 | 3.2 |
| | β-Ti Matrix | 83.5 | 0.4 | 9.8 | 3.8 |
| TiBFeMo, 70 vol.% TiB, 40:60 (wt.%) Fe:Mo | TiB Whisker | 77.5 | 17.7 | 0.2 | 2.8 |
| | β-Ti Matrix | 83.1 | 0.1 | 8.0 | 5.4 |
| TiBFeMo, 70 vol.% TiB, 60:40 (wt.%) Fe:Mo | TiB Whisker | 79.6 | 18.4 | 1.1 | 2.6 |
| | β-Ti Matrix | 82.5 | 0.0 | 12.1 | 3.0 |
| TiBFeMo, 50 vol.% TiB, 40:60 (wt.%) Fe:Mo | TiB Whisker | 79.7 | 16.3 | 0.9 | 2.6 |
| | β-Ti Matrix | 85.7 | 0.0 | 5.9 | 5.7 |
| TiBFeMo, 60 vol.% TiB, 40:60 (wt.%) Fe:Mo | TiB Whisker | 79.8 | 18.5 | 0.4 | 3.6 |
| | β-Ti Matrix | 85.0 | 0.0 | 7.2 | 5.6 |

includes elements not specifically searched for but that are present in nominal quantity, such as O and C.

The trends highlighted in the table are further solidified by the WDS maps of the same samples. Example maps are shown in Figure 5.9. Part (a) of the figure maps the B content detected during mapping. A distinct microstructure is observable containing beta-Ti regions (black) surrounded by TiB whisker formations (white). The Fe map in part (b) is in the same location, but the same microstructure appears in almost completely opposite contrast. This is because the Fe atoms are preferentially staying within the Ti grains. Mo, conversely, is distributed through both beta-Ti and TiB phases. The majority of Mo counts still fall within the Ti grains, but there is a significant amount of Mo being registered in the boride phase. Table 5.2 and Figure 5.9 both demonstrate again that the sintering reaction went to completion. The average weight percent values of Ti and B in

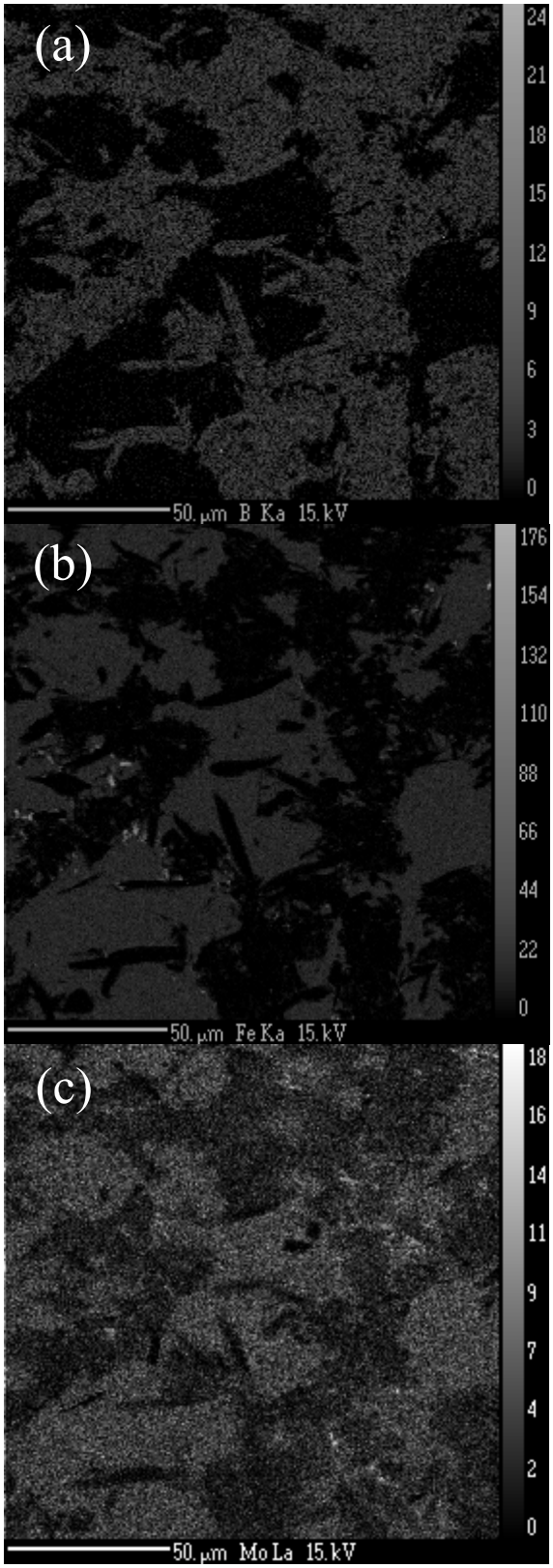


Fig. 5.9 WDS maps of a Ti-B-Fe-Mo sample. (a) map of B distribution, (b) map of Fe distribution, (c) map of Mo distribution.

the whisker phase point to a fully TiB stoichiometry.

## 5.4 Hardness

Because these composite materials have surface microstructures of both hard and soft phases and the indenter could fall on either phase or a combination of the two, at least fifteen indentations were made on each sample in order to obtain a reasonable average.

### 5.4.1 As-sintered Sample Hardness

Table 5.3 shows the sample hardness in Vickers hardness values. These are the hardness values of the samples directly after sintering. The hardness values are far below the theoretical hardness of nearly monolithic TiB in the range of 1600 kgf/mm$^2$ [5] because of the high volume percent of beta-Ti. However, it seems that the hardness does not change linearly with change in TiB volume percent. There is a jump to a higher range of hardness as samples go from 60 to 70 volume percent TiB. This may be due to a difference in microstructure, such as a change from micro- to nanoscale size of TiB whiskers.

### 5.4.2 Sample Hardness after Heat Treatment

A simple heat treatment regime for these samples was proposed in Section 2.2.4. Following this heat treatment, samples were polished and tested for changes in hardness. The results are shown in Table 5.4. The 70 volume percent sample is of similar hardness to those before heat treatment, but the 50 and 60 volume percent samples showed an

Table 5.3 Vickers hardness of samples after sintering.

| Sample Identity | Vickers Hardness ($kgf/mm^2$) |
|---|---|
| TiBFeMo, 70 vol.% TiB, 50:50 (wt.%) Fe:Mo | 1207 ± 121 |
| TiBFeMo, 70 vol.% TiB, 40:60 (wt.%) Fe:Mo | 1089 ± 163 |
| TiBFeMo, 70 vol.% TiB, 60:40 (wt.%) Fe:Mo | 1140 ± 111 |
| TiBFeMo, 60 vol.% TiB, 40:60 (wt.%) Fe:Mo | 856 ± 124 |
| TiBFeMo, 50 vol.% TiB, 40:60 (wt.%) Fe:Mo | 752 ± 80 |

Table 5.4 Vickers hardness of samples after heat treatment.

| Sample Identity | Vickers Hardness ($kgf/mm^2$) |
|---|---|
| TiBFeMo, 70 vol.% TiB, 40:60 (wt.%) Fe:Mo | 1055 ± 202 |
| TiBFeMo, 60 vol.% TiB, 40:60 (wt.%) Fe:Mo | 950 ± 135 |
| TiBFeMo, 50 vol.% TiB, 40:60 (wt.%) Fe:Mo | 836 ± 141 |

average hardness increase of about 100 kgf/mm$^2$.

However, the increases in mean hardness may not be significant when viewed with a statistical range as in Figure 5.10. The average hardness did seem to increase due to heat treatment, but the range of hardness values also enlarged with increasing standard deviation. Therefore, dubious emphasis should be placed on the increase in hardness values due to heat treatment. It can be safely concluded, however, that a 70 volume percent TiB sample can easily achieve hardness values of around 1100 kgf/mm$^2$.

## 5.5 Flexural Strength

Flexural testing was performed in accordance with the methods described in Section 4.4.2. Samples were evaluated before and after heat treatment for comparison of properties.

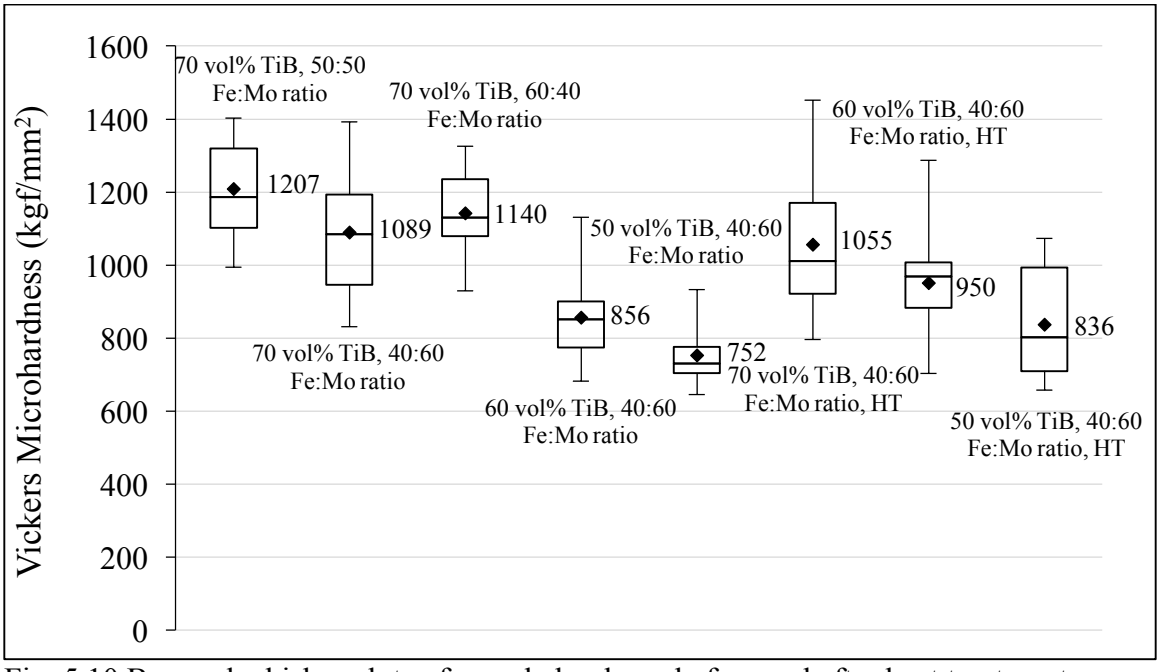


Fig. 5.10 Box and whisker plots of sample hardness before and after heat treatment. Average mean values are located to the right of each box.

### 5.5.1 As-sintered Flexural Strength

5.5.1.1 Strength Evaluation

The flexural strength was evaluated in sample sets of 10. 50, 60, and 70 volume percent TiB samples were tested. The results are contained in Table 5.5. All samples fractured in acceptable fashion according to the ASTM standard [65].

Probability of fracture and Weibull modulus calculations were performed on these sample sets. Characteristic strength of bulk material and Weibull modulus were calculated as shown in Figure 5.11.

It can be readily observed from Figure 5.11 that there is some inconsistency among the strength properties of the materials with different TiB content. The maximum flexural strength observed among all the samples was found in the 50 volume percent TiB sample (1013 MPa). It is expected that this would be the case because it has a larger fraction of metallic phase, which means it should have a higher capability for strengthening by the metal phase. However, the expected trend of increasing strength by increasing beta-Ti volume content was inconsistent beyond this point. The results show

Table 5.5 Average flexural strength of as-sintered samples.

| Sample Identity | Flexural Strength (MPa) |
|---|---|
| TiBFeMo, 70 vol.% TiB, 40:60 (wt.%) Fe:Mo | 906 ± 69 |
| TiBFeMo, 60 vol.% TiB, 40:60 (wt.%) Fe:Mo | 826 ± 84 |
| TiBFeMo, 50 vol.% TiB, 40:60 (wt.%) Fe:Mo | 941 ± 34 |

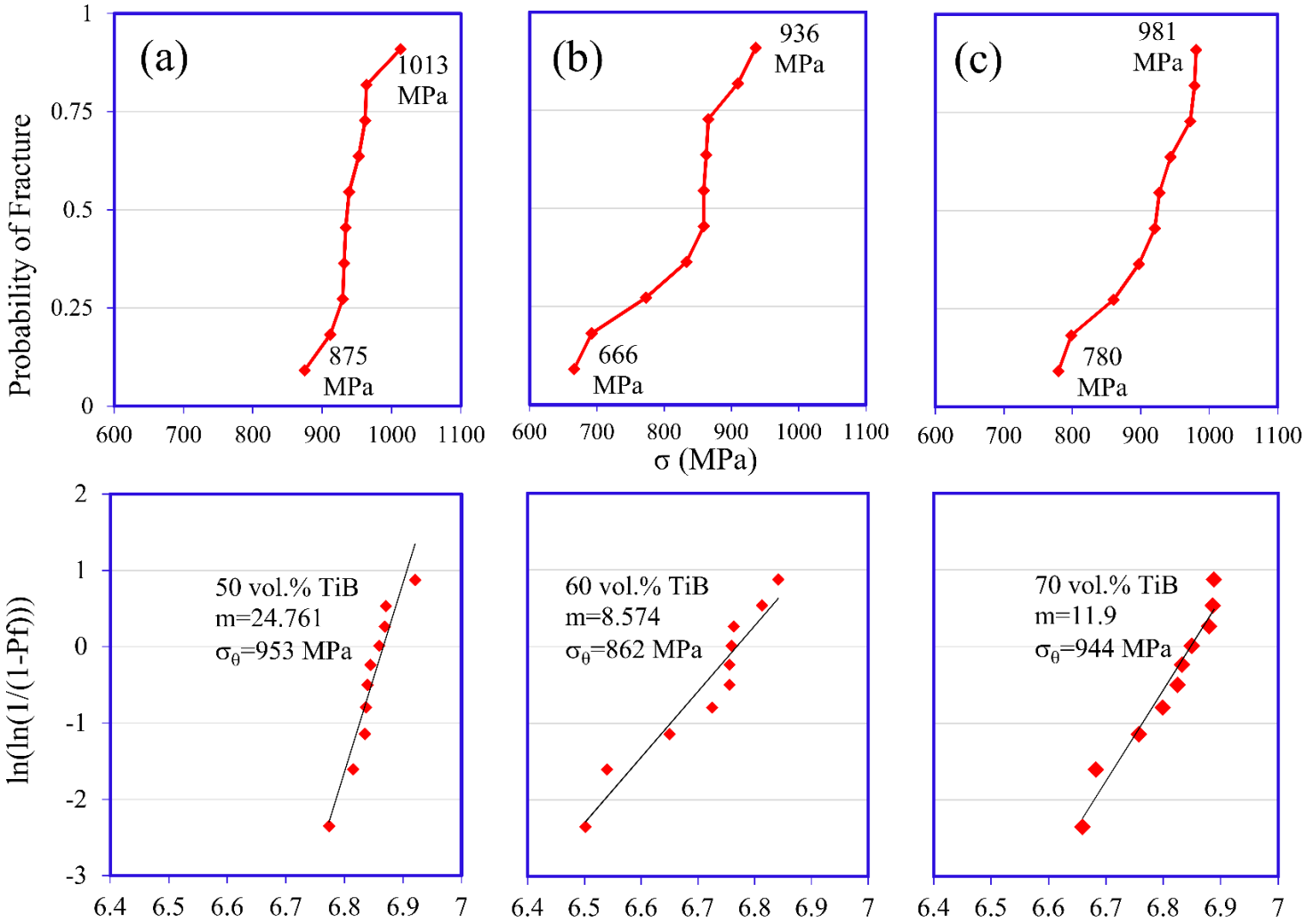


Fig. 5.11 Probability of fracture and Weibull modulus calculations for (a) 50 vol.% TiB, 40:60 wt.% Fe:Mo sample, (b). 60 vol.% TiB, 40:60 wt.% Fe:Mo sample, and (c) 70 vol.% TiB, 40:60 wt.% Fe:Mo sample.

that the 50 and 70 volume percent TiB samples had very similar strengths, while the 60 TiB volume percent samples had the lowest strength.

Consistency among sample groups, as indicated by the Weibull modulus and range between maximum and minimum strength failures, was highest with the 50 volume percent TiB samples with a Weibull modulus of 24.8. The other sample groups showed less consistent results, with larger spread between maximum and minimum strengths and lower Weibull moduli.

The 60 TiB volume percent sample was the most surprising, with a strength as low as 666 MPa, and a characteristic strength of almost 100 MPa less than the other two sample sets. In order to investigate the cause of this inconsistent behavior, fracture surfaces were analyzed. It should be noted that these measured strength values are an improvement in strength of several hundred MPa over some previous studies [7].

#### 5.5.1.2 Fracture Surface Analysis

Analysis of fracture surfaces was revealing pertaining to the inconsistent strength behavior of the sample sets. Madtha et al. [53] discovered during synthesis of Ti-TiB composites that strength properties were affected by the presence of unwanted inclusions such as Ca, O, and C. In their work, these inclusions were identified using a scanning electron microscope to be crack initiation sites.

Following the same methods, the fracture surfaces of strength specimens were characterized. Energy dispersive spectroscopy (EDS) was also used to identify which compounds were appearing at crack initiation sites. The results are shown below.

One of the inclusion types found to cause failure in test samples is shown in

Figure 5.12 and 5.13. EDS mapping shows that these particles are a compound of B and C. Because no B-C compounds were intended in powder mixtures, it is speculated that these particles remain from powder manufacturing processes of the $TiB_2$ powders. These particles were found to be the points of crack origin because of the round fracture pattern seen extending in all directions from these particles. These particles were not very common in the samples and were located randomly through the bulk of the sample. They caused failure when they were located near the tensile surface of the sample during bending.

The far more common inclusion causing failure was found to contain Ca-O compounds, as shown in Figure 5.14 and 5.15. These brittle particles always appeared ruptured with large cracks, indicating their easy failure under bending stresses. The same 360 degree fracture pattern extends from these particles as the B-C particles from Figure 5.12. These Ca-O particles were found at all depths through the samples. In fact, one Ca-O particle caused failure about 200 μm from the tensile surface of the sample. This distribution through the bulk of the sample implies that these inclusion particles were added to the material as part of the original metal powders, as opposed to diffusion from the surface of the sample, for example. ICP analysis showed the presence of Ca in the Puris Ti powders in low but significant amounts (0.13 weight percent).

Both types of inclusion particles varied in size and distance from the tensile surface of the sample. The size, distance from tensile surface, and type of inclusion all played a role in altering the fracture strength of the materials. Table 5.6 shows these factors causing failure, as far as could be determined using SEM and EDS techniques.

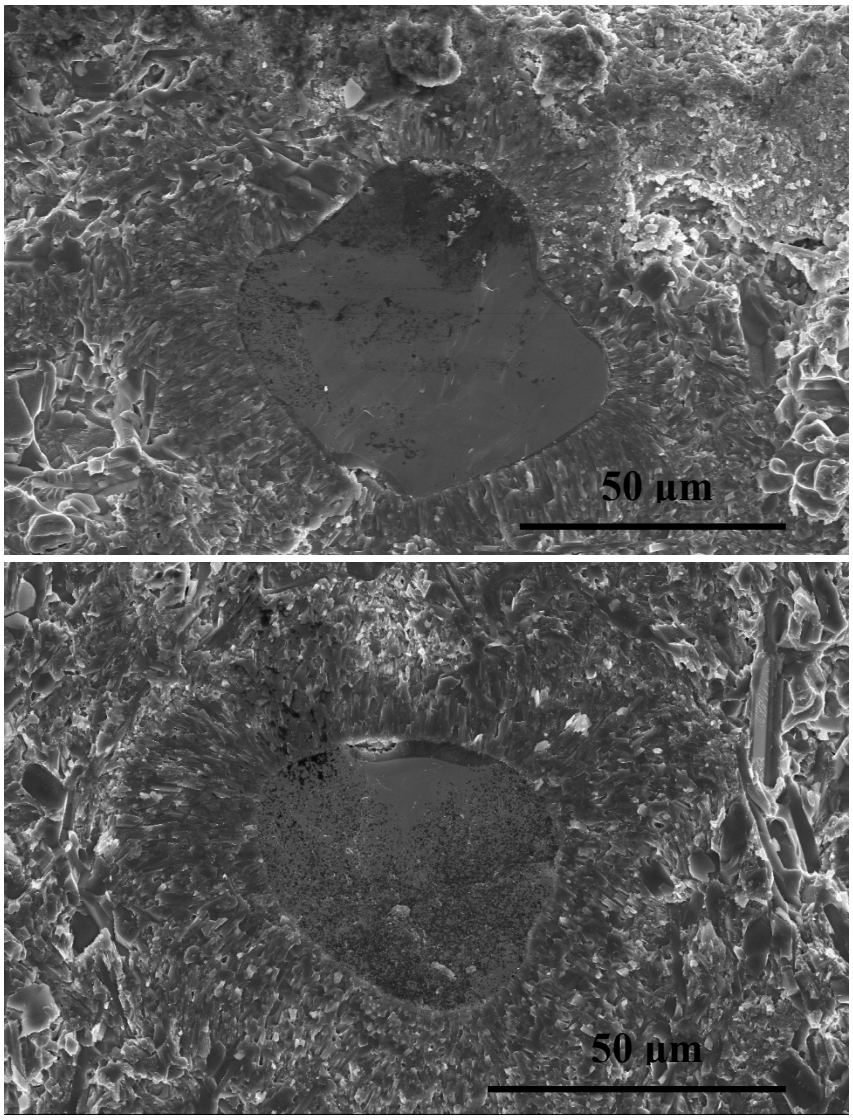


Fig. 5.12 SEM micrographs of B-C inclusions causing fracture in flexural strength specimens.

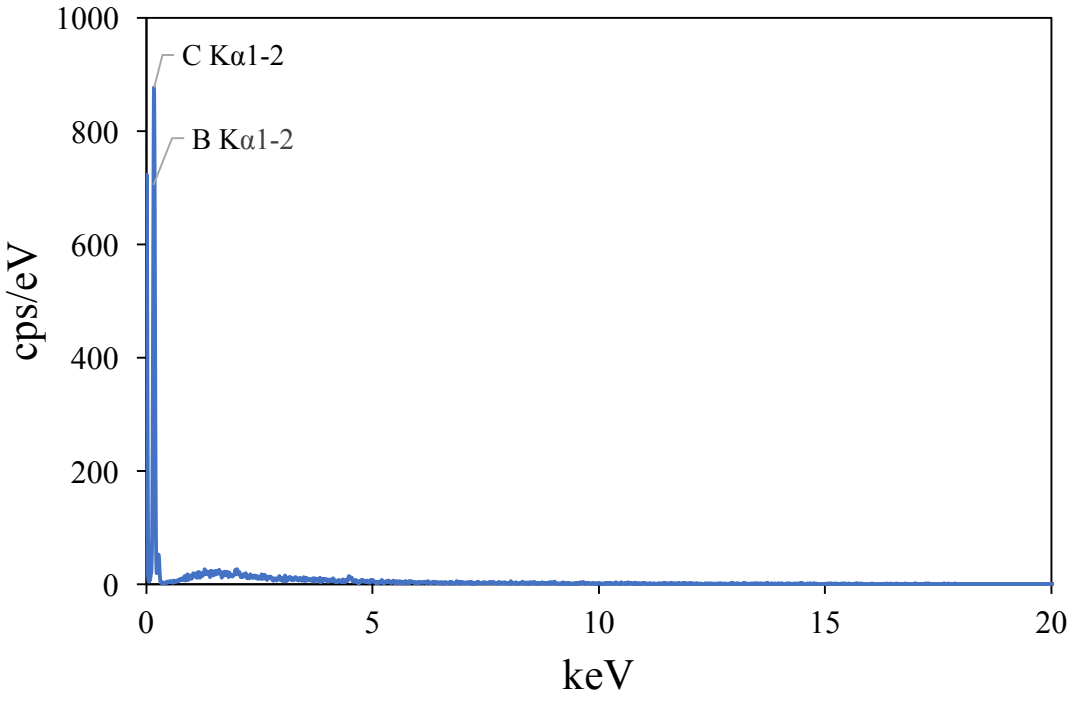


Fig. 5.13 EDS plot depicting B and C content of failure-causing inclusions in strength test bars.

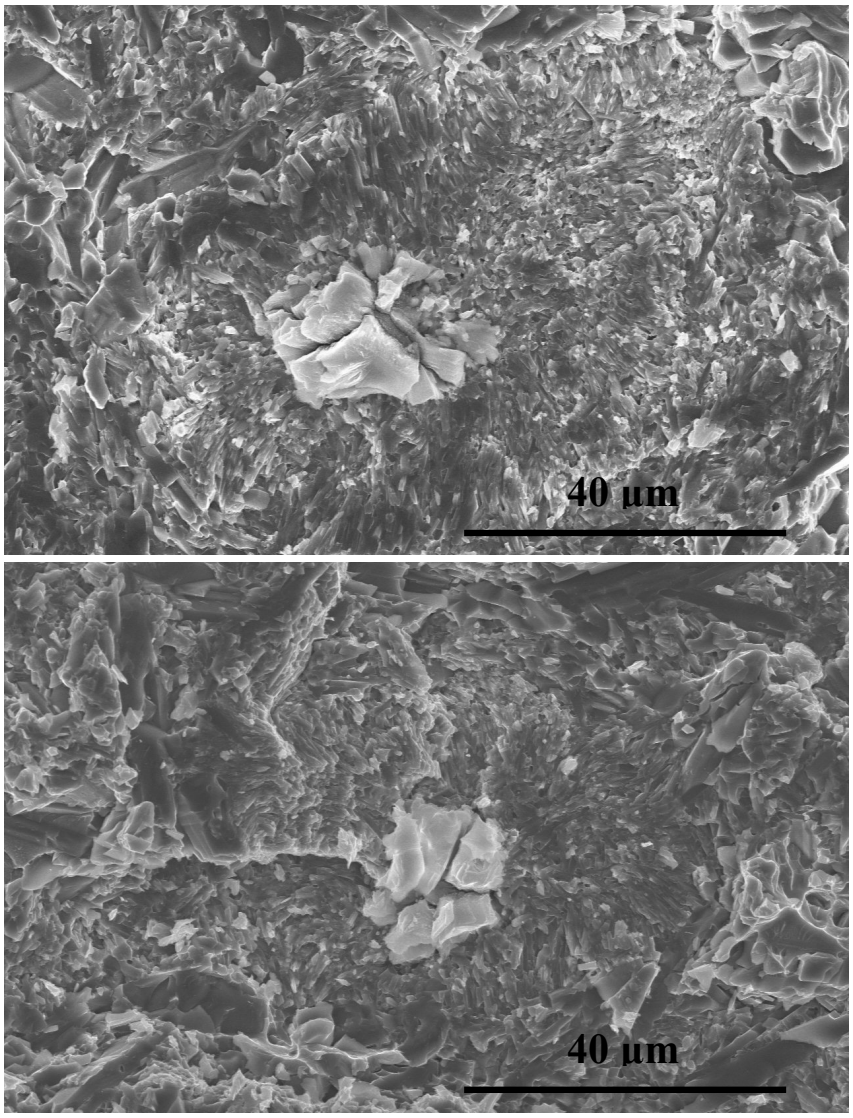


Fig. 5.14 SEM micrographs of Ca-O inclusions causing fracture in flexural strength specimens.

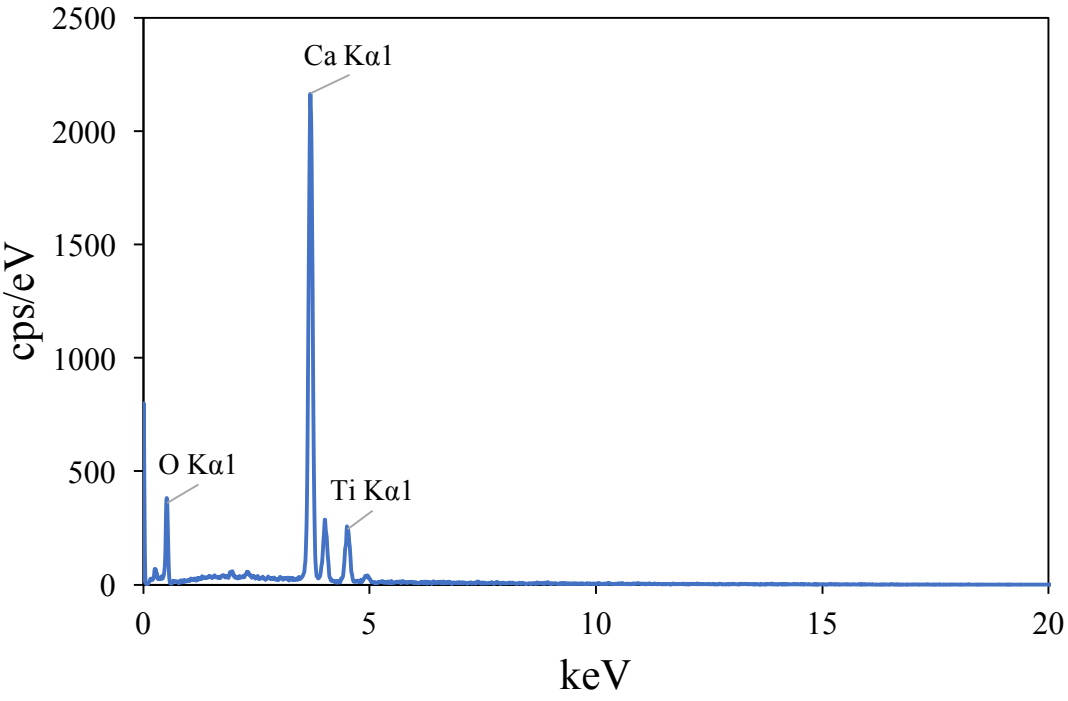


Fig. 5.15 EDS plot depicting Ca and O content of failure-causing inclusions in strength test bars.

Table 5.6 Type of inclusion causing failure for each sample set.

| Composition | Arbitrary Test Number | Failure Strength (MPa) | Ave. Particle diameter (μm) | Particle Distance From Tensile Surface (μm) | Particle Composition |
|---|---|---|---|---|---|
| TiBFeMo, 50 vol.% TiB, 40:60 (wt.%) Fe:Mo | 1 | 875 | 67 | 42 | B, C |
| | 2 | 911 | 38 | 18 | Ca, O, C |
| | 3 | 932 | 27 | 82 | Ca, O |
| | 4 | 953 | 48 | 160 | B, C, Ca |
| | 5 | 962 | 25 | 78 | Ca, O, C |
| | 6 | 964 | 17 | 200 | Ca, O |
| | 7 | 1013 | 23 | 18 | Fe, Ti |
| TiBFeMo, 60 vol.% TiB, 40:60 (wt.%) Fe:Mo | 1 | 666 | 90 | 0 | B, C, Ca, O |
| | 2 | 692 | 89 | 0 | B, C, O |
| | 3 | 773 | 42 | 5 | Ti, C |
| | 4 | 833 | 26 | 7 | Ca, O |
| | 5 | 862 | 44 | 61 | B, O, C, Ca |
| | 6 | 865 | 28 | 89 | Ca, O |
| | 7 | 910 | 40 | 172 | Ca, O |
| | 8 | 936 | 28 | 100 | Ca, O |
| TiBFeMo, 70 vol.% TiB, 40:60 (wt.%) Fe:Mo | 1 | 799 | 27 | 0 | Ti, B, Ca, O |
| | 2 | 861 | 14 | 0 | Ti, O |
| | 3 | 897 | 49 | 112 | Ca, O |
| | 4 | 921 | 16 | 31 | Ca, O |
| | 5 | 944 | 31 | 45 | Ca, O |
| | 6 | 972 | 10 | 35 | Ca, O, C |
| | 7 | 979 | 29 | 54 | Ca, O |
| | 8 | 981 | 16.5 | 31 | Ca, O |

### 5.5.2 Flexural Strength after Heat Treatment

After heat treatment of samples, according to the regime proposed in Section 2.2.4, test bars were prepared for strength testing by the same grinding methods as before. A surface oxide layer formed during heat treatment needed to be removed in addition to the Cu-containing layer deposited by EDM machining.

#### 5.5.2.1 Strength Evaluation

Sample sets were smaller than those tested before heat treatment, which excluded the possibility of valid Weibull modulus calculations. However, average flexural strength of the differing compositions is shown in Table 5.7.

Table 5.7 reflects something of the trend in change in strength expected from changing the volume percent of TiB, which was not easily observed before heat treatment. According to these samples after heat treatment, increasing the volume percent of TiB by 10% causes a reduction in flexural strength of about 250 MPa.

This consistency in behavior may imply that the inclusions that caused such inconsistent behavior before heat treatment may not be playing as large of a role after heat treatment.

#### 5.5.2.2 Fracture Surface Analysis

Fracture surfaces of the heat-treated flexural strength samples were analyzed using the same SEM and EDS techniques. Typical results are shown below.

Figure 5.16 shows a sample that had crack initiation near the tensile surface which originated from the bulk material. The sample came from the 70 volume percent sample

Table 5.7 Average flexural strength of samples after heat treatment.

| Sample Identity (Post Heat Treatment) | Flexural Strength (MPa) |
|---|---|
| TiBFeMo, 70 vol.% TiB, 40:60 (wt.%) Fe:Mo | 375 ± 29 |
| TiBFeMo, 60 vol.% TiB, 40:60 (wt.%) Fe:Mo | 612 ± 73 |
| TiBFeMo, 50 vol.% TiB, 40:60 (wt.%) Fe:Mo | 871 ± 39 |

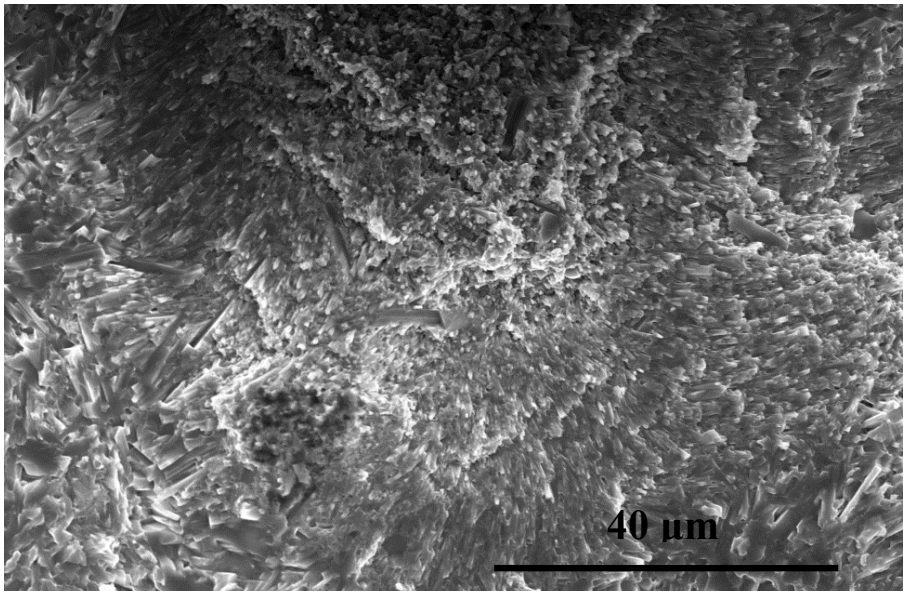


Fig. 5.16 Point of crack initiation in the bulk material of a flexural test sample after heat treatment.

set which had low flexural strength around 375 MPa. It was clear that this was the point of crack initiation due to the directional cracking patterns radiating out from the central point. It was also apparent that no obvious inclusion particle was the cause of this fracture at low strength. It must be concluded, then, that strengthening of the materials by their bulk properties was altered during heat treatment.

The strongest factor affecting strength in these materials after heat treatment seems to originate from bulk properties of the material, and determination of flexural strength is not dictated exclusively by inclusion particles, as was the case before heat treatment. However, the presence of inclusion particles is not nonexistent, as exhibited in Figure 5.17. In this sample and a few others among the sample sets, an inclusion containing a primarily Ca-O compound was again found to be the site of crack initiation.

### 5.6 Fracture Toughness

Fracture toughness of samples of varying TiB volume percent was determined according the methods described in Section 4.4.3. Just as with flexural strength analysis,

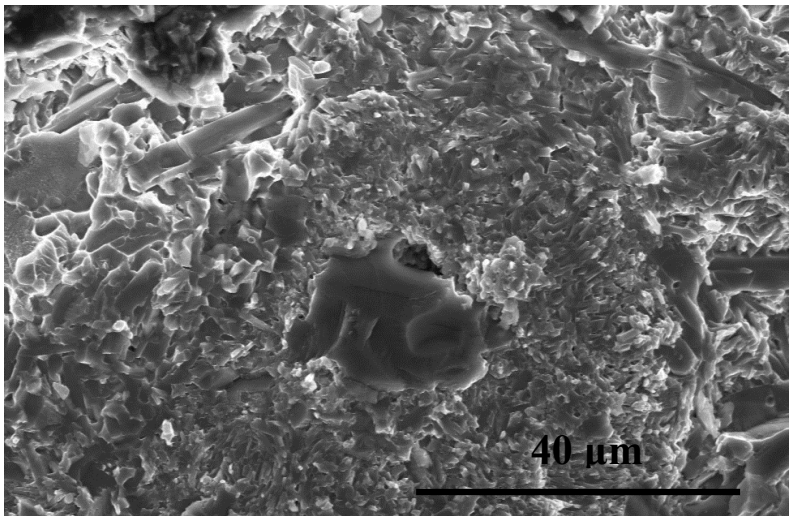


Fig. 5.17 Ca-O inclusion causing failure in a flexural test sample after heat treatment.

samples were evaluated before and after heat treatment for comparison of properties.

### 5.6.1 As-sintered Fracture Toughness

5.6.1.1 Fracture Toughness Evaluation

The fracture toughness was evaluated in sample sets of six. 50, 60, and 70 volume percent TiB samples were tested. The results are contained in Table 5.8. All samples fractured in acceptable fashion according to the ASTM standard [66].

The pattern created by these fracture toughness tests is that toughness of samples increases as the volume fraction of beta-Ti is increased. This was the expected result, as fracture toughness is a measure of energy absorption during crack propagation and a larger amount of ductile phase provides more ability for the material to absorb energy. However, the trend is not linear. The fracture toughness increases by 5 MPa√m between 70 and 60 volume percent TiB, but only 2 MPa√m between 60 and 50 volume percent TiB. In these cermets, incremental increases in metal content seem to have larger effects on toughness when the material has a higher ceramic content.

Table 5.8 Average fracture toughness of as-sintered samples.

| Sample Identity | Fracture Toughness (MPa√m) | Vickers Hardness ($kgf/mm^2$) |
|---|---|---|
| TiBFeMo, 70 vol.% TiB, 40:60 (wt.%) Fe:Mo | 10.5 ± 0.2 | 1089 ± 163 |
| TiBFeMo, 60 vol.% TiB, 40:60 (wt.%) Fe:Mo | 15.4 ± 0.5 | 856 ± 124 |
| TiBFeMo, 50 vol.% TiB, 40:60 (wt.%) Fe:Mo | 17.8 ± 0.8 | 752 ± 80 |

5.6.1.2 Fracture Surface Analysis

Analysis of fracture behavior during toughness testing was performed by fracture surface analysis with a scanning electron microscope. Crack propagation through both TiB and beta-Ti phases was characterized.

Figure 5.18 highlights the behavior of the 70 volume percent sample. Clusters of TiB bound by beta-Ti bridged the gap that the crack was extending through, bonding strength between beta-Ti and TiB resisted pullout of TiB whiskers from the beta-Ti grains during crack propagation, and the beta-Ti phase forced crack propagation through various planes. All these behaviors contributed to resistance to crack growth and increased toughness measurements.

In Figure 5.19, the 60 volume percent TiB samples showed similar characteristics to the 70 volume percent TiB samples. There were TiB clusters bound by beta-Ti protruding from the fracture surface as bridging mechanisms during fracture. The TiB whiskers around these protrusions seem to absorb large amounts of energy and exhibited cracking. TiB whisker pullout from the beta-Ti phase seemed to be a little different from the 70 volume percent samples because the pullout surfaces showed little deformation. This might indicate that the bonding between TiB whiskers and beta-Ti was not quite as strong.

The 50 volume percent TiB samples showed similar whisker pullout properties to the 60 volume percent TiB samples. There was little deformation in the beta-Ti grains from whisker pullout, indicating that debonding did not consume as much energy as the 70 volume percent TiB samples. Because of the presence of a larger amount of ductile metal phase, it appeared in these samples that most of the cracking occurred within the

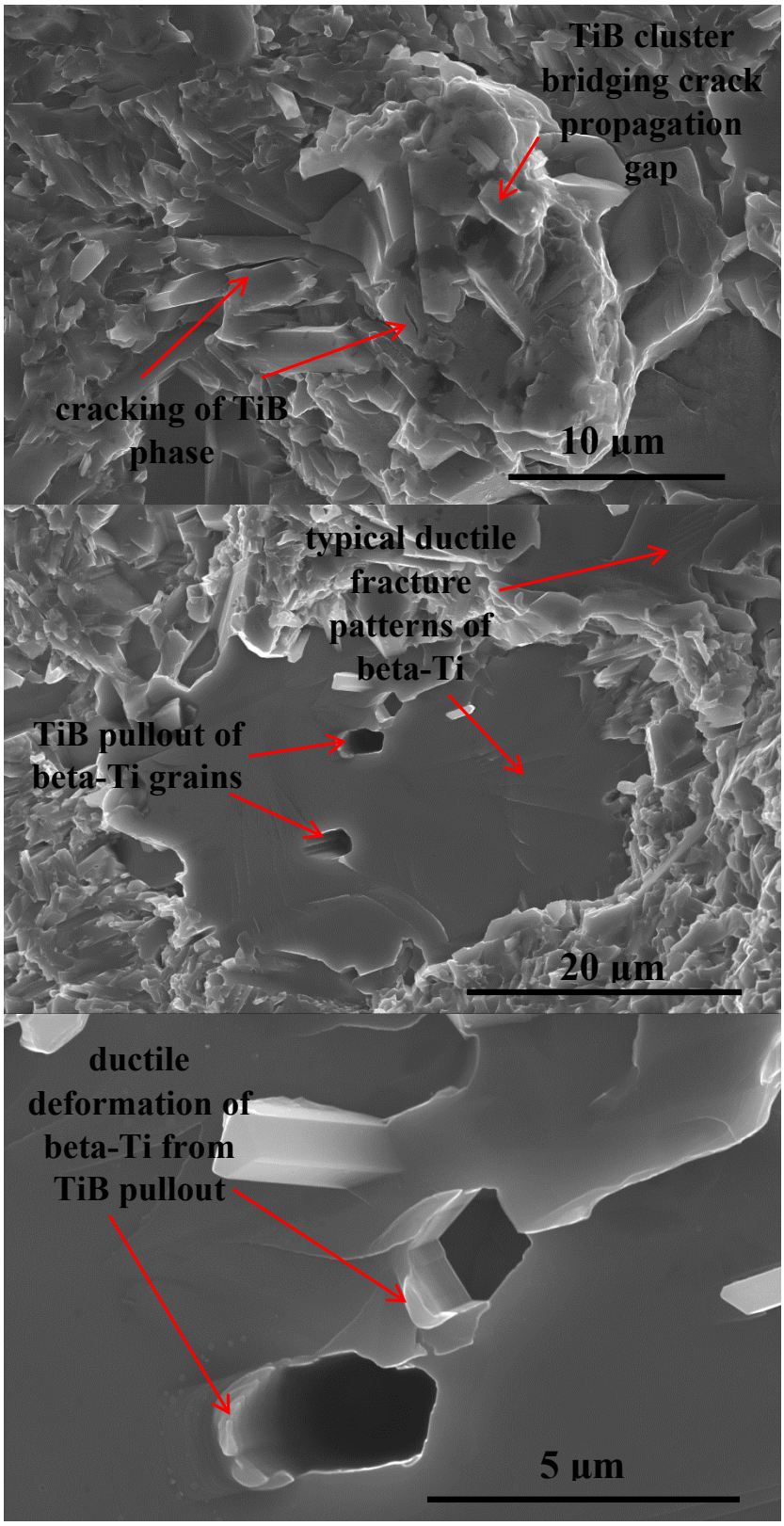


Fig. 5.18 Fracture toughness surface analysis of 70 vol.% TiB, 40:60 wt.% Fe:Mo sample tested as-sintered.

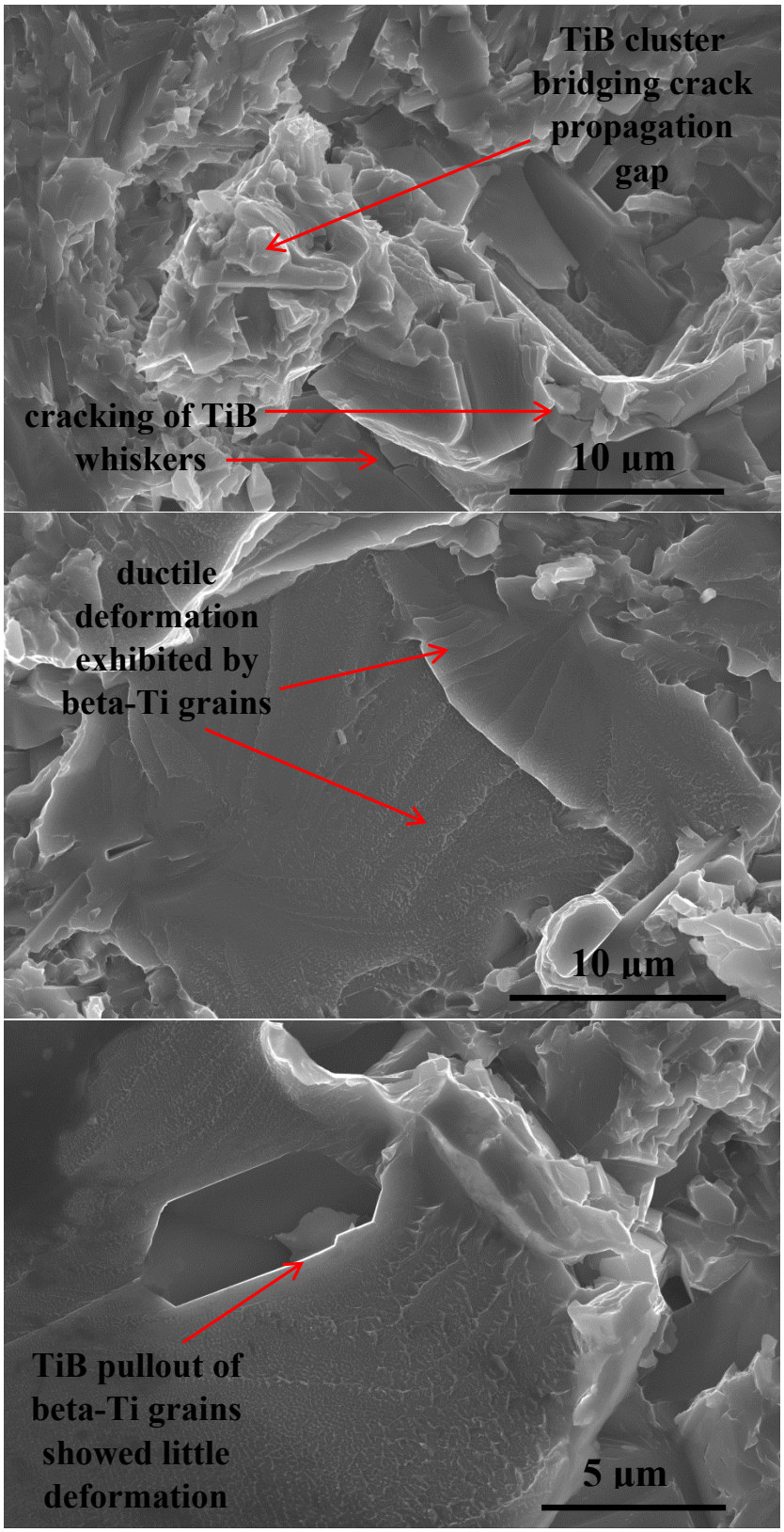


Fig. 5.19 Fracture toughness surface analysis of 60 vol.% TiB, 40:60 wt.% Fe:Mo sample tested as-sintered.

TiB whiskers. Clusters of nanoscale TiB whiskers developed large fissures as the crack propagated through the bar. There is more evidence of large TiB whiskers embedded in and strengthening the beta-Ti phase compared to the other compositions. This is primarily due to the different formation of morphology, as discussed in Section 2.2.2. The SEM analysis of 50 volume percent TiB samples confirms the increase in toughening by increase of ductile metal phase. These points can be observed in Figure 5.20.

### 5.6.2 Fracture Toughness after Heat Treatment

The samples with 50, 60, and 70 volume percent TiB were heat treated according to Section 2.2.4 and prepared for testing in the same fashion as samples in Section 5.6.1.

#### 5.6.2.1 Fracture Toughness Evaluation

Average fracture toughness values after heat treatment are recorded in Table 5.9. They demonstrate an increase in toughness between 6 and 9% among the different compositions due to heat treatment.

The heat treatment was supposed to reduce the formation of unwanted phases that might deteriorate mechanical properties. The heat treatment succeeded at increasing the toughness of the samples, but at the expense of flexural strength. The first step in investigating the causes of this behavior was fracture surface analysis after toughness testing.

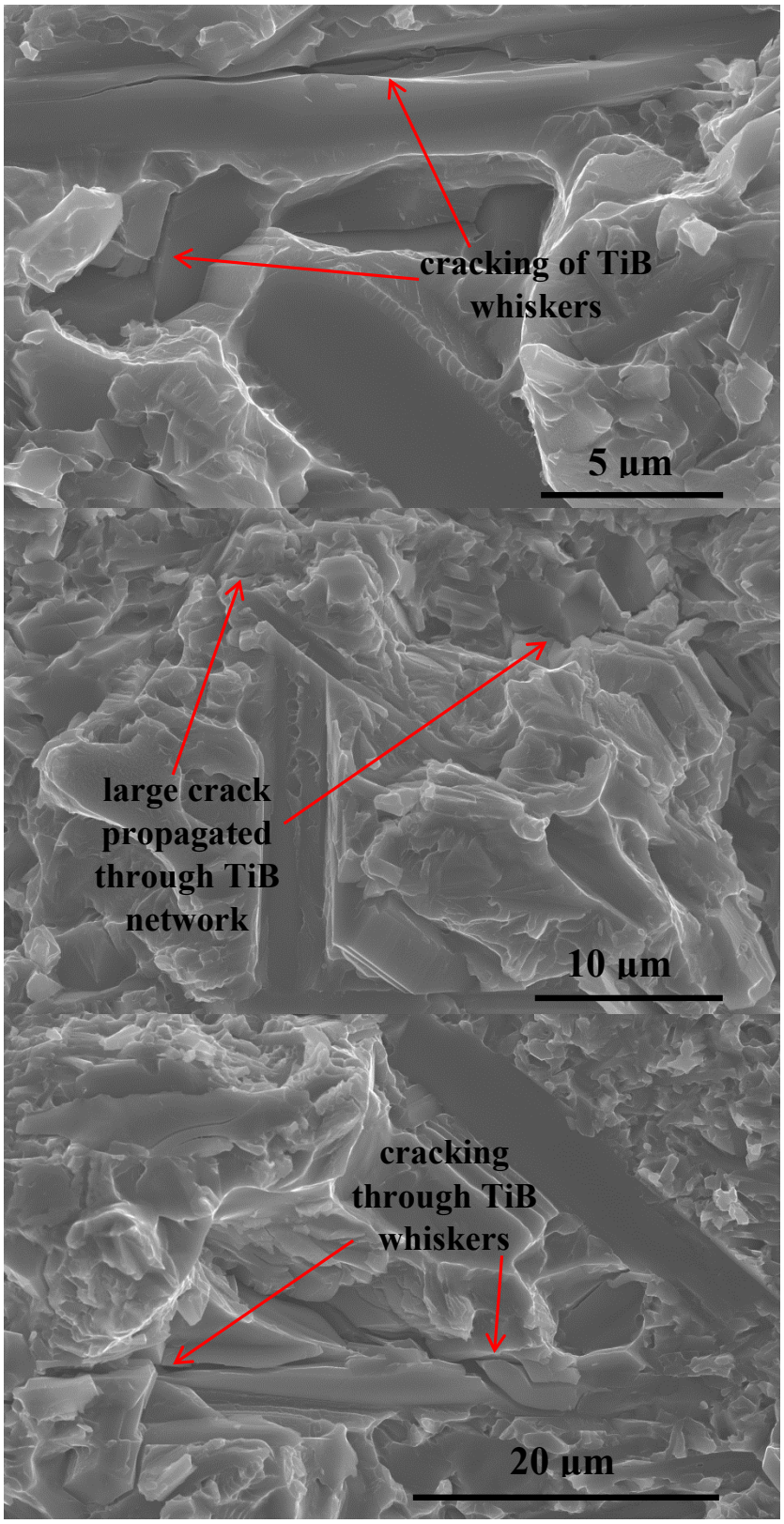


Fig. 5.20 Fracture toughness surface analysis of 50 vol.% TiB, 40:60 wt.% Fe:Mo sample tested as-sintered.

Table 5.9 Average fracture toughness of samples after heat treatment.

| Sample Identity (Post Heat Treatment) | Fracture Toughness (MPa√m) | Vickers Hardness ($kgf/mm^2$) |
|---|---|---|
| TiBFeMo, 70 vol.% TiB, 40:60 (wt.%) Fe:Mo | 11.4 ± 0.3 | 1055 ± 202 |
| TiBFeMo, 60 vol.% TiB, 40:60 (wt.%) Fe:Mo | 16.3 ± 0.6 | 950 ± 135 |
| TiBFeMo, 50 vol.% TiB, 40:60 (wt.%) Fe:Mo | 19.4 ± 0.5 | 836 ± 141 |

5.6.2.2 Fracture Surface Analysis

The fracture surface analysis of heat treated toughness samples is shown in Figure 5.21, 5.22, and 5.23. In general, the beta-Ti appeared to have a slightly higher stiffness than before heat treatment, while still exhibiting some ductile behavior.

The largest observable difference in the samples after heat treatment is the different behavior of the beta-Ti phase. After fracture, the beta-Ti grains appeared as elevated islands standing out from the rest of the surface. At the edge of these islands were sharp cleavage fractures. The fracture patterns through the beta-Ti traveled in straighter lines than before heat treatment. Deformation from pullout of TiB whiskers was less ductile than before heat treatment. All of these indications point to a stiffer behavior of the beta-Ti phase.

The most likely cause of this change in behavior is the heat treatment regime. The samples were water-quenched from 1273 K to room temperature in fractions of a second. This rapid rate of cooling would lead to dimensional contraction of the bars and development of internal stresses and possible metastable athermal omega phase with a

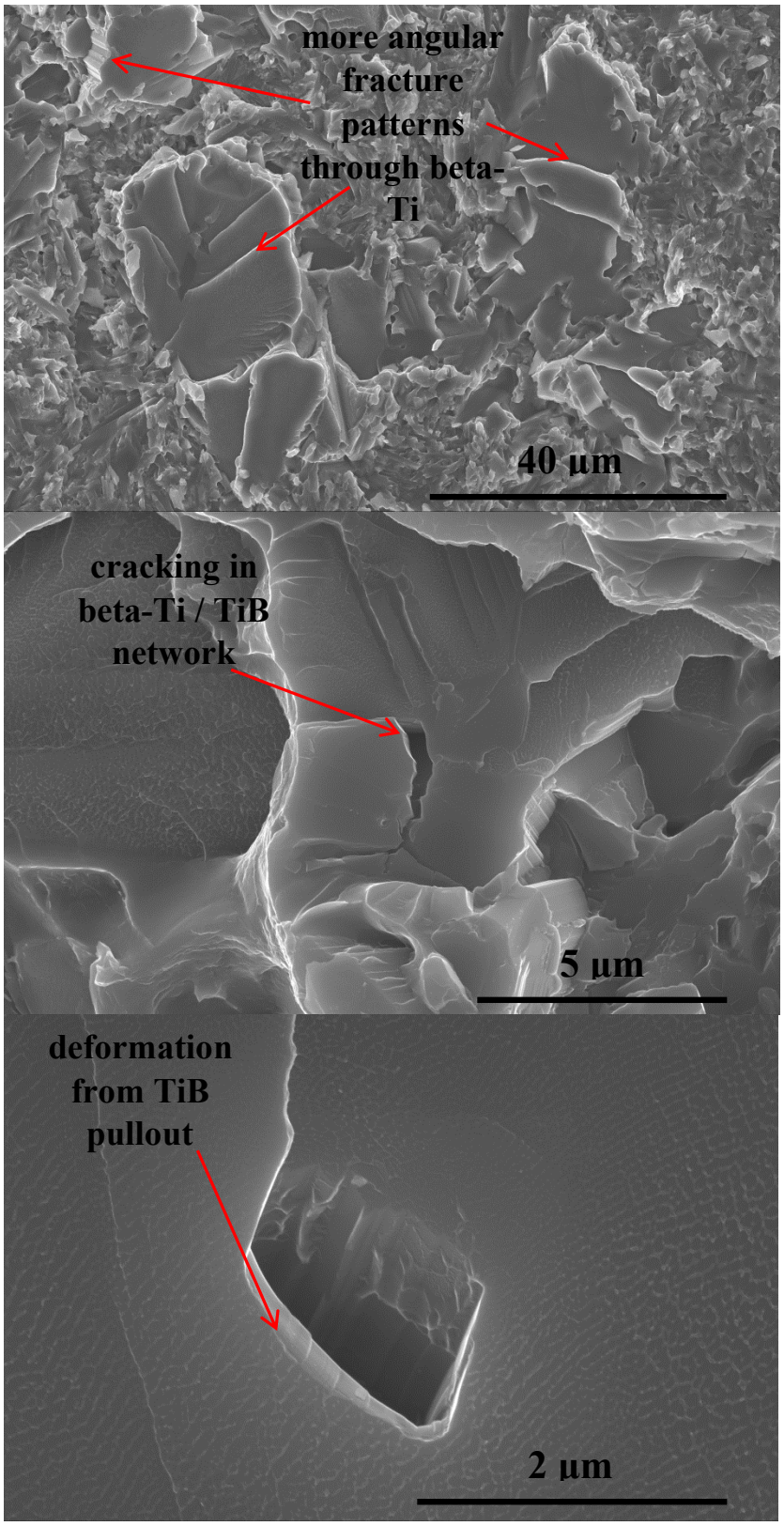


Fig. 5.21 Fracture toughness surface analysis of 70 vol.% TiB, 40:60 wt.% Fe:Mo sample tested after heat treatment.

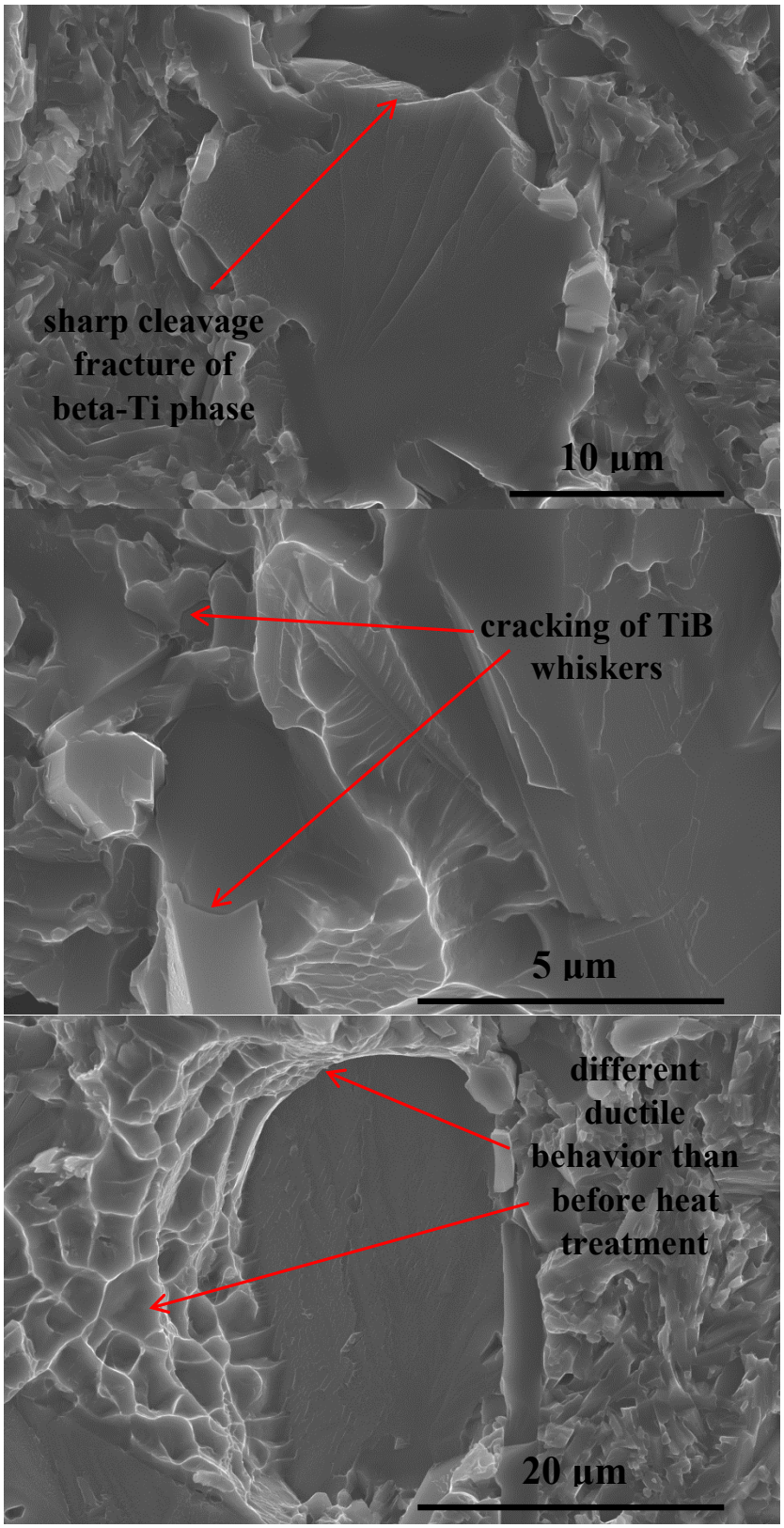


Fig. 5.22 Fracture toughness surface analysis of 60 vol.% TiB, 40:60 wt.% Fe:Mo sample tested after heat treatment.

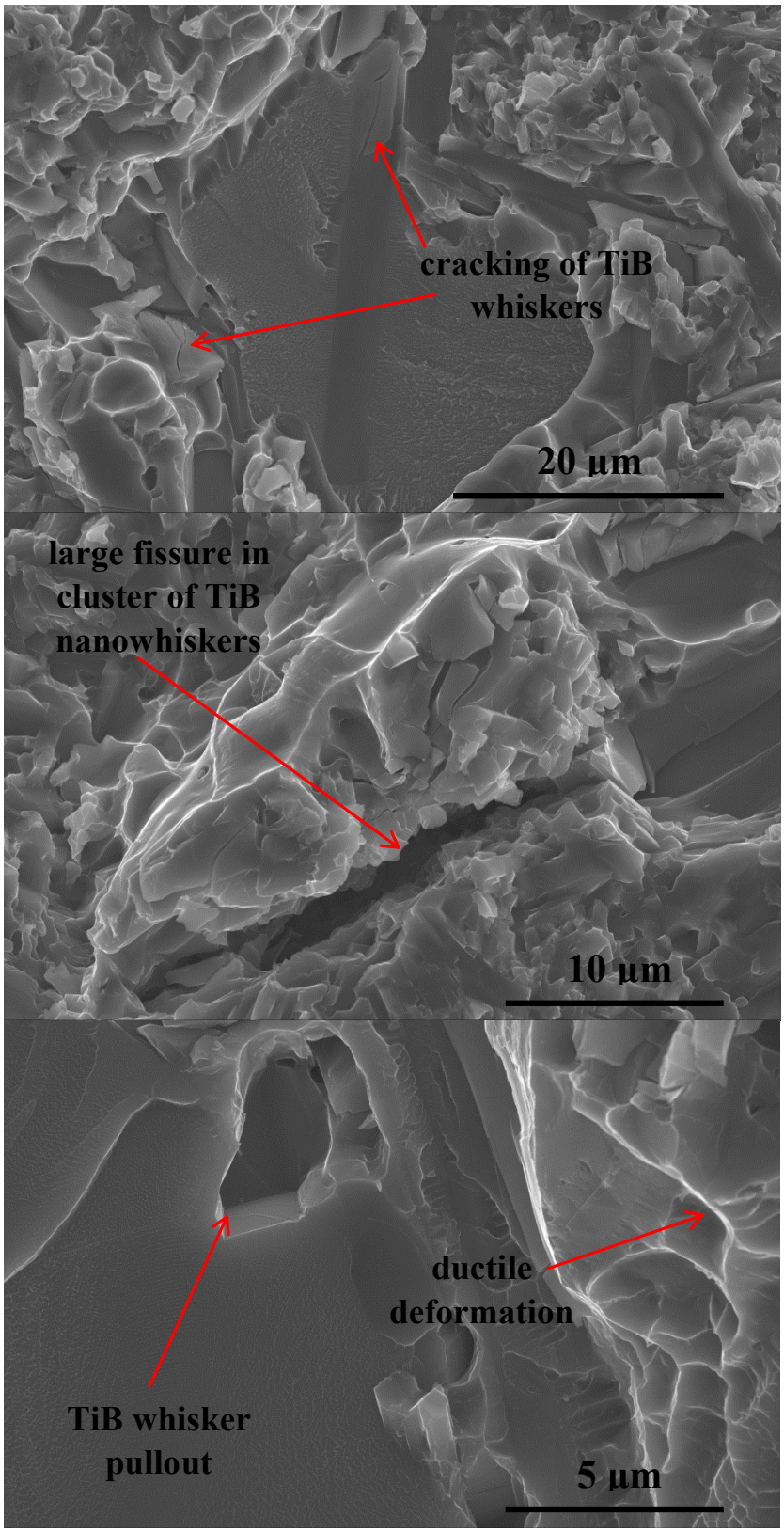


Fig. 5.23 Fracture toughness surface analysis of 50 vol.% TiB, 40:60 wt.% Fe:Mo sample tested after heat treatment.

hexagonal crystal structure [67]. Introducing these changes into the beta-Ti phase would account for its increase in stiffness as seemed to be apparent in the micrographs. This would also help explain the fracture toughness increase. A metallic phase with dual hexagonal and bcc structures would help prevent the propagation of cracks by forcing cracks to move through many alternating structures, thereby impeding their progress. However, the decrease in flexural strength by the same changes is concerning. While toughness increased, the reduction in strength was dramatic in some samples. If athermal omega phase was formed (which further analysis beyond the scope of this thesis will determine), then a non-close-packed hexagonal phase among the beta-Ti structures would be detrimental to strength properties. The change in strength and toughness properties before and after heat treatment is depicted in Figure 5.24.

It is possible that an annealing or ageing step could be added to the heat treatment regime to improve strength properties, but this would have to be investigated carefully, because ageing could introduce isothermal omega phase into the metal grains, which could defeat the purpose of the initial heat treatment.

## 5.7 Cermet property comparison

This section contains a brief comparison of mechanical properties of some common cermets and the Ti-TiB cermets discussed in this project. The comparison is by no means exhaustive, but offers some context to the value of the materials synthesized in this project based on their mechanical properties. The comparison is shown in Table 5.10.

In comparison to some former work with Ti-TiB composites, the samples tested in this project showed similar hardness, but an improvement in flexural strength and

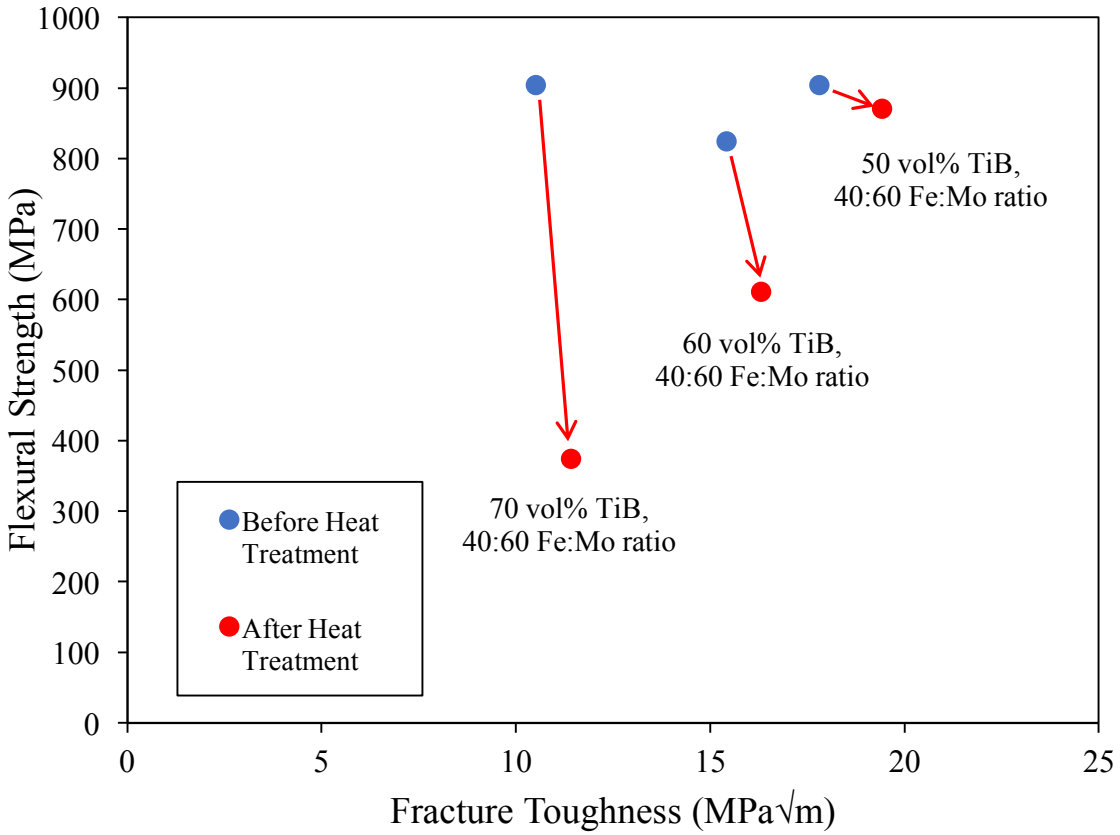


Fig. 5.24 Comparison of strength and toughness of samples before and after heat treatment.

Table 5.10 Comparison of some common industry cermets with Ti-TiB cermets.

| Cermet Composition | Volume Fraction Ceramic Phase | Hardness ($kgf/mm^2$) | Flexural Strength (MPa) | Fracture Toughness (MPa√m) | Reference |
|---|---|---|---|---|---|
| TiB-Ti | 0.4 | 772 | 193 | 6.1 | [7] |
| TiB-Ti | 0.5 | 800* | 449 | 6.2* | [7] |
| WC-Co | 0.8 | 1950 | - | 8 | [19] |
| TiC-TiN-WC-Co | 0.8 | 1475 | - | 16.5 | [24] |
| Ti(C,N)-(Mo,Ni,Co) | 0.9 | 1900 | 1200 | 6 | [26] |
| $TiB_2$-W | 0.7 | 2500 | 700 | 8 | [39] |
| TiB-Ti | 0.5 | 752 | 941 | 17.8 | Experimental |
| TiB-Ti | 0.6 | 856 | 826 | 15.4 | Experimental |
| TiB-Ti | 0.7 | 1090 | 906 | 10.5 | Experimental |

*extrapolated from trends in reported data

fracture toughness. This is due to the stabilization of the beta-Ti phase, which improves bulk properties over composites with alpha-Ti. When compared to other types of cermets, the most noticeable advantage of Ti-TiB cermets is high fracture toughness. The samples in this project achieved high relative toughness while still maintaining competitive flexural strength and hardness. This balance of properties makes Ti-TiB cermets with stabilized beta-Ti phase attractive candidates for current applications of cermets.

# CHAPTER 6

# CONCLUSIONS

## 6.1 Research Objectives

One of the primary objectives of this research, to successfully synthesize Ti-TiB materials in the cermet range using powder metallurgy techniques, was accomplished. All the samples analyzed in this study were fully dense and free of pores. The density was confirmed by analysis of fracture surfaces that showed that crack initiation in samples started from sites other than pores.

Electric-field-activated sintering was successfully utilized for this synthesis at a relatively low operating temperature of 1200˚C. Reaction sintering by design created two-phase microstructures from the mixture of Ti, Fe, Mo, and $TiB_2$ powders. XRD analysis confirmed that there was no residual $TiB_2$ after sintering, so the reaction proceeded to completion. It was proven that the desired microstructure of these cermets can be achieved by one fast sintering step. XRD also confirmed that beta-stabilization was achieved by the additions of Fe and Mo beta-stabilizing powders, with the exception of a minimal presence of alpha-Ti phase, which may be minimized further by a heat treatment.

Full density and stabilization of the beta-Ti phase was consistent among compositions of varying TiB volume percent. With these factors consistent, it was then

possible to evaluate mechanical properties of the different compositions with accuracy. Hardness, flexural strength, and fracture toughness were all recorded at levels at least comparable to and often exceeding the performance of other cermets.

The successful synthesis of samples was due to the CALPHAD design performed before mixing of powder compositions. Compositions were designed to allow for the full stabilization of the beta-Ti phase while avoiding the formation of intermetallic compounds. The sintering temperature of 1200˚C chosen using CALPHAD modeling proved to be a high enough temperature to aid consolidation and solidification kinetics in order to ensure densification.

Lastly, it was shown that mechanical properties of the bulk materials can be altered by the implementation of a simple heat treatment. Toughness was improved up to 9% by this method.

## 6.2 Future Work

During the course of this work, doors for future investigations into material properties were opened. One strong possibility for improvement of properties, in particular flexural strength, is the removal of inclusion particles. Strength above 1000 MPa could potentially be achieved in 50, 60, and 70 volume percent TiB cermets if Ca-O particles were removed.

The work presented in Section 5.3 highlights the formation of ternary (Ti,X)B boride compounds during sintering. There is yet to be work done on the effects of ternary (Ti,X)B borides in comparison to TiB borides on the mechanical properties of Ti-TiB cermets. This presents a future need for the project.

One occurrence that needs more investigation was the large decrease in flexural strength due to heat treatment. It was speculated that the creation of internal stresses and athermal omega precipitates in the beta-Ti phase due to fast quenching may have contributed to this phenomenon, but more work is needed for verification. The first step toward an answer would be microstructural investigation. Microscopy backed by XRD analysis would verify which phases are present and if any unwanted phases have formed to alter properties.

Another direction that is worth investigation is further CALPHAD analysis to design a fully stable beta-Ti phase as opposed to the metastable beta-Ti in this research. A metastable alloy was designed in order to avoid adding too much beta-stabilizer, which would form intermetallic compounds. However, it may be possible to push the beta-stabilizer content up to a point before forming intermetallics. This would reduce the formation of alpha-Ti and possibly eliminate the need for a heat treatment. This possibility was not researched extensively in this project.

Lastly, it will be important in the future to perform wear testing on these cermet samples. These Ti-TiB cermets have been proposed as replacements for other composite materials in applications such as cutting and forming tools. In order to find an industrial application for these Ti-TiB cermets, there must be wear testing data for comparison to other cermets, in addition to the mechanical properties contained in this report.

## REFERENCES


[1] G.Y. Chin, ASM Metals Handbook, ASM Met. Handb. 8 (1985) 229–232. doi:10.1016/S0026-0576(03)90166-8.

[2] P. Ettmayer, W. Lengauer, The Story of Cermets, Int. J. Powder Metall. 21 (1989) 37–38.

[3] K. Tsuda, History of development of cemented carbides and cermet, SEI Tech. Rev. (2016) 16–20.

[4] D. Moskowitz, M. Humenik, Cemented Titanium Carbide Cutting Tools, in: H.H. Hausner (Ed.), Modern Developments in Powder Metallurgy, 1st ed., New York, 1966: pp. 83–94.

[5] J. Du, A.P. Sanders, V. Jindal, K.S.R. Chandran, Rapid in situ formation and densification of titanium boride (TiB) nano-ceramic via transient liquid phase in electric field activated sintering, Scr. Mater. 123 (2016) 95–99. doi:10.1016/j.scriptamat.2016.06.010.

[6] H. Feng, Y. Zhou, D. Jia, Q. Meng, Microstructure and mechanical properties of in situ TiB reinforced titanium matrix composites based on Ti-FeMo-B prepared by spark plasma sintering, Compos. Sci. Technol. 64 (2004) 2495–2500. doi:10.1016/j.compscitech.2004.05.013.

[7] X. Zhang, Q. Xu, J. Han, V.L. Kvanin, Self-propagating high temperature combustion synthesis of TiB/Ti composites, Mater. Sci. Eng. A. 348 (2003) 41–46. doi:10.1016/S0921-5093(02)00635-4.

[8] M. De Graef, J.P.A. Löfvander, C. McCullough, C.G. Levi, The evolution of metastable B*f* borides in a Ti-Al-B alloy, Acta Metall. Mater. 40 (1992) 3395–3406. doi:10.1016/0956-7151(92)90053-H.

[9] K.B. Panda, K.S. Ravi Chandran, Synthesis of ductile titanium-titanium boride (Ti-TiB) composites with a beta-titanium matrix: The nature of TiB formation and composite properties, Metall. Mater. Trans. A. 34 (2003) 1371–1385. doi:10.1007/s11661-003-0249-z.

[10] S.E. Madtha, Nanostructured Bulk Titanium Boride, University of Utah, 2008.

[11] H. Saito, A. Iwabuchi, T. Shimizu, Effects of Co content and WC grain size on wear of WC cemented carbide, Wear. 261 (2006) 126–132. doi:10.1016/j.wear.2005.09.034.

[12] K. Narasimhan, S.P. Boppana, D.G. Bhat, Development of a graded TiCN coating for cemented carbide cutting tools-a design approach, Wear. 188 (1995) 123–129. doi:10.1016/0043-1648(95)06635-7.

[13] A.F. Lisovsky, Formation of mesostructure in WC-Co cemented carbides - a review, Sci. Sinter. 43 (2011) 161–173. doi:10.2298/SOS1102161L.

[14] M. Gao, Y. Pan, F.J. Oliveira, L. Yang, J.L. Baptista, J.M. Vieira, The formation of core-rim structures in Fe40Al/(TiC-TiN-WC) cermets produced by pressureless melt infiltration, Mater. Sci. Eng. A. 371 (2004) 277–282. doi:10.1016/j.msea.2003.12.001.

[15] G. Liu, S. Guo, J. Li, K. Chen, D. Fan, Fabrication of hard cermets by in-situ synthesis and infiltration of metal melts into WC powder compacts, J. Asian Ceram. Soc. 5 (2017) 418–421. doi:10.1016/j.jascer.2017.09.003.

[16] L.J. Prakash, Application of fine grained tungsten carbide based cemented carbides, Int. J. Refract. Met. Hard Mater. 13 (1995) 257–264. doi:10.1016/0263-4368(95)92672-7.

[17] S. Lay, C.H. Allibert, M. Christensen, G. Wahnström, Morphology of WC grains in WC-Co alloys, Mater. Sci. Eng. A. 486 (2008) 253–261. doi:10.1016/j.msea.2007.09.019.

[18] S. Okamoto, Y. Nakazono, K. Otsuka, Y. Shimoitani, J. Takada, Mechanical properties of WC/Co cemented carbide with larger WC grain size, Mater. Charact. 55 (2005) 281–287. doi:10.1016/j.matchar.2005.06.001.

[19] K. Jia, T.E. Fischer, B. Gallois, Microstructure, hardness and toughness of nanostructured and conventional WC-Co composites, Nanostructured Mater. 10 (1998) 875–891. doi:10.1016/S0965-9773(98)00123-8.

[20] Z.Z. Fang, Correlation of transverse rupture strength of WC-Co with hardness, Int. J. Refract. Met. Hard Mater. 23 (2005) 119–127. doi:10.1016/j.ijrmhm.2004.11.005.

[21] Y. Torres, R. Bermejo, F.J. Gotor, E. Chicardi, L. Llanes, Analysis on the mechanical strength of WC-Co cemented carbides under uniaxial and biaxial bending, Mater. Des. 55 (2014) 851–856. doi:10.1016/j.matdes.2013.10.051.

[22] L. Yanbin, L. Yong, T. Huiping, W. Bin, L. Bin, Fabrication and mechanical properties of in situ TiC/Ti metal matrix composites, J. Alloys Compd. 509 (2011) 3592–3601. doi:10.1016/j.jallcom.2010.12.086.

[23] S. Zhang, Titanium carbonitride-based cermets: Processes and properties, Mater. Sci. Eng. A. 163 (1993) 141–148. doi:10.1016/0921-5093(93)90588-6.

[24] Y. Li, N. Liu, X. Zhang, C. Rong, Effect of WC content on the microstructure and mechanical properties of (Ti, W)(C, N)-Co cermets, Int. J. Refract. Met. Hard Mater. 26 (2008) 33–40. doi:10.1016/j.ijrmhm.2007.01.003.

[25] H. Xiong, Z. you Li, X. Gan, L. Chai, Morphology evolution of TiC-based cermets via different sintering schedules, Ceram. Int. 43 (2017) 5805–5812. doi:10.1016/j.ceramint.2017.01.133.

[26] H. Zhou, C. Huang, B. Zou, H. Liu, H. Zhu, P. Yao, J. Wang, Effects of metal phases and carbides on the microstructure and mechanical properties of Ti(C,N)-based cermets cutting tool materials, Mater. Sci. Eng. A. 618 (2014) 462–470. doi:10.1016/j.msea.2014.09.052.

[27] X. Zhang, N. Liu, Microstructure, mechanical properties and thermal shock resistance of nano-TiN modified TiC-based cermets with different binders, Int. J. Refract. Met. Hard Mater. 26 (2008) 575–582. doi:10.1016/j.ijrmhm.2008.01.008.

[28] E.A. Gamble, B.G. Compton, V.S. Deshpande, A.G. Evans, F.W. Zok, Damage development in an armor ceramic under quasi-static indentation, J. Am. Ceram. Soc. 94 (2011). doi:10.1111/j.1551-2916.2011.04472.x.

[29] F. Thevenot, A review on boron carbide, Key Eng. Mater. 56–57 (1991) 59–88. doi:10.4028/www.scientific.net/KEM.56-57.59.

[30] B.G. Compton, F.W. Zok, Impact resistance of TiC-based cermets, Int. J. Impact Eng. 62 (2013) 75–87. doi:10.1016/j.ijimpeng.2013.06.008.

[31] M. Mashhadi, E. Taheri-Nassaj, V.M. Sglavo, H. Sarpoolaky, N. Ehsani, Effect of Al addition on pressureless sintering of B4C, Ceram. Int. 35 (2009) 831–837. doi:10.1016/j.ceramint.2008.03.003.

[32] D.M. Hulbert, D. Jiang, U. Anselmi-Tamburini, C. Unuvar, A.K. Mukherjee, Continuous functionally graded boron carbide-aluminum nanocomposites by spark plasma sintering, Mater. Sci. Eng. A. 493 (2008) 251–255. doi:10.1016/j.msea.2007.05.124.

[33] S. Hayun, N. Frage, M.P. Dariel, The morphology of ceramic phases in BxC-SiC-Si infiltrated composites, J. Solid State Chem. 179 (2006) 2875–2879. doi:10.1016/j.jssc.2006.01.031.

[34] J. Wang, X. Guo, J. Qin, D. Zhang, W. Lu, Microstructure and mechanical properties of investment casted titanium matrix composites with B4C additions, Mater. Sci. Eng. A. 628 (2015) 366–373. doi:10.1016/j.msea.2015.01.067.

[35] J. Keränen, T. Stenberg, T. Mäntylä, T. Lepistö, Microstructural characterization of detonation gun-sprayed boride-based cermet coatings, Surf. Coatings Technol. 82 (1996) 29–37. doi:10.1016/0257-8972(95)02539-1.

[36] K. ichi Takagi, High tough boride base cermets produced by reaction sintering, Mater. Chem. Phys. 67 (2001) 214–219. doi:10.1016/S0254-0584(00)00442-9.

[37] K. ichi Takagi, Development and application of high strength ternary boride base cermets, J. Solid State Chem. 179 (2006) 2809–2818. doi:10.1016/j.jssc.2006.01.023.

[38] J.M. Sánchez, I. Azcona, F. Castro, Mechanical properties of titanium diboride based cermets, J. Mater. Sci. 35 (2000) 9–14. doi:10.1023/A:1004763709854.

[39] R. Ahn, DG, Kawasaki, A, Watanabe, Microstructure and mechanical properties of TiB2-W cermets prepared by HIP., Mater. Trans. JIM. 37 (1996) 1078–1083.

[40] M. Eriksson, D. Salamon, M. Nygren, Z. Shen, Spark plasma sintering and deformation of Ti-TiB2 composites, Mater. Sci. Eng. A. 475 (2008) 101–104. doi:10.1016/j.msea.2007.01.161.

[41] F.C. Wang, Z. hui Zhang, J. Luo, C.C. Huang, S.K. Lee, A novel rapid route for in situ synthesizing TiB-TiB2 composites, Compos. Sci. Technol. 69 (2009) 2682–2687. doi:10.1016/j.compscitech.2009.08.010.

[42] K.S. Ravi Chandran, K.B. Panda, S.S. Sahay, TiBw-reinforced Ti composites: Processing, properties, application prospects, and research needs, Jom. 56 (2004) 42–48. doi:10.1007/s11837-004-0127-1.

[43] R.. Atri, K.. Ravichandran, S.. Jha, Elastic properties of in-situ processed Ti–TiB composites measured by impulse excitation of vibration, Mater. Sci. Eng. A. 271 (1999) 150–159. doi:10.1016/S0921-5093(99)00198-7.

[44] The Materials Information Society, ASM Handbook Volume 3 - Alloy Phase Diagrams, ASM Handb. (1992) 500. doi:10.1007/BF02869318.

[45] K.B. Panda, K.S. Ravi Chandran, Titanium-titanium boride (Ti-TiB) functionally graded materials through reaction sintering: Synthesis, microstructure, and properties, Metall. Mater. Trans. A. 34 (2003) 1993–2003. doi:10.1007/s11661-003-0164-3.

[46] M.E. Hyman, C. McCullough, C.G. Levi, R. Mehrabian, Evolution of boride morphologies in TiAl-B alloys, Metall. Trans. A. 22 (1991) 1647–1662. doi:10.1007/BF02667377.

[47] K.B. Panda, K.S.R. Chandran, First principles determination of elastic constants and chemical bonding of titanium boride (TiB) on the basis of density functional theory, Acta Mater. 54 (2006) 1641–1657. doi:10.1016/j.actamat.2005.12.003.

[48] S.S. Sahay, K.S. Ravichandran, R. Atri, Evolution of microstructure and phases in in situ processed Ti – TiB composites containing high volume fractions of TiB whiskers, J. Mater. Res. 14 (1999) 4214–4223.

[49] M. Selva Kumar, P. Chandrasekar, P. Chandramohan, M. Mohanraj, Characterisation of titanium-titanium boride composites processed by powder metallurgy techniques, Mater. Charact. 73 (2012) 43–51. doi:10.1016/j.matchar.2012.07.014.

[50] M. De Graef, J.P.A. Löfvander, C.G. Levi, Structure of complex monoborides in γ-TiAl alloys with Ta and B additions, Acta Metall. Mater. 39 (1991) 2381–2391. doi:10.1016/0956-7151(91)90019-W.

[51] S. Madtha, C. Lee, K.S. Ravi Chandran, Physical and mechanical properties of nanostructured titanium boride (TiB) ceramic, J. Am. Ceram. Soc. 91 (2008) 1319–1321. doi:10.1111/j.1551-2916.2007.02246.x.

[52] R.M. German, Particle Packing Characteristics, 18th ed., Metal Powder Industries Federation, Princeton, 1989.

[53] S. Madtha, K.S. Ravi Chandran, Reactive-sinter-processing and attractive mechanical properties of bulk and nanostructured titanium boride, J. Am. Ceram. Soc. 95 (2012) 117–125. doi:10.1111/j.1551-2916.2011.04852.x.

[54] B.A. Kazi, M.M. Abdul, parametric optimization of machining Ti-alloys in respect to surface roughness - a review, Appl. Mech. Mater. 152–154 (2012) 468–473. doi:10.4028/www.scientific.net/AMM.152-154.468.

[55] M.A.H. Gepreel, Texturing Tendency in β-Type Ti-Alloys, in: P. Wilson (Ed.), Recent Developments in the Study of Recrystallization, IntechOpen, 2013. doi:http://dx.doi.org/10.5772/53588.

[56] P.J. Bania, Beta titanium alloys and their role in the titanium industry, JOM. 46 (1994) 16–19. doi:10.1007/BF03220742.

[57] X. Shen, Z. Zhang, S. Wei, F. Wang, S. Lee, Microstructures and mechanical properties of the in situ TiB-Ti metal-matrix composites synthesized by spark plasma sintering process, J. Alloys Compd. 509 (2011) 7692–7696. doi:10.1016/j.jallcom.2011.05.017.

[58] K.S.R. Chandran, Alloy and Material Design, University of Utah Department of Metallurgical Engineering, Salt Lake City, 2014.

[59] S. Banerjee, U.M. Naik, Plastic instability in an omega forming Ti-15% Mo alloy, Acta Mater. 44 (1996) 3667–3677. doi:10.1016/1359-6454(96)00012-2.

[60] F. Sun, F. Prima, T. Gloriant, High-strength nanostructured Ti-12Mo alloy from ductile metastable beta state precursor, Mater. Sci. Eng. A. 527 (2010) 4262–4269. doi:10.1016/j.msea.2010.03.044.

[61] C.H. Wang, C.D. Yang, M. Liu, X. Li, P.F. Hu, A.M. Russell, G.H. Cao, Martensitic microstructures and mechanical properties of as-quenched metastable β-type Ti–Mo alloys, J. Mater. Sci. 51 (2016) 6886–6896. doi:10.1007/s10853-016-9976-6.

[62] C.H. Wang, M. Liu, P.F. Hu, J.C. Peng, J.A. Wang, Z.M. Ren, G.H. Cao, The effects of α″ and ω phases on the superelasticity and shape memory effect of binary Ti-Mo alloys, J. Alloys Compd. 720 (2017) 488–496. doi:10.1016/j.jallcom.2017.05.299.

[63] A. Janz, Thermodynamics and constitution of quaternary Mg-Al-Ca-Sr alloys and the extension to the quinary Mg-Al-Ca-Sr-Mn system, Clausthal University of Technology, 2008.

[64] P. Turchi, A. Landa, Thermodynamic Database, Lower Length Scale, PART II: Thermodynamic Assessment of Al–Mo–Si–U, Livermore, 2012. https://e-reports-ext.llnl.gov/pdf/696912.pdf.

[65] ASTM International, Standard test method for flexural strength of advanced ceramics at ambient, Annu. B. ASTM Stand. 94 (2008) 1–16. doi:10.1520/C1161-13.2.

[66] ASTM International, Standard test methods for determination of fracture toughness of advanced ceramics at ambient temperature, ASTM C1421-10. i (2011) 1–31. doi:10.1520/C1421-10.2.

[67] H.L. Chen, Y. Yang, Y. Tang, Q. Chen, A. Engström, Development of thermodynamic and kinetic databases for Ti/TiAl-based alloys, 2017 Diffus. Work. (2017).